

The Measurement of the Quasi-Elastic
Neutrino-Nucleon Scattering Cross Section
at the Tevatron

Narumon Suwonjandee



**The Measurement of the Quasi-Elastic
Neutrino-Nucleon Scattering Cross Section
at the Tevatron**

A Dissertation submitted to the
Division of Research and Advanced Studies
of the University of Cincinnati

in partial fulfillment of the
requirements for the degree of

DOCTORATE OF PHILOSOPHY

in the Department of Physics
of the College of Arts and Sciences

2004

by

Narumon Suwonjandee

B.Sc., Chulalongkorn University, 1993

M.Sc., Chulalongkorn University, 1996

M.S., University of Cincinnati, 1998

Committee Chair: Professor Randy Johnson

Abstract

The quasi-elastic neutrino nucleon cross section measurement has been measured in the low energy region less than 100 GeV. The data agree well with the model proposed by C. H. Llewellyn Smith. This model predicts that the quasi-elastic cross section should be constant in the high energy region. The NuTeV experiment at Fermilab provides data which allows us to measure the quasi-elastic cross section for both neutrinos and anti-neutrinos at high energy. We find that $\sigma_{qe}^{Nucleon}(\nu) = 0.94 \pm 0.03(stat.) \pm 0.07(syst.)$, and $\sigma_{qe}^{Nucleon}(\bar{\nu}) = 1.12 \pm 0.04(stat.) \pm 0.10(syst.)$ for neutrino and anti-neutrino, respectively.

Acknowledgments

First of all I would like to offer my sincere thanks to Prof. Randy Johnson for accepting me as an advisee and guiding me in research. His careful guidance, suggestions, patience, reading of the manuscript, and financial support are greatly acknowledged. I am also thankful to my committee members, Prof. Michael Sokoloff, Prof. L.C.R. Wijewardhana and Prof. Howard Jackson for accepting to serve in my committee and for all the suggestions.

Many thanks to all professors, physicists, graduate students and postdocs in NuTeV collaboration, especially, Prof. Donna Naple, GERALYN (Sam) Zeller, Unki Yang, Jeffrey McDonald and Martin Tzanov.

My stay in the Physics Department for the past few years had been memorable due to many good friends I met here. My special thanks to Sharmanthi Fernando, Ebru Celsuki, Zhiling Zhao, Sunil and Sriyani Jayatilleke, Nimal R. Wijesekera, Luminda Kulasiri, and many others for offering me their friendship.

I would also like to thank the Department of Physics of University of Cincinnati and the National Science Foundation for offering me scholarship and financial support when I travelled in the past few years. I thank all members of the staff and the faculty members, in particular Prof. Frank Pinski, Mr. David Will, Mrs. Melody Whitlock and Mrs. Donna Deutenberg, for providing a very friendly and a comfortable working environment and a helpful atmosphere to pursue my research.

I take this opportunity to show my gratitude to my mother, Siriporn and my sister, Jintanaporn who await for me back home in Thailand. They have encouraged and supported me over the years. I would like to thank Nadia Worthen who helps me through a lot of difficulties in living here. I also would like to thank Sommart Jarurattanakua, Taweekiat Iamngamtrap, Kobchai Tayanasant, Janjira Wongpaitoonpiya and all my friends for the encouragement they gave me over years.

Contents

1	Introduction	1
1.1	Standard Model	2
1.2	Neutrino Nucleon Scattering	5
1.3	Nuclear Interaction	5
1.4	$\nu - N$ Cross Section	6
2	The Theory of Neutrino-Nucleon Scattering	8
2.1	$\nu - N$ Scattering Formalism	9
2.2	$\nu - N$ Cross Section	11
2.2.1	The Quark Parton Model	16
2.2.2	QPM and Cross Sections	20
2.2.3	QPM and Structure Functions	22
2.3	$\nu - N$ QE Scattering Process	23
2.3.1	QE Cross Section	23
2.3.2	Electric and Magnetic Form Factors	27
2.3.3	Nuclear Effects	29
2.4	Resonances Process	31
2.4.1	RES Productions	31

2.4.2	RES Cross section for 1π using Albright Model	34
2.5	Higher Twist Model	36
2.5.1	Target Mass Effect	36
2.5.2	Higher Twist Effect	37
2.5.3	Cross Section using Modified PDF+HT	38
3	Experimental Apparatus	40
3.1	Neutrino at the Fermilab Tevatron	41
3.2	Neutrino Beamline	43
3.3	NuTeV Detector	44
3.3.1	Target Calorimeter	45
3.3.2	Toroidal Muon Spectrometer	49
3.4	Trigger and Gate	51
3.4.1	Trigger	51
3.4.2	Gate	51
3.5	The Calibration or Test Beam	53
4	Data Analysis	56
4.1	Hadron Energy Reconstruction	57
4.2	Muon Momentum Reconstruction	58
4.3	Muon Angle Reconstruction	59
4.4	Muon Energy Reconstruction	60
4.5	Analysis Cuts	61
4.5.1	Fiducial Volume and Timing Cuts	61
4.5.2	Geometric Cuts	63
4.5.3	The Cross Section Cuts	64

4.5.4	Flux Cuts	65
5	Monte Carlo Simulation	66
5.1	Event Generation	67
5.2	Cross Section Models	68
5.3	Physics Model Corrections	69
5.3.1	Charm Mass Correction	69
5.3.2	Isoscalar Correction	72
5.3.3	Propagator Correction	73
5.3.4	Radiative Correction	73
5.3.5	Nuclear Effect Correction	73
5.4	E_{had} Calculation	75
5.5	E_{μ} Calculation	78
5.6	Calculation of Other Variables	80
6	The Extraction of Flux and Quasi-Elastic Cross Sections	84
6.1	Flux	85
6.1.1	Fixed ν Flux Extraction Method	86
6.1.2	Flux Extraction	89
6.1.3	Flux Normalization	92
6.2	QE Events Extraction	96
6.2.1	Non DIS Events Extraction	96
6.3	Quasi-Elastic Cross Section Extraction	109
7	Systematic Errors	113
7.1	The Experimental Systematics	113
7.2	The Cross Section Extraction Systematics	114

7.2.1	Flux Extraction Methods	114
7.2.2	Q^2 Tail in $E_{had} < 5$ Region	115
7.3	The Model Systematics	115
7.3.1	M_A and F_A in C. H. Llewellyn Smith Quasi-elastic Model . . .	115
7.3.2	Limit on Higher Twist at High x	116
8	Conclusion	118
A	Place Study	123
B	E_μ Subtraction Calculation	134
	Bibliography	141

List of Figures

2.1	The Feynman diagram for charged current $\nu - N$ scattering	9
2.2	The Feynmann diagram of lepton-quark DIS	17
2.3	The helicity configurations in $\nu(\bar{\nu})$ scattering off $q(\bar{q})$	19
2.4	The Feynman diagram for CC DIS	21
2.5	Schematic diagrams of lepton-nucleon quasi-elastic scattering	24
2.6	Schematic diagrams of lepton-nucleon resonances process	32
2.7	Schematic diagram of lepton-nucleon neutrino-induced single pion	33
2.8	Schematic diagrams of lepton-nucleon in higher twist processes	38
3.1	The NuTeV Beamline.	42
3.2	The NuTeV SSQT.	43
3.3	The NuTeV detector.	45
3.4	The NuTeV calorimeter.	46
3.5	The scintillation counter.	48
3.6	The target drift chamber	50
3.7	Schematic of beam and gate structures	52
3.8	Schematic of accelerator time structure	53
3.9	Schematic diagram of NuTeV calibration beam spectrometer	54

5.1	Leading order diagrams for ν scattering off s or d quark	70
5.2	Examples of CC QED radiative correction diagrams	74
5.3	Comparison of DT to MC in E_{had} distribution	77
5.4	Comparison of DT to MC in E_μ distribution	79
5.5	Comparison of DT to MC in E_ν distribution	80
5.6	Comparison of DT to MC in θ_μ distribution	81
5.7	Comparison of DT to MC in q^2 distribution for $E_{had} < 5$	82
5.8	Comparison of DT to MC in q^2 distribution for $5 < E_{had} < 20$	83
6.1	The kinematic region for ν -N scattering processes.	86
6.2	The values of $\frac{B}{A}$ as a function of E_ν	92
6.3	The absolute flux distribution	95
6.4	The differential cross section in low E_{had} for $E_\nu = 60$ GeV	97
6.5	Comparison of DT to MC in E_{had} distribution for this analysis	98
6.6	NON-DIS sample as a function of E_ν	100
6.7	HT sample as a function of E_ν	101
6.8	Extracted QE sample as a function of E_ν	103
6.9	Extracted QE sample as a function of Q^2	105
6.10	Extracted QE sample as a function of E_ν with Q^2 and $E_\nu > 30$ GeV cuts	107
6.11	Acceptance correction	109
6.12	σ_{qe} per nucleon in an iron target as a function of E_ν	110
8.1	$\sigma_{qe}(\nu_\mu n \rightarrow \mu^- p)$ as a function of E_ν for a bound nucleon	120
8.2	$\sigma_{qe}(\bar{\nu}_\mu p \rightarrow \mu^+ n)$ as a function of E_ν for a bound nucleon	121
A.1	Comparison of CCFR to NuTeV length distribution in ν mode	124

A.2	Comparison of CCFR to NuTeV length distribution in $\bar{\nu}$ mode	124
A.3	NuTeV length distribution after removing the shift in ν mode	126
A.4	NuTeV length distribution after removing the shift in $\bar{\nu}$ mode	126
A.5	Comparison of E_{had} distribution with and without the shift	127
A.6	DT <i>LENGTH</i> versus E_{had} distributions in ν mode	129
A.7	MC <i>LENGTH</i> versus E_{had} distributions using big E_{had} bin in ν mode	129
A.8	DT <i>LENGTH</i> versus E_{had} distributions in $\bar{\nu}$ mode	130
A.9	MC <i>LENGTH</i> versus E_{had} distributions using big E_{had} bin in $\bar{\nu}$ mode	130
A.10	NuTeV <i>LENGTH</i> distribution with finer E_{had} bins in ν mode	131
A.11	NuTeV <i>LENGTH</i> distribution with finer E_{had} bins in $\bar{\nu}$ mode	132
A.12	MC <i>LENGTH</i> versus E_{had} distributions using finer E_{had} bins in ν mode	133
A.13	MC <i>LENGTH</i> versus E_{had} distributions using finer E_{had} bins in $\bar{\nu}$ mode	133
B.1	Comparison of DT to MC in E_{μ}^{diff} distribution in ν mode	137
B.2	Comparison of DT to MC in E_{μ}^{diff} distribution in $\bar{\nu}$ mode	137
B.3	Comparison of DT to MC in E_{μ}^{diff} distribution after applying the shift in ν mode	138
B.4	Comparison of DT to MC in E_{μ}^{diff} distribution after applying the shift in $\bar{\nu}$ mode	138
B.5	E_{had} distribution for DT when apply E_{μ}^{diff}	139
B.6	E_{had} distribution for DT when apply E_{μ}^{diff}	139
B.7	E_{had} distribution for MC when apply E_{μ}^{diff}	140
B.8	E_{had} distribution for MC when apply E_{μ}^{diff}	140

List of Tables

1.1	Three generations of leptons	3
1.2	Three generations of quarks	4
1.3	Fundamental fields and mediators	4
3.1	Fractional neutrino fluxes from various sources	44
3.2	Composition of one unit of NuTeV target calorimeter	47
3.3	NuTeV trigger list with descriptions	55
6.1	Comparison of \tilde{R} to extracted \tilde{R}'	93
6.2	The number of NON-DIS events	99
6.3	The number of HT events	102
6.4	The number of extracted QE events	104
6.5	The number of extracted QE events sum from $2.5 < Q^2 < 5 \text{ GeV}^2$	106
6.6	The final number of extracted QE events for $Q^2 < 2.5 \text{ GeV}^2$	108
6.7	The total QE cross section per nucleon bound in an iron target	111
6.8	NuTeV total QE cross section per bound nucleon	112
7.1	The systematic errors	117
8.1	NuTeV total QE cross section treated as a free nucleon	122

B.1	The mean values of E_{μ}^{diff}	135
B.2	The mean values of E_{μ}^{diff} after the shift	135

Chapter 1

Introduction

This thesis will present a measurement of the quasi-elastic scattering cross section from charged current neutrino-nucleon scattering at high energy ($E_\nu > 30$ GeV). Quasi-elastic events are characterized by low hadron energy (E_{had}), low momentum transfer (q^2), and low hadron invariant mass (W). The data used in this analysis are from the E815/NuTeV (Neutrino at the Tevatron, NuTeV) experiment at Fermilab. A sign selected quadrupole train, SSQT [1], was used in this experiment to produce the neutrino and anti-neutrino beams. This allows us to extract the neutrino and anti-neutrino cross sections separately.

The data taken from the NuTeV experiment are neutrino (or anti-neutrino) nucleon scattering events at very high energy, up to 350 GeV. Most events at high q^2 are deep inelastic scattering events where neutrino interacts incoherently with the individual quarks. For low q^2 events neutrinos see a nucleon as a single particle. Thus, they interact coherently with entire nucleon.

To extract the quasi-elastic events, we need to subtract off the more prevalent deep inelastic scattering events. We have to model the beam and detector with a Monte Carlo and then normalize the Monte Carlo events to the data in a region where deep inelastic scattering predominates. We extract the quasi-elastic events by subtracting the normalized Monte Carlo deep inelastic events from the data.

Finally we normalize our deep inelastic scattering cross section to the world average to determine absolute neutrino flux as a function of energy and use this flux to calculate the quasi-elastic cross section.

1.1 Standard Model

Neutrino-nucleon scattering interactions involve quarks inside the nucleon. Both neutrino and quark are fundamental particles. The Standard Model is a theory which successfully describes all known particle interactions (except gravity) and experiments. All matter is composed of fundamental particles with either spin-1 (“*bosons*”) or spin- $\frac{1}{2}$ (“*fermions*”). Fermions interact with the exchange of bosons.

Fermions can be classified in two categories: leptons and quarks. Leptons and quarks interact via the exchange of vector bosons. All charged fermions interact electromagnetically via the exchange of photons, γ . The Quantum Electrodynamics (QED) is a U(1) gauge theory which describes the electromagnetic interactions between charged particles. All fermions also interact weakly with the exchange of gauge bosons, W^\pm and Z^0 . The gauge theory which unified the QED to the weak interactions (elec-

troweak interaction) becomes $SU(2) \times U(1)$.

Only quarks carry the color charge of Quantum Chromodynamics (QCD) and interact strongly via the exchange gluons, g . QCD is an $SU(3)$ gauge theory which describes quarks as $SU(3)$ triplets and gluons as an $SU(3)$ octet. There are six kinds of quarks and six kinds of leptons which can be divided into three “*generations*” or “*families*”. They are listed in Table 1.1 and Table 1.2. The mass of quarks and leptons are taken from PDG (2002) [2].

	Lepton Type	Electric Charge (e)	Mass
First Generation	e^- Electron	-1	0.511 MeV
	ν_e Electron Neutrino	0	< 3 eV
Second Generation	μ^- Muon	-1	105.658 MeV
	ν_μ Muon Neutrino	0	< 0.19 MeV
Third Generation	τ^- Tau	-1	1.777 GeV
	ν_τ Tau Neutrino	0	< 18.2 MeV

Table 1.1: Three Generations of leptons

In lepton families, each lepton has its own anti-partner which has opposite charge and lepton number. There are totally 12 leptons. Similarly, each quark has its own anti-partner called “*anti-quark*” with opposite charge. Quarks come into one of three colors: red (r), blue (b), and green (g). Anti-quarks come in as anti-colors: \bar{r} , \bar{b} , \bar{g} . There are totally 18 quarks and 18 anti-quarks. Gluon carries two colors (*bicolored*), one unit of color and one of anti-color. There are eight gluons.

There are four fundamental interactions in the nature which describe all interactions

	Quark Type	Electric Charge (e)	Mass
First Generation	u Up	$\frac{2}{3}$	1.5-4.5 MeV
	d Down	$-\frac{1}{3}$	5-8.5 MeV
Second Generation	c Charm	$\frac{2}{3}$	1.0-1.4 GeV
	s Strange	$-\frac{1}{3}$	80-155 MeV
Third Generation	t Top	$\frac{2}{3}$	174.3 GeV
	b Bottom	$-\frac{1}{3}$	4.0-4.5 GeV

Table 1.2: Three Generations of Quarks

among particles: gravitational field, electromagnetic field, weak field, and strong field. They are distinguished by the effective coupling strengths and mediators. Four different types of interaction field are listed in Table 1.3.

Interaction Fields	Interaction Particles	Mediators Particles	Mediators Mass (GeV)	Effective Coupling Strength
Gravitational	All Particles	Graviton	Massless	$G_N \approx 10^{-37} GeV^{-2}$
Electromagnetic	All Electrically Charged Particles	Photon (γ)	Massless	$\alpha \approx 10^{-2}$
Weak	Quarks and Leptons	Vector Bosons (W^\pm, Z^0)	80, 91	$G_F \approx 10^{-5} GeV^{-2}$
Strong	All Colored Particles (Quarks, Gluons)	8 Gluons (g)	Massless	$G_S \approx 1 GeV^{-2}$

Table 1.3: Fundamental Fields and Mediators

The four mediators correspond to four different types of interactions. Except the graviton, the other three mediators are the gauge bosons which carry the force for related interaction. However, gravity acts on all particles through the exchange of graviton. Because the effective coupling strength of gravitational field is very small compare to the ones from the other types of interaction, gravity is negligible for the work covered in this analysis.

1.2 Neutrino Nucleon Scattering

Scattering experiments reveal that protons and neutrons inside nucleon are not point-like particles, but consist of bound states of quarks and gluons (sometimes called “*partons*”). Quarks have never been observed as free particles. They are always bound.

One way to probe for the structure of nucleons is to collide the nucleons with a beam of leptons. At high momentum transfer (q^2) or short wavelength, a lepton interacts directly with a quark. After scattering, the quark has enough energy to break up the nucleon. Such a process is considered as “*deep inelastic scattering process*” (DIS). For low q^2 or long wavelength the incoming lepton interacts coherently with all the quarks as if it sees a nucleon as one single particle. The recoiling nucleon exits as a single particle or as a simple excited state. The process which a neutrino scatters off a single nucleon and has a single nucleon and a scattered lepton in the final state is called “*quasi-elastic scattering process*” (QE). A process where quarks are excited from the ground state to excited state and produce Δ or N^* particles is called “*resonances*” (RES) production. The Δ or N^* particles are unstable particles which then decay into pions and nucleons.

1.3 Nuclear Interaction

The neutrino-nucleon ($\nu - N$) QE scattering process can also involve nuclear interaction. The QE scattering from nucleons bound in the nucleus differs from that for free nucleons in three respects [3]:

- The nucleons are not at rest in the lab frame;
- The nucleons are bound; and
- The Pauli exclusion principle restricts scattering into new states which are already occupied (this causes a suppression of QE scattering at small q^2).

An incoming neutrino scatters from a single nucleon in the free Fermi sea, with the recoiling nucleon required to lie outside the Fermi sphere. Because of the Pauli exclusion principle, the recoiled nucleon cannot scatter into an already occupied state. The size of the Fermi sphere depends on the Fermi momentum K_F . The nuclear Fermi momentum is related to the nuclear density ρ by $K_F = (3\pi^2\rho/2)^{1/3}$ [4]. ρ is also roughly constant for the heavy nuclei. The momentum distribution for protons and neutrons are taken as follows:

$$\begin{aligned} K_F^p &= \left(\frac{2Z}{A}\right)^{\frac{1}{3}} K_F, \\ K_F^n &= \left(\frac{2N}{A}\right)^{\frac{1}{3}} K_F, \end{aligned} \tag{1.1}$$

where Z is the number of protons, N is the number of neutrons and $A = Z + N$ is the atomic number. For an isoscalar target $Z = N = A/2$ and $K_F^p = K_F^n = K_F$. The Fermi momentum for iron ^{56}Fe is 0.257 GeV/c [5].

1.4 $\nu - N$ Cross Section

At high energy, the following ν -N scattering process can be considered as either DIS, QE or RES depends on the momentum transfer q^2 and the effective mass of the final

state:

$$\nu_\mu + N \rightarrow \mu + X.$$

Once we know the number of each type of events, we calculate the cross section (σ) from

$$\sigma \propto \frac{N}{\Phi}.$$

where N is the number of events and Φ is the neutrino flux.

We will discuss the theory of neutrino-nucleon scattering process in more detail in the next chapter. The experiment setup will be discussed in chapter 3. Chapter 4 and 5 will describe how to reconstruct neutrino events from the data and simulate events in the Monte Carlo. The extraction methods used in this analysis will be present in chapter 6. Chapter 7 will present the systematic errors. Chapter 8 will summarize our conclusion.

Chapter 2

The Theory of Neutrino-Nucleon Scattering

In the previous chapter we classify the continuum of neutrino-nucleon ($\nu - N$) interactions as deep inelastic scattering (DIS) where high energy neutrino scatters off of individual quarks inside a nucleon incoherently, quasi-elastic (QE) scattering and resonances (RES) production where the neutrino coherently interact with a single nucleon.

In this chapter we will develop the formalism for DIS and QE scattering, and describe our “*higher twist*” (HT) model which attempts to connect coherent and incoherent processes.

2.1 $\nu - N$ Scattering Formalism

Figure 2.1 shows the relevant Feynman diagram for lepton-nucleon scattering. The incoming lepton (ν or l) which carries a four-momentum k scatters off a nucleon of mass M and four-momentum P with the exchange of a photon (γ) for electromagnetic interactions or a vector boson (W^\pm) for charged-current (CC) weak interactions. In the CC interactions the neutrino changes to its lepton partner with a four-momentum k' . The W^\pm boson carries a momentum transfer q , where $q = k - k'$.

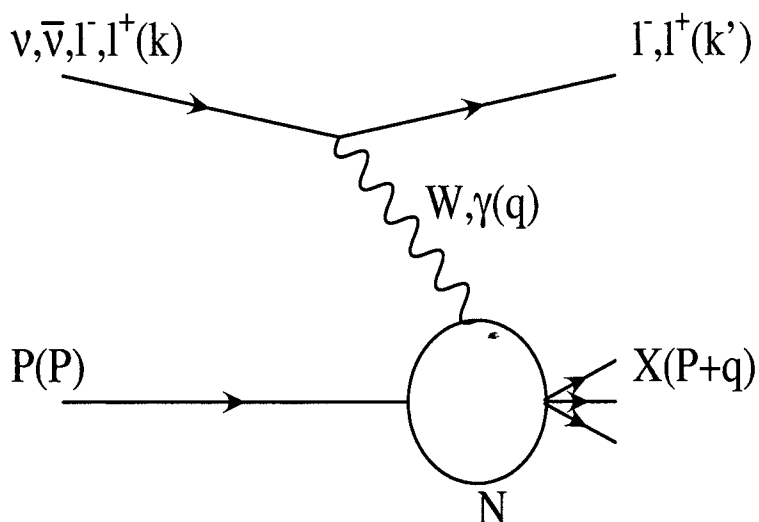


Figure 2.1: The Feynman diagram for charged current lepton-nucleon scattering. This process can occur as an electromagnetic (via the exchange of a photon) or weak (via the exchange of W-boson) interaction process.

The components of the four-momentum, k , k' , P , and p' in the lab system are:

$$k = (E_\nu, 0, 0, E_\nu)$$

$$\begin{aligned}
k' &= (E_\mu, p_\mu \sin \theta_\mu \cos \phi_\mu, p_\mu \sin \theta_\mu \sin \phi_\mu, p_\mu \cos \theta_\mu) \\
P &= (M, 0, 0, 0) \\
p' &= P + q = P + (k - k')
\end{aligned} \tag{2.1}$$

We normally use the Lorentz-invariant variables to describe the scattering process. They are the square of the center of mass energy (s):

$$s = (P + k)^2 = M^2 + 2ME_\nu, \tag{2.2}$$

the energy transferred to the hadron (ν):

$$\nu = \frac{P \cdot q}{M} = E_\nu - E_\mu = E_{had} - M, \tag{2.3}$$

the negative square of the four-momentum transfer (Q^2):

$$Q^2 = -q^2 = -(k - k')^2 = -m_\mu^2 + 2E_\nu(E_\mu - p_\mu \cos \theta_\mu), \tag{2.4}$$

the invariant mass squared of the hadrons (W^2):

$$W^2 = p'^2 = (P + q)^2 = M^2 + 2M\nu - Q^2 \geq M^2, \tag{2.5}$$

the Bjorken scaling variable (x):

$$x = \frac{-q^2}{2P \cdot q} = \frac{Q^2}{2M\nu}, \tag{2.6}$$

and the inelasticity (y):

$$y = \frac{P \cdot q}{P \cdot k} = \frac{E_{had}}{E_\nu}. \quad (2.7)$$

For elastic scattering of a massless particle in the center of mass frame, y is related to the scattering angle (θ^*) by:

$$y = \frac{1 - \cos \theta^*}{2}. \quad (2.8)$$

In $\nu - N$ scattering experiments, the three independently measured variables in a CC events are the outgoing muon momentum (p_μ), the outgoing muon angle (θ_μ), and the observed energy of the final state hadrons (E_{had}). From these three quantities the neutrino energy can be calculated by $E_\nu = E_{had} + E_\mu - M$.

2.2 $\nu - N$ Cross Section

Let us consider a CC interaction for a muon neutrino scattering off a nucleon. The matrix element \mathcal{M} of the Feynmann diagram in Figure 2.1 can be written as the product of the leptonic and the hadronic vertices and the W boson propagator:

$$\mathcal{M} = J_\alpha^{hadron} \left(\frac{g_{\alpha\beta} + q_\alpha q_\beta / M_W^2}{q^2 - M_W^2} \right) J_{lepton}^\beta. \quad (2.9)$$

The lepton-boson vertex consists of an annihilation of a muon neutrino (ν_μ) with a four-momentum k and spin s and a creation of a muon with a four-momentum k' and spin s' . The leptonic part of the interaction takes the form:

$$J_{lepton}^\beta = \frac{-ig_w}{2\sqrt{2}} \langle \bar{u}_\mu(k', s') | \gamma^\beta (1 - \gamma_5) | u_\nu(k, s) \rangle, \quad (2.10)$$

where g_w is the weak coupling constant, $\bar{u}_\mu(k', s')$ is the wave function of the outgoing muon, and $u_\nu(k, s)$ is the wave function of the incoming neutrino. Squaring the leptonic part, summing over outgoing spins, and averaging over incoming spins gives the covariant leptonic tensor $L_{\alpha\beta}$:

$$\begin{aligned}
L_{\alpha\beta} &= \sum_{s,s'} \left(\frac{-ig_w}{2\sqrt{2}} \langle \bar{u}_\mu(k', s') | \gamma_\alpha (1 - \gamma_5) | u_\nu(k, s) \rangle \right) \\
&\quad \times \left(\frac{-ig_w}{2\sqrt{2}} \langle \bar{u}_\mu(k', s') | \gamma_\beta (1 - \gamma_5) | u_\nu(k, s) \rangle \right)^\dagger \\
&= \frac{g_w^2}{8} \sum_{s,s'} \langle \bar{u}_\mu(k', s') | \gamma_\alpha (1 - \gamma_5) | u_\nu(k, s) \rangle \langle \bar{u}_\nu(k, s) | \gamma_\beta (1 - \gamma_5) | u_\mu(k', s') \rangle \\
&= g_w^2 [k'_\alpha k_\beta + k'_\beta k_\alpha - k \cdot k' g_{\alpha\beta} \mp ik^\gamma k'^\delta \epsilon_{\gamma\delta\alpha\beta}], \tag{2.11}
\end{aligned}$$

where the $-(+)$ term applies to incident neutrinos (anti-neutrinos). $g_{\alpha\beta}$ is a symmetric metric tensor and $\epsilon_{\gamma\delta\alpha\beta}$ is the totally anti-symmetric metric tensor.

Hadrons are not point-like particles, and can not be described with the simple current given in Eq. 2.10. We write the hadronic tensor rather than hadronic current. Like the lepton tensor, the hadronic tensor is defined as a product of hadronic current, $W^{\alpha\beta} = (J^{hadron})^\alpha J_{hadron}^{\beta\dagger}$. The most general expression for hadronic tensor $W^{\alpha\beta}$ is a second-rank tensor which parametrizes the nucleon-boson vertex. It should depend on P , p' , and q . Since $q = P - p'$, these three are not independent. We can use any two of them; the customary choice is P and q . Thus the most general hadronic tensor written in terms of available vectors for lepton-nucleon scattering process is:

$$\begin{aligned}
W^{\alpha\beta} &= \frac{g_w^2}{8} \left[-g^{\alpha\beta} V_1 + P^\alpha P^\beta V_2 + (P^\alpha q^\beta + P^\beta q^\alpha) V_3 \right. \\
&\quad \left. + q^\alpha q^\beta V_4 - i\epsilon^{\alpha\beta\gamma\delta} P_\gamma q_\delta V_5, + i(P^\alpha q^\beta - P^\beta q^\alpha) V_6 \right], \tag{2.12}
\end{aligned}$$

where V_i are the structure functions which depend only on the Lorentz invariant quantities made up of P and q .

W is a spin-1 massive particle and its propagator is:

$$\frac{g_{\alpha\beta} + q_\alpha q_\beta / M_W^2}{q^2 - M_W^2} \approx -\frac{g_{\alpha\beta}}{M_W^2}. \quad (2.13)$$

The W boson mass, M_W , is very large, and therefore the terms $q_\alpha q_\beta / M_W^2 \ll 1$ and $q^2 \ll M_W^2$ can be ignored. (But in our flux analysis (Chapter 6.1.2) where q^2 can be large, we will make a correction to compensate for dropping this term.)

Contracting of the leptonic and hadronic tensors yields:

$$\begin{aligned} |\mathcal{M}|^2 &= \frac{L_{\alpha\beta} W^{\alpha\beta}}{M_W^4} = \frac{g_w^4}{8M_W^4} \left\{ 2(k \cdot k') V_1 + [2(k \cdot P)(k' \cdot P) - (k \cdot k') M_N^2] V_2 \right. \\ &\quad + 2[(k \cdot P)(k' \cdot q) + (k \cdot \hat{q})(k' \cdot P) - (k \cdot k')(P \cdot q)] V_3 \\ &\quad + [2(k \cdot q)(k' \cdot q) - (k \cdot k') q^2] V_4 \\ &\quad - 2[(k' \cdot P)(k \cdot q) - (k' \cdot q)(k \cdot P)] V_5 \\ &\quad \left. + [(P^\alpha q^\beta - P^\beta q^\alpha) k^\gamma k'^\delta \epsilon_{\gamma\delta\alpha\beta}] V_6 \right\} \\ &= \frac{g_w^4}{8M_W^4} \left\{ 2MxyE_\nu V_1 + E_\nu M^2 [2(1-y)E_\nu - Mxy] V_2 \right. \\ &\quad - ME_\mu m_\mu^2 V_3 + 2MxyE_\nu m_\mu^2 V_4 \\ &\quad \left. + 2M^2 E_\nu^2 xy(2-y) V_5 \right\}. \quad (2.14) \end{aligned}$$

As can be seen in the above equation V_6 gives no contribution to the cross section. At high energies the contribution from V_3 and V_4 are negligible since they are proportional to the muon mass.

The differential cross section in the lab system is defined as follows:

$$\begin{aligned}
\frac{d^2\sigma^{\nu N}}{d\Omega_\mu dE_\mu} &= \frac{1}{(4\pi)^2} \frac{E_\mu}{E_\nu} |\mathcal{M}|^2 \\
&= \frac{g_w^4}{8} \frac{E_\mu}{(4\pi)^2} \left(\frac{1}{M_W^4} \right) \\
&\quad \times \left[2MxyV_1 + M^2(2E_\nu(1-y) - Mxy)V_2 + 2M^2xyE_\nu(2-y)V_5 \right].
\end{aligned} \tag{2.15}$$

We can change the differential cross section variable from Ω_μ and E_μ to invariant variables x and y and rewrite the weak coupling constant in terms of the Fermi coupling constant (G_F) using the following relations:

$$dxdy = \frac{E_\mu}{2\pi M\nu} d\Omega dE_\mu, \tag{2.16}$$

and

$$G_F = \frac{\sqrt{2}}{8} \left(\frac{g_w}{M_W} \right)^2. \tag{2.17}$$

For convenience we use E instead of E_ν . The cross section then becomes:

$$\frac{d^2\sigma^{\nu(\bar{\nu})}}{dxdy} = \frac{G_F^2 ME}{\pi} \left[Mxy^2V_1 + \left(1 - y - \frac{Mxy}{2E} \right) M^2\nu V_2 \pm 2M^2x\nu y \left(1 - \frac{y}{2} \right) V_5 \right]. \tag{2.18}$$

The $-(+)$ term applies to incident neutrinos (anti-neutrinos) scattering off from a nucleon.

The structure functions V_i are often expressed in terms of new dimensionless structure

functions F_i as follows:

$$\begin{aligned}
MV_1(\nu, Q^2) &= F_1(x, Q^2), \\
M^2\nu V_2(\nu, Q^2) &= F_2(x, Q^2), \\
2M^2\nu V_5(\nu, Q^2) &= F_3(x, Q^2).
\end{aligned} \tag{2.19}$$

These structure functions $F_i(x, Q^2)$ not only depend on the quark flavor of the target particle, but also on whether the probing particle is a neutrino or anti-neutrino.

The cross section now takes the form:

$$\frac{d^2\sigma^{\nu(\bar{\nu})}}{dxdy} = \frac{G_F^2 ME}{\pi} \left[\left(1 - y - \frac{Mxy}{2E}\right) F_2^{\nu(\bar{\nu})} + \frac{y^2}{2} 2xF_1^{\nu(\bar{\nu})} \pm y\left(1 - \frac{y}{2}\right)x F_3^{\nu(\bar{\nu})} \right]. \tag{2.20}$$

Electron-nucleon (eN) scattering process, which is an electromagnetic interaction with a photon exchange, is another way to measure the structure functions of a proton (refer back to Fig. 2.1). In this case there are only two measurable structure functions involved which are xF_1^{eN} and F_2^{eN} [6, 7]¹. However, the ratio of the structure functions are related by $\frac{F_2^{eN}}{2xF_1^{eN}} = \frac{F_2^{\nu N}}{2xF_1^{\nu N}}$, where $F_2^{\nu N}$ and $2xF_1^{\nu N}$ are structure functions of $\nu - N$ scattering process. A new function R is defined as the ratio of these two structure functions from electron scattering data. R is related to the longitudinal (σ_L) and tranverse (σ_T) absorption cross sections and can be measured [8, 9, 10]. R

¹ $xF_1^{eN}(x)$ and $F_2^{eN}(x)$ terms are proportional to the sum of the product of the quark distribution and the square of the charges of the quarks inside the nucleon ($F_1(x)$ or $F_2(x) \propto \sum_i Q_i^2 p_i(x)$). Q_i is the charge of the quark. $p_i(x)$ is the quark distribution that will be discussed in the quark parton model section. $F_2^{eN}(x)$ relates to $F_2^{\nu N}(x)$ by $F_2^{\nu N}(x) = 18/5 F_2^{eN}(x)$.

is defined as:

$$R(x, Q^2) = \frac{\sigma_L}{\sigma_T} = \frac{F_2}{2xF_1} \left(1 + \frac{4M^2x^2}{Q^2} \right) - 1, \quad (2.21)$$

where σ_L and σ_T relate to F_1^{eN} and F_2^{eN} by [11]:

$$\begin{aligned} \sigma_L &= \frac{4\pi^2\alpha}{K} \left[\left(1 + \frac{\nu^2}{Q^2} \right) \frac{F_2^{eN}}{\nu} - \frac{F_1^{eN}}{M} \right], \\ \sigma_T &= \frac{4\pi^2\alpha}{MK} F_1^{eN}. \end{aligned} \quad (2.22)$$

α is the fine structure constant. K is the energy carried by a real photon and defined as:

$$K = \nu - \frac{Q^2}{M}.$$

Using this R function, Eq. 2.20 can be expressed in terms of just two unknown structure functions F_2 and xF_3 :

$$\frac{d^2\sigma^{\nu(\bar{\nu})}}{dx dy} = \frac{G_F^2 M E}{\pi} \left[\left(1 - y - \frac{Mxy}{2E} + \frac{y^2}{2} \frac{1 + \frac{4M^2x^2}{Q^2}}{1 + R(x, Q^2)} \right) F_2^{\nu(\bar{\nu})} \pm y \left(1 - \frac{y}{2} \right) x F_3^{\nu(\bar{\nu})} \right]. \quad (2.23)$$

2.2.1 The Quark Parton Model

The quark parton model (QPM) supposes that a nucleon is composed of point-like non-interacting scattering centers known as partons (quarks and gluons). Quarks inside the nucleon are composed of “*valence*” quarks, which give it its flavor properties, and a “*sea*” of quark-antiquark pairs which have overall no flavor. Both valence-quark (q_v) and sea-quark (q_s) and sea-antiquark (\bar{q}_s) are considered as partons. The antiquark distributions ($\bar{q}(x)$) inside the nucleon are purely from the sea distributions, whereas the quark distributions ($q(x)$) are from valence and sea distributions. x is

momentum fraction carried by quark or anti-quark. In this analysis the $q_s(x)$ and $\bar{q}_s(x)$ are assumed to be the same ².

$$q(x) = q_v(x) + q_s(x), \quad (2.24)$$

$$\bar{q}(x) = \bar{q}_s(x), \quad (2.25)$$

and

$$q_s(x) = \bar{q}_s(x). \quad (2.26)$$

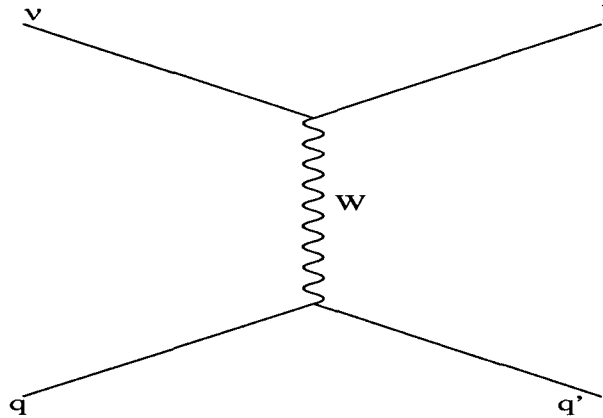


Figure 2.2: The Feynmann diagram of lepton-quark deep inelastic scattering via the exchange of intermediate vector bosons (W^\pm) in the CC interaction.

In the QPM, the neutrino interacts with the individual partons and not the nucleon as a whole. The Feynmann diagram of a neutrino scattered off a quark is shown in Fig. 2.2. For neutrinos which are spin-1/2 particles, the spin is always opposite to the linear momentum and this is referred to as “*left-handed*”, whereas the antineu-

²NuTeV measurements have revealed significant discrepancies of $\sin^2_{\theta_w}$ measurement between the observed nucleon-neutrino interaction and that predicted by the Standard Model [12, 13]. One explanation could be the asymmetry of strange sea in nucleons [14, 15].

trinos are always “*right-handed*”. The momentum of the particle is used to define as a preferred direction in space. The property which has been called left-handed and right-handed is called “*helicity*”. The helicity of a particle is +1 if the spin of a particle points in the same direction as the linear momentum, and is -1 if the spin points in the opposite direction.

The interacting parton constituents of the nucleon can be either quark (q) or anti-quark (\bar{q}) which carries spin-1/2. The total spin for neutrino-parton scattering process can be either 0 or 1. The possible helicity configurations of neutrino-parton scattering are shown in Fig. 2.3. In addition, the nucleon, in general, may have some scalar partons (k) which have no spin. These may be either particles themselves or ignored terms like a mass term of the parton in the interaction. In this case there would be spin 1/2 scattering process also.

The cross section for neutrino elastic scattering from point-like particles depends only on the square of center-of-mass energy ($s = 2mE$) and the scattering angle (θ^*). m is the mass of a parton. The differential cross sections for the neutrino-parton scattering are given by:

$$\text{total spin } 0 : \quad \frac{d\sigma^{\nu q}}{d \cos \theta^*} = \frac{d\sigma^{\nu \bar{q}}}{d \cos \theta^*} = \frac{G_F^2 s}{\pi} = \frac{2G_F^2 mE}{\pi}, \quad (2.27)$$

$$\text{total spin } 1 : \quad \frac{d\sigma^{\nu \bar{q}}}{d \cos \theta^*} = \frac{d\sigma^{\nu q}}{d \cos \theta^*} = \frac{G_F^2 s}{\pi} \left(\frac{1 + \cos \theta^*}{2} \right)^2 = \frac{2G_F^2 mE}{\pi} (1 - y)^2, \quad (2.28)$$

$$\text{total spin } \frac{1}{2} : \quad \frac{d\sigma^{\nu k}}{d \cos \theta^*} = \frac{d\sigma^{\nu k}}{d \cos \theta^*} = \frac{G_F^2 s}{\pi} (1 + \cos \theta^*) = \frac{4G_F^2 mE}{\pi} (1 - y) \quad (2.29)$$

In the zero angular momentum case, the cross section depends only on the center-of-mass energy not the scattering angle θ^* (Eq. 2.27). For neutrino scatters off a

right-handed antiquark or anti-neutrino scatters off a left-handed quark, the total angular momentum of the system is 1 and the cross section depends on the scattering angle θ^* (Eq. 2.28). If there are spin-0 k partons (no helicity particles), the total angular momentum of the $\nu - k$ or $\bar{\nu} - k$ will be $1/2$ and the cross section will also be angular dependence (Eq. 2.29).

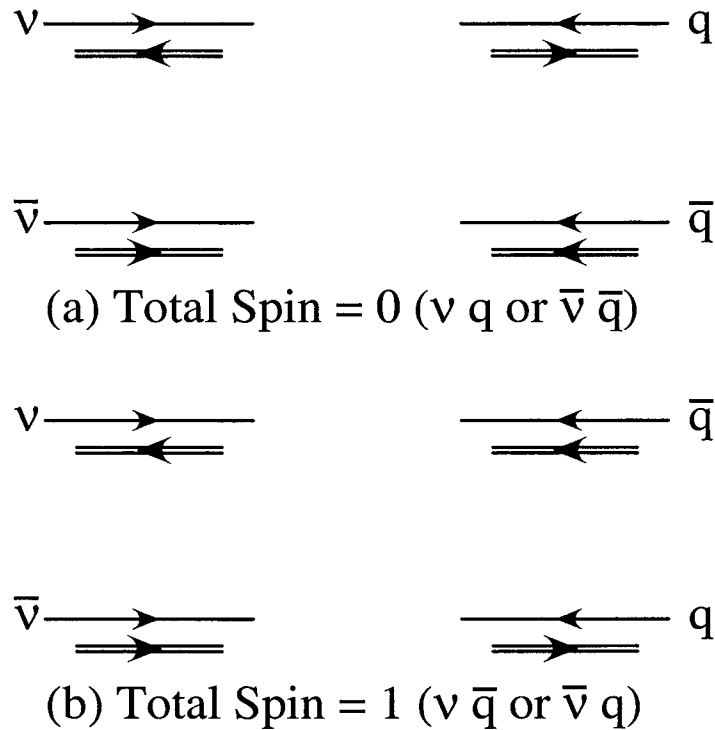


Figure 2.3: The helicity configurations for high energy neutrinos and anti-neutrinos scattering off quarks and anti-quarks. The single line represents the linear momentum. The double line is spin.

2.2.2 QPM and Cross Sections

QPM states that partons are bounded inside a nucleon. Assume that the initial momentum of the i_{th} parton, P_i , is a fraction ξ_i of the momentum of the nucleon P :

$$P_i = \xi_i P \quad (2.30)$$

The final momentum of the struck parton is

$$P_i' = P_i + q \quad (2.31)$$

By neglecting the mass of the parton, $P_i'^2$ and $P_i'^2 \approx 0$, one gets:

$$0 \approx P_i'^2 = (P_i + q)^2 = (\xi_i P + q)^2 \approx q^2 + 2\xi P \cdot q \quad (2.32)$$

and hence:

$$\xi_i = \frac{-q^2}{2P \cdot q} = x. \quad (2.33)$$

This infers that the Bjorken x is simply the fractional momentum of the nucleon carried by the parton. Figure 2.4 shows neutrino scatters off an individual quark. Quarks involved in this process can be valence or sea quarks, while the anti-quarks are only from sea quarks.

Now let us consider a neutrino or anti-neutrino DIS scatters from a parton, q or \bar{q} or k . Because the momentum is not known, we introduce the parton distribution function, $p(x)$, the probability of scattering from a particular type of partons. The quantity $p(x)dx$ is interpreted as the probability of finding a parton of type p in a hadron

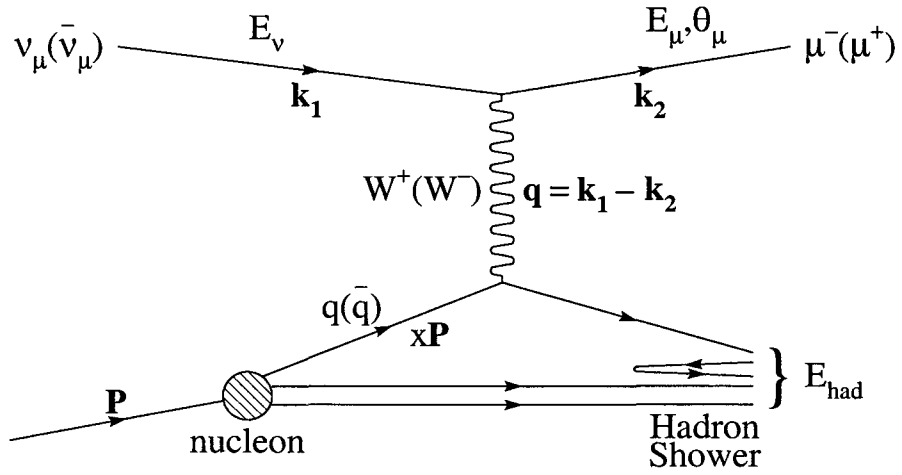


Figure 2.4: The Feynman diagram for charged current DIS. The struck quark carries a fraction x of the nucleon's four-momentum P . The quarks in this interaction are from valence and sea quarks while the anti-quarks are only from sea quarks. The two lines coming out from the nucleon are either q or \bar{q} .

carrying momentum fraction x to $x + dx$. The off-shell mass m of parton relates to the mass of nucleon by $m = xM$. Then using the parton momentum distribution $x p(x)$, the differential cross section for scattering off one parton is

$$\frac{d^2\sigma^\nu}{dx dy} \propto \frac{2G_F^2 M E}{\pi} x p(x). \quad (2.34)$$

Then the total differential cross section due to all types of partons becomes:

$$\begin{aligned} \frac{d^2\sigma^\nu}{dx dy} &= \frac{2G_F^2 M E}{\pi} [x q^\nu(x) + (1-y)^2 x \bar{q}^\nu(x) + 2(1-y)x k^\nu(x)], \\ \frac{d^2\sigma^{\bar{\nu}}}{dx dy} &= \frac{2G_F^2 M E}{\pi} [x \bar{q}^{\bar{\nu}}(x) + (1-y)^2 x q^{\bar{\nu}}(x) + 2(1-y)x k^{\bar{\nu}}(x)]. \end{aligned} \quad (2.35)$$

2.2.3 QPM and Structure Functions

The parton distributions are associated with the structure functions by comparing the y dependent terms of Eq. 2.35 with Eq. 2.20, yielding:

$$\begin{aligned}
 2xF_1^{\nu,\bar{\nu}} &= 2[xq^{\nu,\bar{\nu}}(x) + x\bar{q}^{\nu,\bar{\nu}}(x)], \\
 F_2^{\nu,\bar{\nu}} &= 2[xq^{\nu,\bar{\nu}}(x) + x\bar{q}^{\nu,\bar{\nu}}(x) + 2xk^{\nu,\bar{\nu}}(x)], \\
 xF_3^{\nu,\bar{\nu}} &= 2[xq^{\nu,\bar{\nu}}(x) - x\bar{q}^{\nu,\bar{\nu}}(x)],
 \end{aligned}
 \tag{2.36}$$

where the $\frac{Mxy}{E_\nu}$ term has been neglected.

In QPM the structure functions are purely functions of the Bjorken variable x only. This assumption is known as the Bjorken scaling hypothesis. This implies that in the regime where the QPM is valid, the structure functions are no longer Q^2 dependence. Thus

$$F_i(x, Q^2) \rightarrow F_i(x). \tag{2.37}$$

In general the difference between the two structure functions, $2xF_1$ and xF_3 , is in the antiquark components which are all sea quark components. The xF_3 term will depend only on valence quarks.

If the scalar distribution function is negligible, then

$$2xF_1 = F_2. \tag{2.38}$$

which is known as the Callan-Gross relation.

2.3 $\nu - N$ QE Scattering Process

The DIS scattering process occurs in all energy transfer regions and had been discussed in the previous section. This section we will move to the low energy transfer region where QE scattering process dominates. The QE scattering is a process that occurs when the incoming particle does not have enough energy to break the nucleon. It rather changes the quarks' flavor inside the nucleon via the exchange of intermediate vector bosons, W^\pm . Figure 2.5 shows the Feynmann diagrams for the quasi-elastic scattering processes.

$$\nu(k) + n(p) \rightarrow l^-(k') + p(p'). \quad (2.39)$$

$$\bar{\nu}(k) + p(p) \rightarrow l^+(k') + n(p'). \quad (2.40)$$

According to the conservation of charge, neutrino can scatter quasi-elastically only with neutron while anti-neutrino interacts only with proton. These are charged current interactions.

2.3.1 QE Cross Section

The matrix element of QE interaction for neutrino can be written as a product of the hadronic weak current and the leptonic current in the same way as for DIS process:

$$M = \frac{G_F}{\sqrt{2}} \cos \theta_c \langle p(p') | J_\alpha^0 | n(p) \rangle \left(\frac{g_{\alpha\beta}}{q^2 - M_W^2} \right) J_{lepton}^\beta, \quad (2.41)$$

where G_F is the Fermi constant and θ_c is the Cabbibo angle ($\cos \theta_c = 0.98$). The leptonic part is the same as the one in DIS process. J_α^0 is the $\Delta S = 0$ hadronic current and is different from the one in DIS process. For QE, the hadronic current involves the quark flavor changing which is related to the Cabbibo, Kobayashi, and

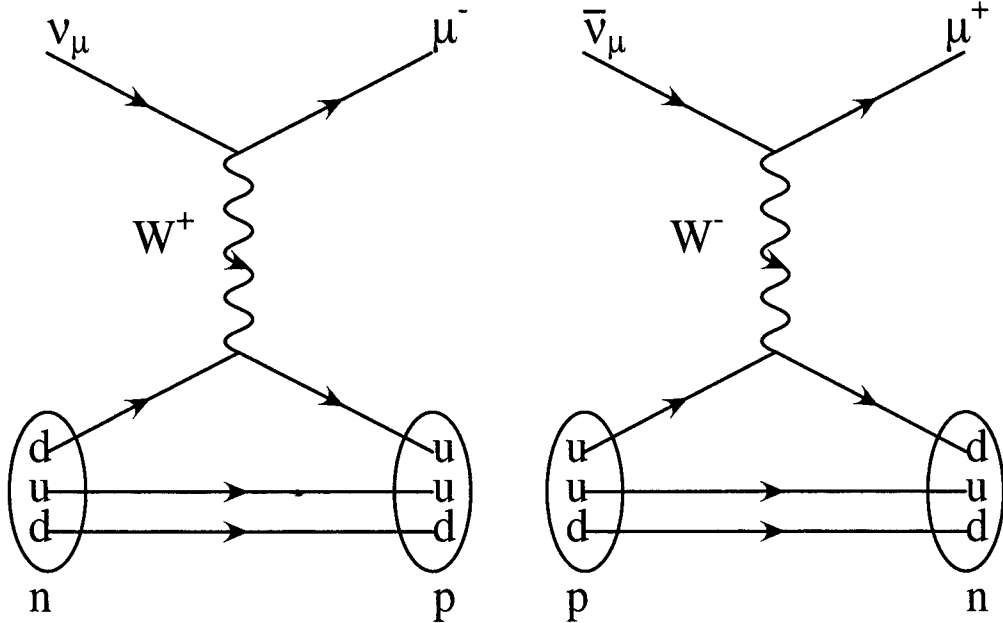


Figure 2.5: Schematic diagram of lepton-nucleon quasi-elastic scattering via the exchange of intermediate vector bosons (W^\pm).

Maskawa (CKM) matrix, U_{ij} . Instead of writing the hadronic tensor to compare with the one in DIS process, we start with the hadronic current which can be related to the photon scattering process. The hadronic current can be written in terms of six complex form factors which characterize the structure of nucleon [16] as:

$$J_\alpha^0 = \gamma_\alpha F_V^1 + \frac{i\sigma_{\alpha\nu}q^\nu}{2M}\xi F_V^2 + \frac{q_\alpha}{M}F_S + \gamma_\alpha\gamma_5 F_A + \frac{q_\alpha\gamma_5}{M}F_P + \gamma_5\frac{(p+p')_\alpha}{M}F_T, \quad (2.42)$$

where the four-momentum transfer between the incoming and the outgoing particles $q = k - k' = p' - p$, the anomalous magnetic moment $\xi = \mu_p - \mu_n = 3.708$, and M is the nucleon mass. The unknowns are the six form factors F_S (induced scalar), F_P (induced pseudoscalar), F_V^1 (isovector Dirac), F_V^2 (isovector Pauli), F_A (axial vector),

and F_T (induced tensor). They are scalar functions of q^2 only. We can square the hadronic current to obtain the covariant hadronic tensor $W_{\alpha\beta}$:

$$\begin{aligned}
W_{\alpha\beta} &= J_\alpha^{0\dagger} J_\beta^0 \\
&= -2g_{\alpha\beta} \left[|F_A|^2(4M^2 - q^2) - |F_V^1|^2 q^2 - \xi^2 |F_V^2|^2 q^2 - 2\xi \text{Re}(F_V^1 F_V^{2*}) q^2 \right] \\
&\quad + p_\alpha p_\beta \left[8|F_V^1|^2 + 8|F_A|^2 - (2\xi^2 |F_V^2|^2 + 8|F_T|^2) \frac{q^2}{M^2} \right] \\
&\quad + (p_\alpha q_\beta + p_\beta q_\alpha) \left[4|F_V^1|^2 + 4|F_A|^2 + 8\text{Re}(F_V^1 F_S^*) - 8\text{Re}(F_T^* F_A) \right. \\
&\quad \left. + \left(-\xi^2 |F_V^2|^2 - 4|F_T|^2 + 2\xi \text{Re}(F_V^2 F_S^*) - 4\text{Re}(F_T^* F_P) \right) \frac{q^2}{M^2} \right] \\
&\quad - \frac{q_\alpha q_\beta}{2M^2} \left[\left(\xi^2 |F_V^2|^2 (4M^2 + q^2) + 4(2M^2 \xi \text{Re}(F_V^1 F_V^{2*}) - 4M^2 \text{Re}(F_V^1 F_S^*)) \right. \right. \\
&\quad \left. \left. + 4M^2 \text{Re}(F_T^* F_A) + 4M^2 \text{Re}(F_A F_P^*) \right) \right. \\
&\quad \left. + 4 \left(|F_T|^2 + |F_P|^2 - \xi \text{Re}(F_V^2 F_S^*) + 2\text{Re}(F_T^* F_P) \right) q^2 + |F_S|^2 (-4M^2 + q^2) \right] \\
&\quad - 8i\epsilon_{\gamma\delta\alpha\beta} p_\gamma q_\delta \left[\text{Re}(F_V^1 F_A^*) + \xi \text{Re}(F_V^2 F_A^*) \right] \\
&\quad - i(p_\alpha q_\beta - p_\beta q_\alpha) \\
&\quad \times \left[8\text{Im}(F_V^1 F_S^*) + 8\text{Im}(F_T^* F_A) + (2\xi \text{Im}(F_V^2 F_S^*) + 4\text{Im}(F_T^* F_P)) \frac{q^2}{M^2} \right].
\end{aligned} \tag{2.43}$$

Then we compare the hadronic tensor in Eq. 2.43 to the general form of the hadronic tensor from Eq. 2.12. One gets the relations between the general form factors, V_i , in the hadron interaction to the one from the QE as follow:

$$V_1 = 2 \left[|F_A|^2(4M^2 - q^2) - |F_V^1|^2 q^2 - \xi^2 |F_V^2|^2 q^2 - 2\xi \text{Re}(F_V^1 F_V^{2*}) q^2 \right], \tag{2.44}$$

$$V_2 = \left[8|F_V^1|^2 + 8|F_A|^2 - (2\xi^2 |F_V^2|^2 + 8|F_T|^2) \frac{q^2}{M^2} \right], \tag{2.45}$$

$$V_3 = \left[4|F_V^1|^2 + 4|F_A|^2 + 8\text{Re}(F_V^1 F_S^*) - 8\text{Re}(F_T^* F_A) \right]$$

$$+ \left(-\xi^2 |F_V^2|^2 - 4|F_T|^2 + 2\xi \text{Re}(F_V^2 F_S^*) - 4\text{Re}(F_T^* F_P) \right) \frac{q^2}{M^2} \Big], \quad (2.46)$$

$$\begin{aligned} V_4 = & -\frac{1}{2M^2} \left[(\xi^2 |F_V^2|^2 (4M^2 + q^2) + 4(2M^2 \xi \text{Re}(F_V^1 F_V^{2*}) - 4M^2 \text{Re}(F_V^1 F_S^*)) \right. \\ & + 4M^2 \text{Re}(F_T^* F_A) + 4M^2 \text{Re}(F_A F_P^*)) \\ & + 4 \left(|F_T|^2 + |F_P|^2 - \xi \text{Re}(F_V^2 F_S^*) + 2\text{Re}(F_T^* F_P) \right) q^2 \\ & \left. + |F_S|^2 (-4M^2 + q^2) \right], \quad (2.47) \end{aligned}$$

$$V_5 = 8 \left[\text{Re}(F_V^1 F_A^*) + \xi \text{Re}(F_V^2 F_A^*) \right], \quad (2.48)$$

$$V_6 = -\left(8\text{Im}(F_V^1 F_S^*) + 8\text{Im}(F_T^* F_A) + (2\xi \text{Im}(F_V^2 F_S^*) + 4\text{Im}(F_T^* F_P)) \frac{q^2}{M^2} \right). \quad (2.49)$$

After the contraction between the lepton tensor and hadronic tensor, the neutrino quasi-elastic scattering differential cross section for interactions in Eq. 2.39 and 2.40 can be written in terms of these six form factors as:

$$\frac{d\sigma}{d|q^2|} \left(\begin{array}{l} \nu n \rightarrow l^- p \\ \bar{\nu} p \rightarrow l^+ n \end{array} \right) = \frac{M^2 G_F^2 \cos^2 \theta_c}{8\pi E_{\nu, \bar{\nu}}^2} \left[A(q^2) \mp B(q^2) \frac{(s-u)}{M^2} + \frac{C(q^2)(s-u)^2}{M^4} \right], \quad (2.50)$$

where $s - u = 4ME_\nu + q^2 - m_\mu^2$. The $+(-)$ sign corresponds to anti-neutrino-proton (neutrino-neutron) scattering. A, B and C are functions of Q^2 and are related to the form factors.

$$\begin{aligned} A = & \frac{(m^2 - q^2)}{4M^2} \left[\left(4 - \frac{q^2}{M^2} \right) |F_A|^2 - \left(4 + \frac{q^2}{M^2} \right) |F_V^1|^2 - \frac{q^2}{M^2} |\xi F_V^2|^2 \left(1 + \frac{q^2}{4M^2} \right) \right. \\ & - \frac{4q^2 \xi \text{Re}(F_V^{1*} F_V^2)}{M^2} + \frac{q^2}{M^2} \left(4 - \frac{q^2}{M^2} \right) |F_T|^2 \\ & \left. - \frac{m^2}{M^2} \left(|F_V^1 + \xi F_V^2|^2 + |F_A + 2F_P|^2 - \left(4 - \frac{q^2}{M^2} \right) (|F_S|^2 + |F_P|^2) \right) \right], \end{aligned}$$

$$\begin{aligned}
B &= \frac{q^2}{M^2} \text{Re}[F_A^*(F_V^1 + \xi F_V^2)] - \frac{m^2}{M^2} \text{Re} \left[(F_V^1 + \frac{q^2}{4M^2} \xi F_V^2)^* F_S - (F_A + \frac{q^2 F_P}{2M^2})^* F_T \right], \\
C &= \frac{1}{4} \left(|F_A|^2 + |F_V^1|^2 - \frac{q^2}{M^2} \left| \frac{\xi F_V^2}{2} \right|^2 - \frac{q^2}{M^2} |F_T|^2 \right), \tag{2.51}
\end{aligned}$$

where m is the muon mass (m_μ).

2.3.2 Electric and Magnetic Form Factors

In order to study the quasi-elastic interaction, various hypotheses about the hardronic current restrict the form factors as follows [16]:

1. Time-reversal invariance of vector current conservation requires that all form factors are real.
2. Charge symmetry yields F_V^1 , F_V^2 , F_A and F_P are real ($F_V^1 = F_V^{1*}$), and F_S and F_T are imaginary ($F_S = -F_S^*$).
3. No second-class currents implies F_S and F_T to be zero.
4. Conserved vector current (CVC) requires $F_S = 0$.
5. Isotriplet current

$$F_V^1(q^2) = F_1^p(q^2) - F_1^n(q^2) \rightarrow \text{Dirac electromagnetic isovector form factor.}$$

$$F_V^2(q^2) = \frac{\mu_p F_2^p(q^2) - \mu_n F_2^n(q^2)}{\mu_p - \mu_n} \rightarrow \text{Pauli electromagnetic isovector form factor.}$$

The form factors can be expressed in terms of the Sachs form factors as follows:

$$\begin{aligned}
F_V^1(q^2) &= \frac{G_E^V(q^2) - \frac{q^2}{4M^2} G_M^V(q^2)}{1 - \frac{q^2}{4M^2}}, \text{ and} \\
\xi F_V^2(q^2) &= \frac{G_M^V(q^2) - G_E^V(q^2)}{1 - \frac{q^2}{4M^2}}. \tag{2.52}
\end{aligned}$$

A reasonable fit to low energy data can be obtained if we assume:

$$\begin{aligned} G_E^V(q^2) &= \frac{1}{\left(1 - \frac{q^2}{M_V^2}\right)^2}, \\ G_M^V(q^2) &= \frac{1 + \mu_p - \mu_n}{\left(1 - \frac{q^2}{M_V^2}\right)^2}, \end{aligned} \quad (2.53)$$

with a vector mass $M_V = 0.84$ GeV. The axial vector form factor is given by:

$$F_A(q^2) = \frac{F_A(0)}{\left(1 - \frac{q^2}{M_A^2}\right)^2}, \quad (2.54)$$

with an axial vector mass $M_A = 1.03$ GeV and $F_A(0) = -1.23$. A reasonable approximation for all q^2 is given by:

$$F_P(q^2) = \frac{2M^2 F_A(q^2)}{M_\pi^2 - q^2}, \quad (2.55)$$

where $M_\pi = 0.134$ GeV is a pion mass.

Using these assumptions to simplify the analysis of the quasi-elastic interaction and neglecting the muon mass, the differential cross section for the quasi-elastic (Eq. 2.50) can be expressed in terms of three complex form factors (F_A , F_V^1 and F_V^2). A, B and C terms are reduced to:

$$\begin{aligned} A &= \frac{-q^2}{4M^2} \left[\left(4 - \frac{q^2}{M^2}\right) |F_A|^2 - \left(4 + \frac{q^2}{M^2}\right) |F_V^1|^2 - \frac{q^2}{M^2} \left(1 + \frac{q^2}{4M^2}\right) |\xi F_V^2|^2 \right. \\ &\quad \left. - \frac{4q^2}{M^2} (F_V^1 \xi F_V^2) \right], \\ B &= \frac{q^2}{4M^2} F_A (F_V^1 + \xi F_V^2), \end{aligned}$$

$$C = \frac{1}{4} \left(|F_A|^2 + |F_V^1|^2 - \frac{q^2}{4M^2} |\xi F_V^2|^2 \right). \quad (2.56)$$

The cross section in Eq. 2.50 corresponds to free-nucleon $\nu/\bar{\nu}$ interactions. There must be a correction for Pauli exclusion principle and Fermi motion of nucleons in the nuclei known as “*nuclear effects*”.

2.3.3 Nuclear Effects

At low energy region where the QE dominates, there are some nuclear effects need to be accounted for. The most important nuclear effects are due to

1. The Fermi motion
2. The Pauli exclusion principle

The Fermi Motion

The simplest Fermi motion model is a Fermi gas model where the momentum distribution is constant up to the maximum Fermi momentum K_F and is zero above K_F . However, such a model does not account for a long tail in the momentum distribution outside the Fermi surface seen in electron scattering experiments. Bodek and Ritchie [5] modified the Fermi gas model to include a long momentum distribution tail. We use their model to account for the Fermi motion in our analysis. In that model, the normalized momentum distributions, $|\Phi(\vec{P})|^2$, are

$$|\Phi(\vec{P})|^2 = \begin{cases} \frac{1}{C} \left(1 - 6 \left(\frac{K_F a}{\pi} \right)^2 \right) & \text{for } 0 < |\vec{P}| < K_F \\ \frac{1}{C} \left(2R \left(\frac{K_F a}{\pi} \right)^2 \left(\frac{K_F}{P} \right)^4 \right) & \text{for } K_F < |\vec{P}| < 4 \text{ GeV}/c \\ 0 & \text{for } |\vec{P}| > 4 \text{ GeV}/c \end{cases} \quad (2.57)$$

where $a = 2(\text{GeV}/c)^{-1}$, $C = \frac{4}{3}\pi K_F^3$, and $R = \frac{1}{(1-K_F/4)}$. The probability $|\Phi(P)|^2$ satisfy the normalization

$$\int_0^{4\text{GeV}/c} |\Phi(\vec{P})|^2 4\pi P^2 dP = 1 \quad (2.58)$$

The momentum distributions of protons and neutrons are defined as follows:

$$K_F^p = K_F \left(\frac{2Z}{A} \right)^{1/3} \quad (2.59)$$

$$K_F^n = K_F \left(\frac{2N}{A} \right)^{1/3} \quad (2.60)$$

where Z, N , and $A = Z + N$ are the number of protons, neutrons, and nucleons, respectively. The momentum distributions for iron (^{56}Fe) is $K_F^{56\text{Fe}} = 0.257 \text{ GeV}/c$.

The Pauli Suppression

For the Pauli suppression [16] we simply use the simple Fermi gas model to account for suppression at very small energy transfer. The cross section per neutron is equal to the cross section on a free neutron multiplied by $1 - \frac{D}{N}$ where

$$D = \begin{cases} Z & \text{for } w < \frac{u-v}{2} \\ \frac{A}{2} \left(1 - \frac{3w}{4}(u^2 + v^2) + \frac{w^3}{2} - \frac{3}{32w}(u^2 - v^2)^2 \right) & \text{for } \frac{u-v}{2} < w < \frac{u+v}{2} \\ 0 & \text{for } w > \frac{u+v}{2}, \end{cases} \quad (2.61)$$

where $u = \left(\frac{2N}{A}\right)^{1/3}$, $v = \left(\frac{2Z}{A}\right)^{1/3}$, $w = \frac{|q|}{2K_F}$, and q is the momentum transfer of the system ³ and $K_F = 0.257$ is the Fermi momentum from [5]. Z, N , and $A = Z + N$

³In Ref. [16], the terms $\frac{w^3}{2}$ was $\frac{w^3}{3}$.

are the number of protons, neutrons, and nucleons, respectively. For protons the multiplicative factor becomes $1 - \frac{D}{Z}$.

2.4 Resonances Process

In a low energy scattering region ($W \approx 2\text{GeV}$) three constituent quarks can remain bounded inside a nucleon. The neutrino-nucleon scattering process in this region can excite the quarks from ground state to excited state and produce resonances such as Δ 's or N^* 's particles. These particles then decay into pions and nucleons. The number of pions produced depends on the energy of the incoming neutrino and the state produced. Unlike the quasi-elastic scattering process, the resonances processes involve both proton and neutron for neutrino and anti-neutrino scattering processes.

2.4.1 RES Productions

For neutrino energies of a few GeV the single-pion production proceeds mainly through the excitation of the low mass resonances. The main contribution to the cross section comes from the production and the subsequent decay of the $\Delta(1232)P_{33}$ resonance. However, some of the channels receive a non-negligible contribution from the isospin 1/2 resonances as, for example, the $N(1440)P_{11}$ and the $N(1535)S_{11}$ resonances.

The resonances process is largely dominated by Δ^{++} excitation for neutrino scattering off proton and by Δ^- excitation for anti-neutrino scattering off neutron. Figure 2.6 shows the Δ excitation processes for neutrino (anti-neutrino) scattering off proton (neutron). There are also processes which involves Δ^+ excitation for neutrino scat-

tering off neutron and Δ^0 excitation for anti-neutrino scattering off proton. The examples of RES processes are shown in Eq. 2.62.

$$\begin{aligned}
 \nu_\mu + p(uud) &\rightarrow \mu^- + \Delta^{++}(uuu) \\
 \bar{\nu}_\mu + n(udd) &\rightarrow \mu^+ + \Delta^-(ddd) \\
 \nu_\mu + n(udd) &\rightarrow \mu^- + \Delta^+(uud) \\
 \bar{\nu}_\mu + p(uud) &\rightarrow \mu^+ + \Delta^0(ddd)
 \end{aligned} \tag{2.62}$$

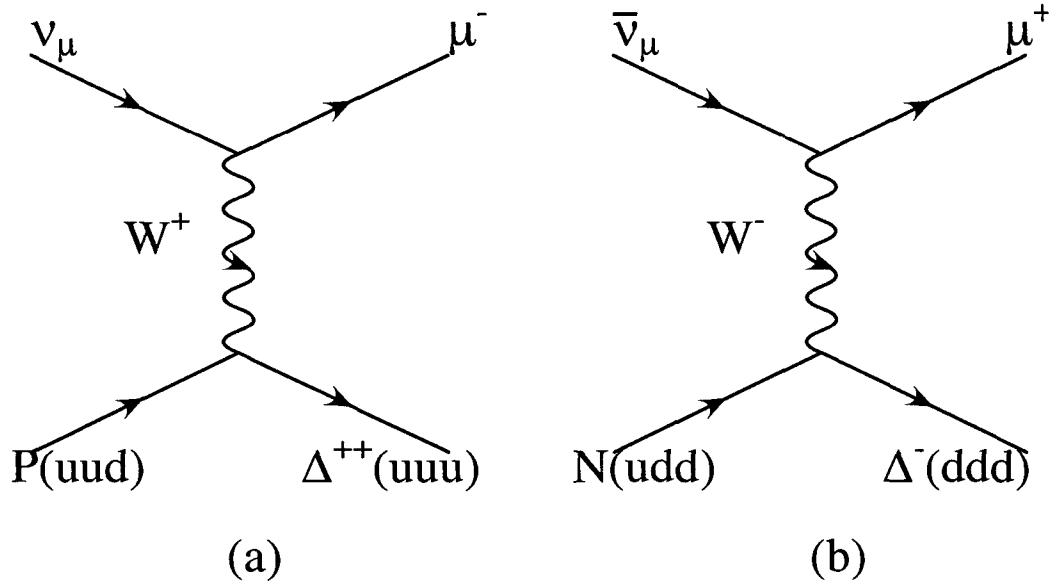


Figure 2.6: Schematic diagram of lepton-nucleon for resonances process which produce delta particles via the exchange of a vector boson (W).

The Δ particles then decay into a pion and a nucleon which leads to a single pion production in the final state. The followings show the possibility for inelastic neutrino (anti-neutrino)-nucleon scattering off proton and neutron in the charged current in-

teraction where the final hadronic state consist of a nucleon accompanied by a single pion as shown in Fig. 2.7 and Eq. 2.63.

$$\begin{aligned}
 \nu_\mu + p &\rightarrow \mu^- + p + \pi^+ \\
 \nu_\mu + n &\rightarrow \mu^- + p + \pi^0 \\
 \nu_\mu + n &\rightarrow \mu^- + n + \pi^+ \\
 \bar{\nu}_\mu + n &\rightarrow \mu^+ + n + \pi^- \\
 \bar{\nu}_\mu + p &\rightarrow \mu^+ + n + \pi^0 \\
 \bar{\nu}_\mu + p &\rightarrow \mu^+ + p + \pi^-
 \end{aligned}
 \tag{2.63}$$

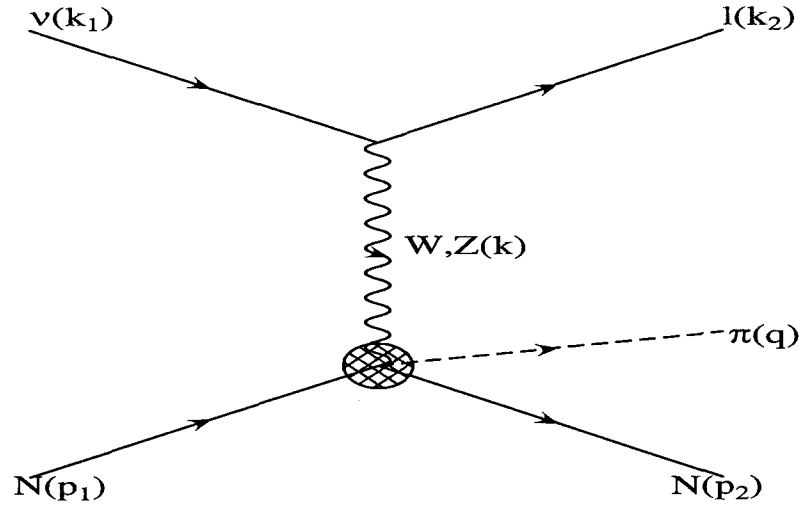


Figure 2.7: Schematic diagram of lepton-nucleon neutrino-induced single pion production off nucleons via the exchange of a vector boson (Z and W).

All these interactions are expected to dominate the nucleon resonances if the pion-

nucleon invariant energy does not exceed 2 GeV ($W < 2 \text{ GeV}$).

2.4.2 RES Cross section for 1π using Albright Model

Consider the neutrino excitation of a single nonstrange nucleon resonances by either charged or neutral weak currents [17, 18, 19],

$$\nu(k) + N(p) \rightarrow l(k') + N^*(p') \quad (2.64)$$

ν is the incoming neutrino, l is either charged or neutral scattered lepton, N and N^* are the nucleon before scattering and resonances nucleon. The matrix element of resonances in $\nu - N$ scattering can be written as a product of the hadronic weak current and the leptonic current,

$$M(\nu N \rightarrow l N^*) = \frac{G_F \cos \theta_c}{\sqrt{2}} \langle N^*(p') | J_\alpha | N(p) \rangle \langle \bar{u}_\mu(k') | \gamma_\alpha (1 - \gamma_5) | u_\nu(k) \rangle. \quad (2.65)$$

G_F is the Fermi constant and θ_c is the Cabibbo angle. The leptonic part is the same as the one in DIS and QE processes. For Δ production J_α is the hadronic current which contains a vector and an axial vector and can be written in terms of eight form factors under the assumption of a local $V - A$ lepton current. The hadron current is given by [19] :

$$\begin{aligned} \langle \Delta | J_\alpha | N \rangle = & \bar{\psi}_\sigma \left[\delta_{\sigma\alpha} (F_1^A + F_1^V \gamma_5) + \frac{i p_\sigma \gamma_\alpha (F_2^A + F_2^V \gamma_5)}{M} \right. \\ & + \frac{p_\sigma (p + p')_\alpha (F_3^A + F_3^V \gamma_5)}{M^2} \\ & \left. + \frac{p_\sigma (p - p')_\alpha (F_4^A + F_4^V \gamma_5)}{M^2} \right] u_N, \end{aligned} \quad (2.66)$$

where $M = M_1 + M_2$. The adjoint matrix element is found to be:

$$\begin{aligned} \langle \Delta | J_\beta | N \rangle^\dagger = & \bar{u}_N \left[-\delta_{\rho\beta} (F_1^{A*} - F_1^{V*} \gamma_5) - \frac{i p_\rho \gamma_\beta (F_2^{A*} - F_2^{V*} \gamma_5)}{M} \right. \\ & - \frac{p_\rho (p + p')_\beta (F_3^{A*} - F_3^{V*} \gamma_5)}{M^2} \\ & \left. - \frac{p_\rho (p - p')_\beta (F_4^{A*} - F_4^{V*} \gamma_5)}{M^2} \right] \psi_\rho. \end{aligned} \quad (2.67)$$

The summation over the Δ spin states is carried out with the spin- $\frac{3}{2}$ projection operator:

$$\begin{aligned} \sum_\lambda \psi_\rho^{(\lambda)} \bar{\psi}_\sigma^{(\lambda)} = & \left\{ \delta_{\rho\sigma} + \frac{2 p'_\rho p'_\sigma}{3 M_2^2} - \frac{1}{3} \gamma_\rho \gamma_\sigma \right. \\ & \left. - \frac{i}{3 M_2} (\gamma_\rho p'_\sigma - \gamma_\sigma p'_\rho) \right\} \frac{-i \gamma \cdot p' + M_2}{2 M_2}. \end{aligned} \quad (2.68)$$

The differential cross section in the limit that $q^2 \rightarrow 0$ is illustrated as follows:

$$\begin{aligned} \frac{d\sigma}{dq^2} = & \frac{G_F^2}{12\pi} \left(\frac{s - M_2^2}{s - M_1^2} \right) \left(\frac{M_1 + M_2}{M_2} \right)^2 \\ & \times \left\{ |F_1^A|^2 + 2 \left(\frac{M_2 - M_1}{M_1 + M_2} \right) \text{Re}(F_1^A F_2^{A*} + F_1^A F_3^{A*}) \right. \\ & + \left(\frac{M_2 - M_1}{M_1 + M_2} \right)^2 [|F_2^A|^2 + |F_3^A|^2 + |F_1^V|^2 + |F_2^V|^2 + 2 \text{Re}(F_2^A F_3^{A*} + F_1^V F_2^{V*})] \\ & \left. + 2 \left(\frac{M_2 - M_1}{M_1 + M_2} \right)^3 \text{Re}(F_1^V F_3^{V*} + F_2^V F_3^{V*}) + \left(\frac{M_2 - M_1}{M_1 + M_2} \right)^4 |F_3^V|^2 \right\}. \end{aligned} \quad (2.69)$$

Terms proportional to $\frac{m_l}{(M_1 + M_2)^2}$ are neglected. The $F_4^{V,A}$ do not contribute because their coefficients are proportional to the lepton mass.

Rein and Sehgal have classified all the resonances productions with a single pion in the final state [17]. From the differential cross sections in terms of resonances excitation

matrix element, they adopt the quark model proposed by Feynman, Kislinger, and Ravndal [20] (FKR). FKR-model depicts the basic quark-quark interaction as an oscillator potential. The transition matrix elements are then determined by the current operators.

2.5 Higher Twist Model

The non-perturbative higher twist effects arise from inter-quark interactions in the nucleon. There are two sources of non-perturbative effects, the target mass [21, 22, 23] and the higher twist effects [24, 25, 26, 27, 28, 29]. The target mass effects are called kinematic higher twist effects and the higher twist effects are called dynamic higher twist effects.

2.5.1 Target Mass Effect

In the QPM, the partons are assumed to be massless. The Bjorken scaling variable, x or the fractional nucleon momentum carried by the struck quark, does not hold when the scattering occur at very large x and low Q^2 , $Q^2 \approx M_N^2$. At $x \approx 1$, the mass of the struck quark is effectively the same as the nucleon mass. One cannot ignore M_N at low Q^2 .

Due to the target mass effect at large x and small Q^2 the fractional momentum, ξ , carried by parton in QPM is related to the Bjorken variable x by:

$$\xi = \frac{xQ^2}{0.5Q^2(1 + [1 + \frac{(2M_Nx)^2}{Q^2}]^{\frac{1}{2}})}, \quad (2.70)$$

where

$$2Q'^2 = [Q^2 + M_f^2 - M_i^2] + [(Q^2 + M_f^2 - M_i^2)^2 + 4Q^2(M_i^2 + P_T^2)]^{\frac{1}{2}}. \quad (2.71)$$

M_i is the initial parton mass with average initial transverse momentum P_T and M_f is the mass of final parton [21].

2.5.2 Higher Twist Effect

The lepton-nucleon scattering at low Q^2 involves double partons scattering (scattering from two partons at the same time). At low Q^2 the virtual gauge boson does not have enough energy to probe a single parton inside the nucleon. These higher twist processes are suppressed by powers of $1/Q^2$.

In the HT process there is a cross link between the struck quark and the spectator quarks via a gluon propagator as shown in Fig 2.8. HT model is a bridge that connects the DIS processes at high energy to the RES processes at low momentum transfer and low hadronic mass. We obtain the HT events by reweighting the DIS with some factor at certain value of x .

The quark distributions inside the nucleon are parametrized as standard Parton Distribution Functions (PDFs) obtained from global fits to various set of data at very high energies. These fits are done within the theory of Quantum Chromodynamics with leading order (LO) or next to leading order (NLO). Most of high energy data come from DIS processes of electron/muon scattering experiments on hydrogen and deuterium, and neutrino experiments on nuclear targets with x less than 0.75.

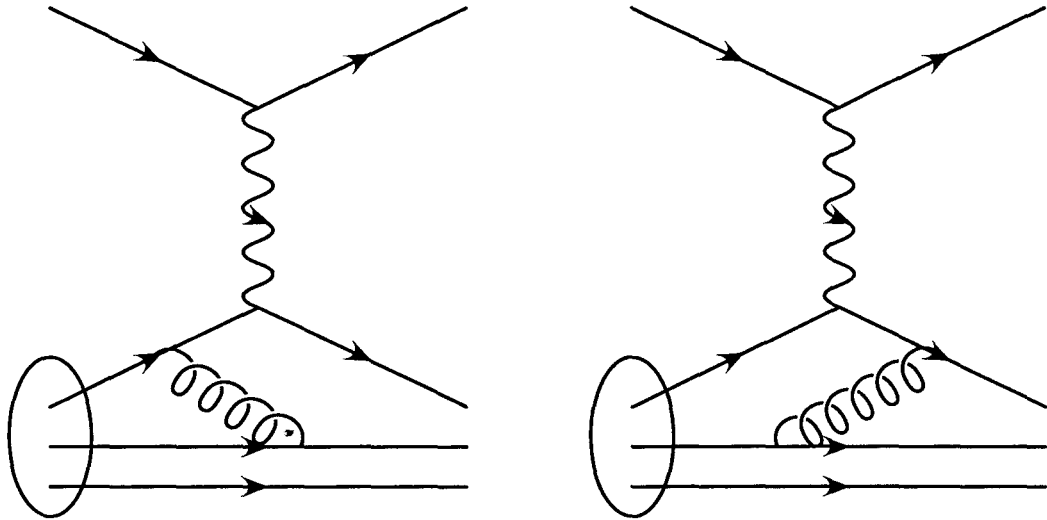


Figure 2.8: Schematic diagrams of lepton-nucleon in higher twist processes.

There are a lot of attempts to modify and make corrections to the leading order PDFs such that they can be used to model electron, muon, and neutrino inelastic scattering cross sections both at very low and high energies. Phenomenologists have studied the SLAC high x data and Q^2 between 7 and 31 GeV^2 which are in a region where non-perturbative effects can be very large [24, 25].

2.5.3 Cross Section using Modified PDF+HT

The HT model has been parametrized to fit the average cross section in the resonances region. Previous study [30] shows that it is more accurate than the single-pion production model from Rein and Sehgal [17].

The higher twist effects are measured by comparing SLAC electron scattering and BCDMS muon scattering measurements of $F_2(x, Q^2)$ to the model expectation and fitting deviations to the form $1 + ht(x)/Q^2$.⁴ The fit gives

$$ht(x) = \begin{cases} 0 & \text{for } x < 0.4 \text{ and } ht < 0 \\ 0.672\left(\frac{x^{1.893}}{1-1.138x} - 0.236\right) & \text{for } x \leq 0.8 \\ 10 & \text{for } x > 0.8 \end{cases} \quad (2.72)$$

These corrections increase the CC cross section at high x and low Q^2 ,

$$\frac{d^2\sigma}{dxdy} \rightarrow \frac{d^2\sigma}{dxdy} \cdot \left(1 + \frac{ht(x)}{Q^2}\right) \quad (2.73)$$

Equation 2.73 describes the DIS data in high Q^2 region well. It also well describes resonances data at low Q^2 region.

⁴Another way to describe the low energy data and account for HT effects is done by

1. Increase the d/u ratio at high x .
2. Rescale the scaling variable x by using $x_w = (Q^2+B)/(2M\nu+A)$ or $(x_w = x(Q^2+B)/(Q^2+Ax))$. Parameter A includes target mass and higher twist effects at high x . Parameter B allows the fits to go down to the photoproduction limit ($Q^2 = 0$).
3. Multiply all PDFs, F_1 , F_2 , and xF_3 , by a factor $Q^2/(Q^2 + C)$. This is done in order for the fits to describe low Q^2 data in the photoproduction limit.

Chapter 3

Experimental Apparatus

Neutrino interacts weakly with matter. There are two ways to increase the number of interaction:

- By increasing the neutrino beam intensity, and
- By increasing the size of the target.

The NuTeV experiment was designed to observe neutrino interactions from the highest energy, highest intensity sign selected neutrino beam ever produced. The NuTeV experiment observed approximately two million neutrino interactions in the detector. The NuTeV neutrino beam was produced from 800 GeV proton beam at the Fermilab Tevatron superconducting synchrotron ring. The proton beam was directed to hit a beryllium-oxide, BeO, target and produced a hadron shower. The hadron shower decays into secondary neutrino beam and charged particles. After passing through a kilometer of dirt which absorbed all charged particles, the neutrino beam hits the iron, Fe, target at the NuTeV detector located in the LabE/F hall. The NuTeV detector consisted of slices of steel plates and particle detectors. Even with hundreds

of slices of Fe target, only one in a billion neutrinos in the NuTeV neutrino beam interacted as it goes from the first to the last slice of steel plate.

3.1 Neutrino at the Fermilab Tevatron

The NuTeV neutrino-nucleon ($\nu - N$) deep inelastic scattering took place at Fermilab National Accelerator laboratory. Figure 3.1 shows the Fermilab Tevatron and the ν beam line. The proton passes through the following accelerators:

- The hydrogen atom is ionized to H^- ions;
- Cockroft-Walton electrostatic accelerator boosts the H^- ions to 750 KeV;
- The “*Linac*” (linear accelerator) boosts the 750 KeV proton beam to 200 MeV;
- The Booster, a 140 m diameter synchrotron ring, accelerates the proton beam to 8 GeV;
- The Main Ring, a 2 km diameter synchrotron ring, accelerates the proton beam to 150 GeV; and
- The Tevatron Ring, a superconducting synchrotron ring located below the Main Ring, accelerates the proton beam until it reaches 800 GeV.

After the proton passes through the accelerators and its energy reaches 800 GeV, the proton beam is sent to the neutrino beamline.

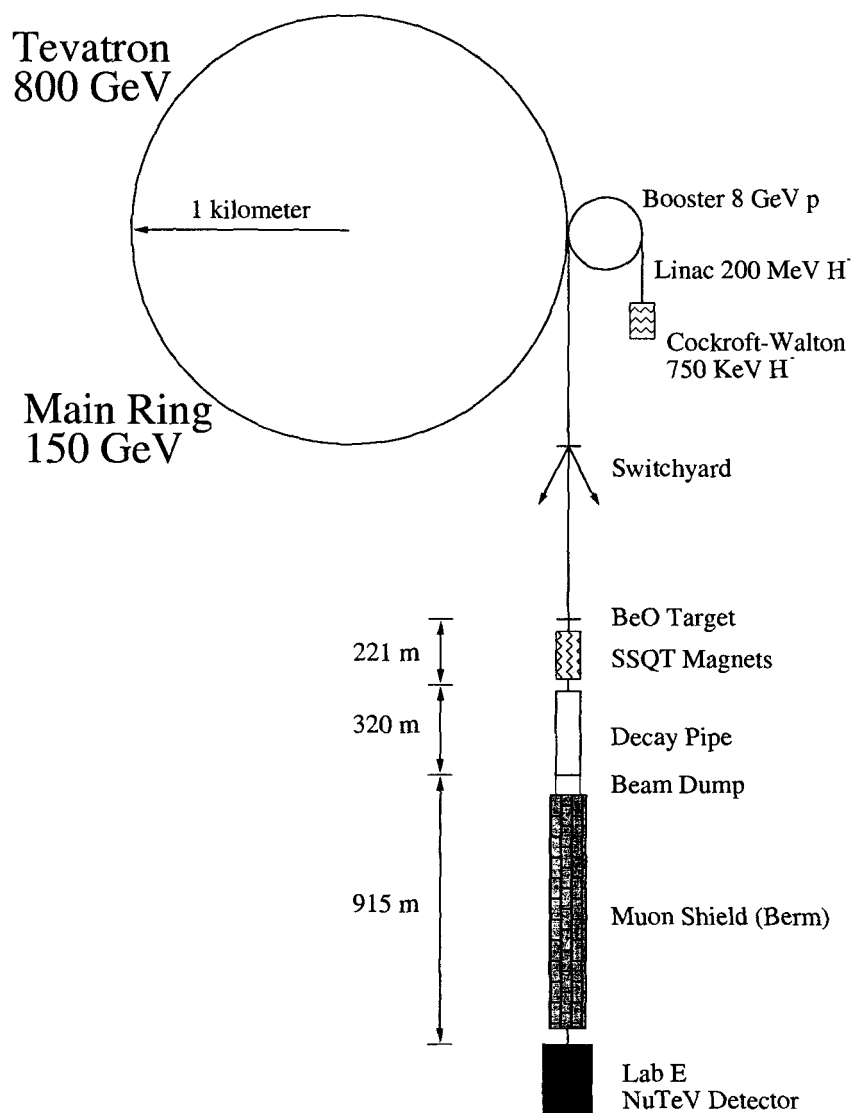


Figure 3.1: The NuTeV Beamline.

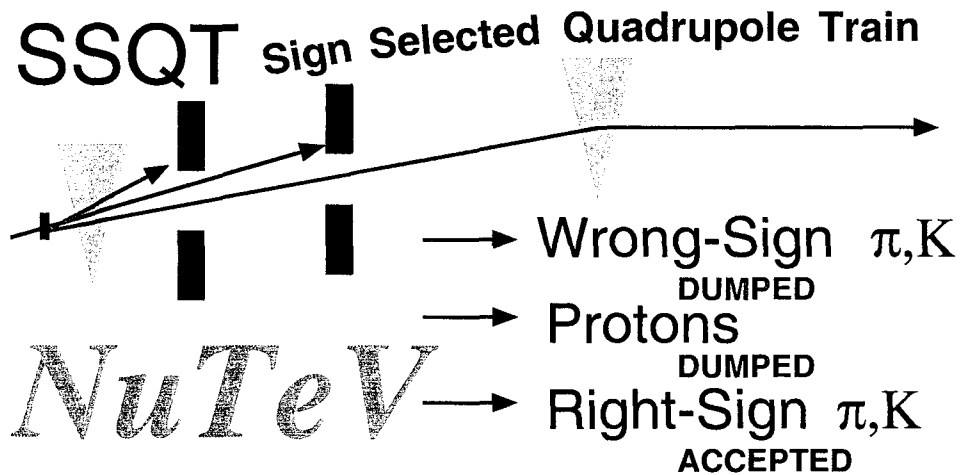


Figure 3.2: The NuTeV SSQT.

3.2 Neutrino Beamline

The proton beam from the Tevatron ring is directed onto a 33 cm long (1-interaction length) BeO target in the Neutrino Center beamline. The protons interact to produce a hadron shower, containing mostly pions and kaons. The long lived charged mesons are directed toward the detector and focused using a series of magnets called *sign-selected quadrupole train*, SSQT [1]. The SSQT is designed to select and focus the right charge (*“right-signed”* mesons). Figure 3.2 shows NuTeV sign-selected quadrupole train. It consists of six quadrupole magnets, two bending dipole magnets, and two iron beam dumps.

The SSQT dipoles bend charged π and K mesons down a beamline 7.8 mrad from the primary proton beam direction and direct the beam towards the LabE/F NuTeV detector. The *“wrong-signed”* mesons are bent in the opposite direction and dumped

Source	ν Mode	$\bar{\nu}$ Mode
$\pi^\pm, K^\pm \rightarrow \mu^\pm(\bar{\nu}_\mu)$	0.982	0.973
K_{e3}^\pm, π_{e2}^\pm	0.0157 ± 0.0003	0.0115 ± 0.0002
K_{Le3}, K_{Se3}	0.00065 ± 0.00007	0.00290 ± 0.00030
Charm Meson $\rightarrow \nu_e$	0.00042 ± 0.00006	0.00155 ± 0.00020
$\mu \rightarrow \nu_e$	0.00007 ± 0.00001	0.00010 ± 0.00001
$\Lambda_c, \Lambda, \Sigma$	0.00003 ± 0.00003	0.00023 ± 0.00020
Wrong Sign	0.00108	0.0029

Table 3.1: Fractional neutrino fluxes from various sources. All the data are from [32], except the wrong sign which is from [1].

into an iron block. The neutral particles and protons which do not interact hit another dump. The SSQT quadrupoles focus the “right-signed” mesons in both x and y directions to keep the mesons at the center of the beam. The focused beam is sent to the decay pipe where π and K mesons decay in flight into ν or $\bar{\nu}$ and charged particles. All charged particles are absorbed in the beam dump and the muon shield (earth berm) in front of LabE/F. Only ν or $\bar{\nu}$ get to the NuTeV detector. The NuTeV ν or $\bar{\nu}$ beam is not purely ν_μ or $\bar{\nu}_\mu$, but contain a small (10^{-2}) contamination of ν_e or $\bar{\nu}_e$ which comes from K_{e3}^\pm or K_{Le3} decay and a smaller (10^{-3}) [1, 31] contamination of $\bar{\nu}_\mu$ or ν_μ which comes from decay of wrong signed K^\pm . Table 3.1 lists the sources and the fractions of neutrinos in each beam with the estimated uncertainties.

3.3 NuTeV Detector

The NuTeV detector located 1.5 km downstream of the primary proton target at LabE/F consists of a 690 tons iron-scintillator calorimeter and a toroidal muon spectrometer (Fig. 3.3). The calorimeter serves as ν -target and is used to measure the energy of a hadronic shower and the position of muons as they traverse it. The

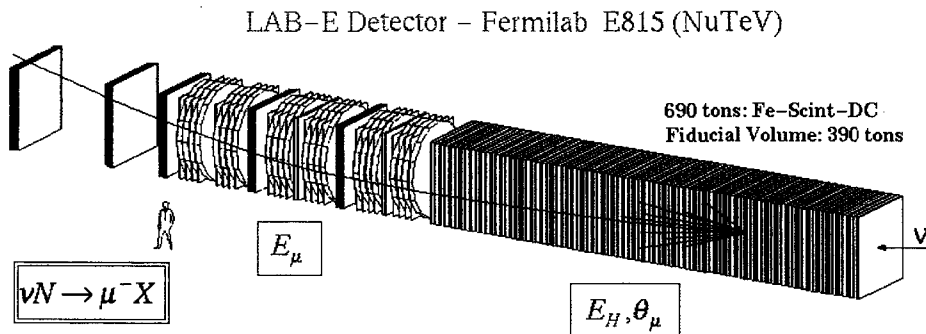


Figure 3.3: The NuTeV detector.

toroidal spectrometer is used to measure the momentum of the outgoing muons.

3.3.1 Target Calorimeter

The NuTeV target calorimeter is 3 m (H) x 3m (W) x 17.7 m (L) and weights approximately 690 tons. It consists of 168 steel plates with 84 liquid scintillation counters and 42 drift chambers spaced evenly throughout its volume. Two plates of steel are placed between every two consecutive scintillation counters and one drift chamber is between every other set of counters. One unit counter consists of a scintillation counter and two steel plates surrounding the scintillator; one unit calorimeter layer consists of two counters and a drift chamber as shown in Fig. 3.4. This unit calorimeter is repeated 42 times to make the calorimeter. Table 3.2 summarizes the calorimeter's composition [33] in terms of each component length, radiation length, and interaction length.

The muons must at least have 12 GeV to traverse all 84 scintillator planes. The calorimeter hadronic energy response and resolution are calibrated using the data from another beam called the “*calibration beam*” or “*test beam*”.

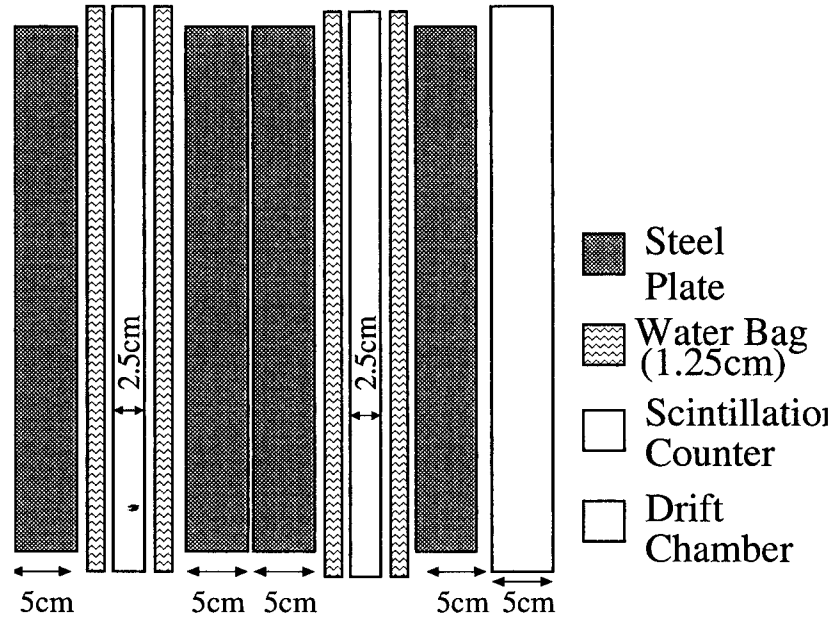


Figure 3.4: The NuTeV calorimeter.

Steel Plates

The 168 steel plates measuring 3 m (H) x 3 m (W) x 5.1 cm (L) are served as a massive target in which neutrino can interact.

Scintillation Counters

After the interaction occurs in the steel plates, the energy of the interaction is sampled by the scintillation counters. There are 84 liquid scintillation counter in the NuTeV detector, numbered from 84 to 1, starting at the upstream end of the calorimeter. Each counter is a 3 m (H) x 3 m (W) x 2.5 cm (L) Lucite box viewed by photomultiplier tubes (PMTs) mounted at each of the counter corners. 3 mm thick vertical Lucite ribs are used for structural support and spaced approximately 2.5-5.1 cm apart. The counters are staggered so that the ribs are not aligned on the transverse plane

Component	Length (cm)	Radiation Length (λ_{rad})	Interaction Length (λ_I)
4 Steel Plates	20.7	11.75	1.24
2 Scint. Counters	6.3	0.19	0.07
4 Water Bags	6.6	0.19	0.08
1 Drift Chamber	3.7	0.17	0.03
Total	37.3	12.30	1.42

Table 3.2: Composition of a NuTeV target calorimeter unit.

along the calorimeter's length. Figure 3.5 shows a schematic of a NuTeV scintillation counter.

Each counter is filled with roughly 65 gallons of Bicron 517L liquid scintillator oil. There are two plastic water-filled bags approximately 2.5 cm thick, one on each side of each counter, to produce support for the counters.

When a charged particle passing through the counter, it excites the primary fluors, which radiate ultraviolet light. The secondary fluors absorb the ultraviolet and emit visible blue light. The blue light is transmitted to the edges of the counters by total internal reflection. At the edges, there are one-half-inch-thick plastic bars, called "*wavelength shifter bars*" which absorb the blue light and re-emit green light. The wavelength shifter bars act as a wave guide to transfer the light to the four corners of the counter. The four PMTs at the corners collect the light output of the counter. The amount of light is then converted into the corresponding energy using calibration beam. The energy resolution for hadronic showers is $\frac{\sigma_E}{E} \approx \frac{0.86}{\sqrt{E(\text{GeV})}}$ [34].

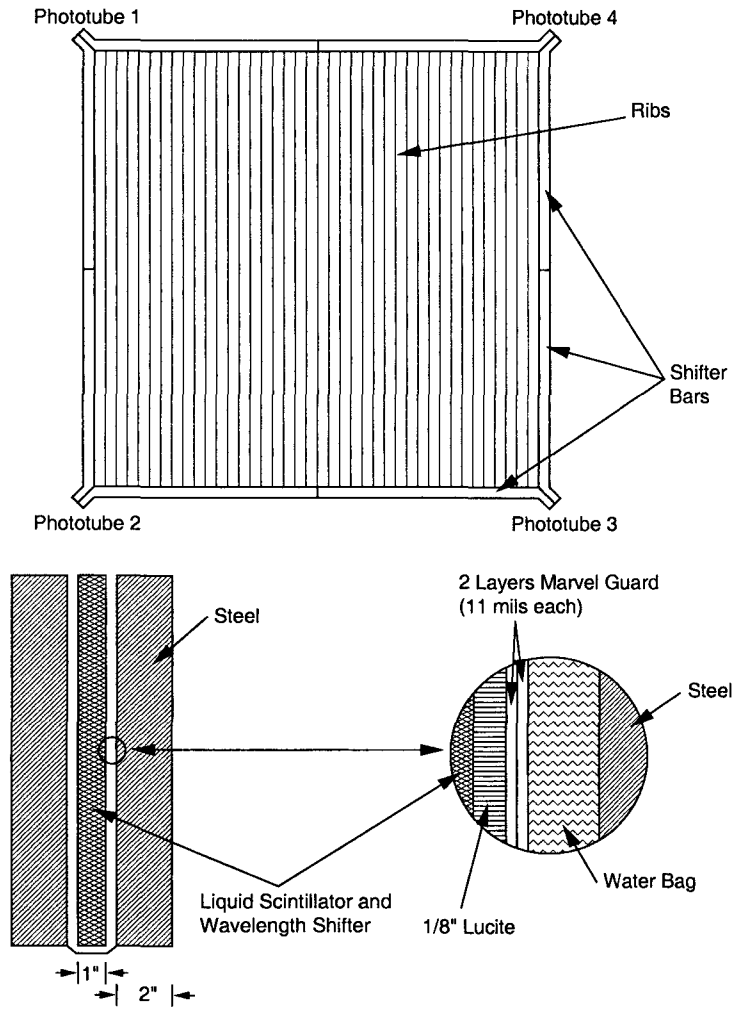


Figure 3.5: The scintillation counter.

Drift Chambers

Muons emerging from the neutrino interaction are tracked inside the calorimeter target by drift chambers. There are 42 drift chambers inter-spaced throughout the calorimeter which are used to measure the position of the outgoing muon as it traverses through the calorimeter. Each drift chamber has an active area of 3 m (H) x 3 m (W) and is comprised of 24 horizontal and 24 vertical cells. Each cell is 5 inches across and 0.75 inches thick and contains three wires in the center of the cell (two sense wires and one field wire). Figure 3.6 shows a cutaway view of a drift chamber cell. The upper and lower surfaces of each cell are covered with copper-clad G10 panels, which are milled to form a set of 19 cathode strips per cell. Strip voltage is supplied by I-beams at the edge of each cell which are held at -4500V. This voltage is distributed decrementally to each strip via a resistor card acting as a voltage divider; this maintains a uniform electric field across the drift space.

3.3.2 Toroidal Muon Spectrometer

The toroidal muon spectrometer is located at the end of the target calorimeter. The muon spectrometer consists of three large toroidal iron magnets and five sets of drift chambers. The toroidal magnets measure the momentum of the outgoing muon as it emerges from the calorimeter. At each magnet segment, there is a set of drift chambers which measure the position of the outgoing muon. Two additional sets of drift chambers at the end are used to measure the final angle of the muon after it bends in the magnets. The resolution of muon momentum is $\frac{\Delta P}{P} = 0.11$ [34].

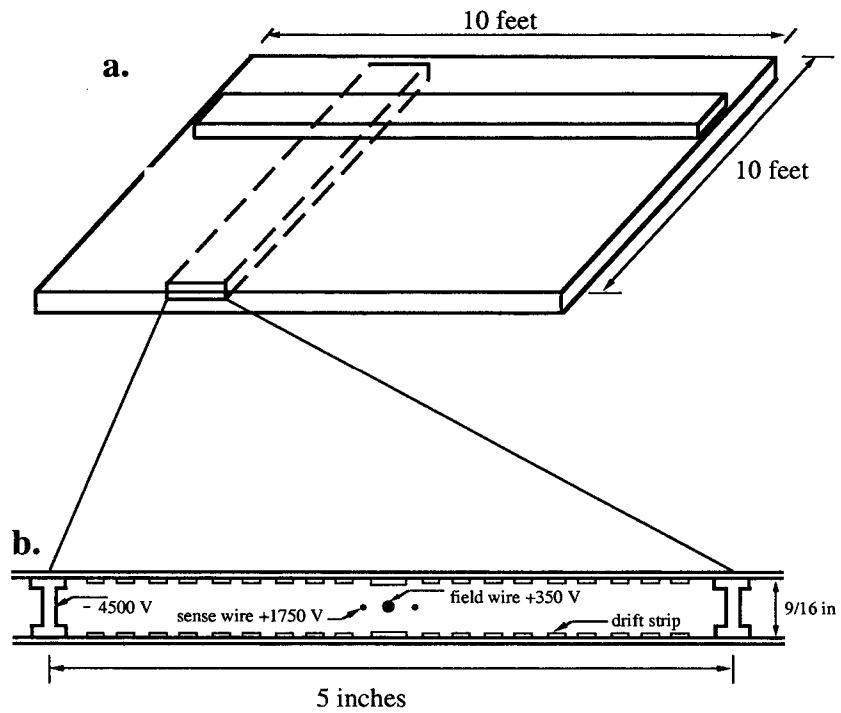


Figure 3.6: **a.** The target drift chamber top view. There are two orthogonally oriented planes consisting of three-wire cells. **b.** Cross section of a three wire drift chamber cell.

3.4 Trigger and Gate

The NuTeV trigger is designed to select various types of events which satisfy certain requirements called “*triggers*”. Each trigger initiates the digital signal and records the events if it occurs within a proper time window called a “*gate*” synchronized to the accelerator cycle.

3.4.1 Trigger

The NuTeV trigger provides information for a large variety of analysis topics. The trigger electronics signals comes from the four PMTs at the corners of each counter. The signals are combined in various ways to produce information. Table 3.3 shows a list of the different triggers and their descriptions.

3.4.2 Gate

There are four different kind of gates during an acceleration cycle:

- Pedestal Gate : pulser initiates random reads out the electronics when there is no beam passing through the detector;
- Cosmic Ray Gate : activates neutrino trigger when there is no beam (for cosmic ray background study);
- Fast Gate : contains five neutrino pings with neutrino trigger, each roughly is $1 - 2 \times 10^{12}$ proton on target; and
- Slow Gate : contains test beam events used for calibration of detector.

The total time for each acceleration cycle is approximately one minute (60.1 sec).

The neutrino beam occurs during the fast spill (covered by the fast gate) and consists

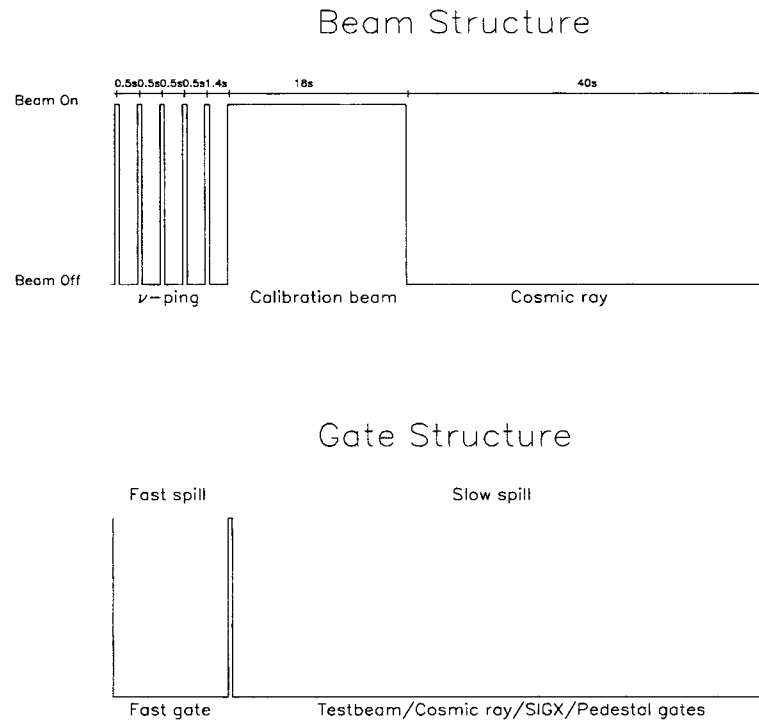


Figure 3.7: A schematic diagram of beam and gate timing structures. The fast spill contains neutrino events which are recorded within the fast gate. The slow gate, or testbeam gate, opens during the calibration beam for 18 s of the slow spill. The cosmic ray and pedestal data are taken during the rest of the acceleration cycle time when there is no beam.

of five 5 msec “buckets” or “pings” of protons on target. The pings are separated by 0.5 sec. The neutrino beam is separated from the the calibration beam by 1.4 sec. The slow spill includes the other three kind of gates and takes the remaining of the acceleration time. Figure 3.7 shows the beam and the gate structures.

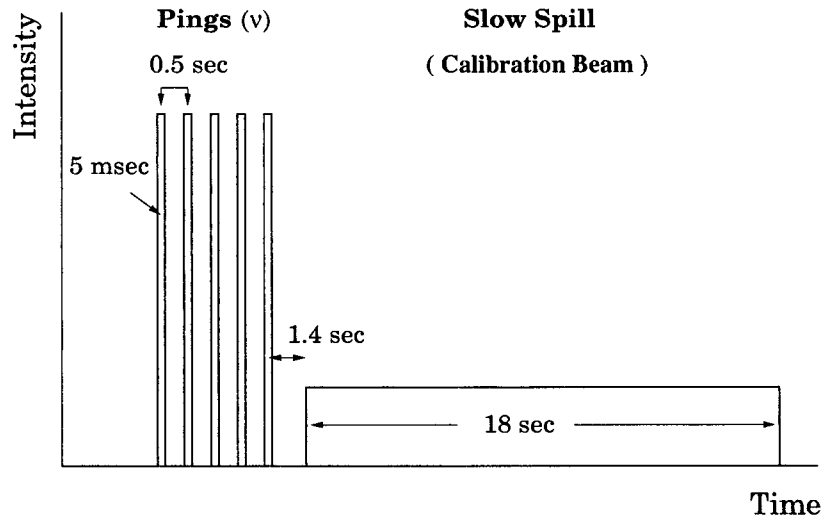


Figure 3.8: A schematic diagram of accelerator time structure of the fast and slow spills.

3.5 The Calibration or Test Beam

In order to measure the hadronic energy, we need to convert the light from the scintillators to the corresponding energy. NuTeV constructed another beam line called the calibration beam. Particles entered this beamline 1.4 s after the neutrino pings, but during the same 1-min accelerator cycle (Fig. 3.8). With a known momentum beam of hadrons, muons, and electrons, the energy resolution and response of the detector are measured directly.

The calibration beam period within one accelerator cycle is 18 s with uniformly distributed beam intensity. This calibration beamline is delivered by a beamline completely independent of the neutrino beamline. The calibration beam can produce high-purity beams of hadrons, muons, and electrons of energy ranging from 4.8 to

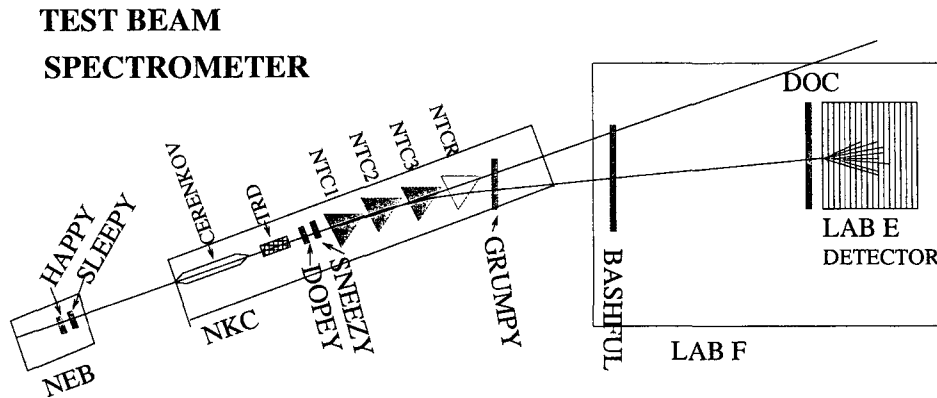


Figure 3.9: A schematic diagram of NuTeV calibration beam spectrometer system. There are seven drift chambers named as seven dwarfs. The distance between the most upstream chambers (HAPPY) in the spectrometer and the first momentum-analyzing magnet (NTC1) is 83.3 m, and the distance between the most downstream chamber (DOC) and the magnets (NTCR) is 69.2 m.

190 GeV.

The beamline is instrumented as a low mass spectrometer with a long lever arm as shown in Fig. 3.9. The calibration beam spectrometer consists of a number of drift chambers and dipole magnets, a Čerenkov counter and an array of transition radiation detectors (TRDs). The drift chambers are used to track the position of the charged particles. The dipole magnets are adjusted so that particles have correct momentum and are directed to the NuTeV detector. The Čerenkov counter and TRDs provide particle identification for pions, kaons, anti-protons, and electrons. When particle identification is not needed, these detectors are rolled out of the beamline and are replaced by a vacuum pipe to reduce multiple scattering.

<i>Trigger</i>	<i>Name</i>	<i>Requirements</i>
1	Charged-Current Trigger	<ul style="list-style-type: none"> • counters ON- upstream of toroid 1 • counters ON- in toroid gaps • no upstream veto
2	Neutral-Current Trigger	<ul style="list-style-type: none"> • $E_{had} > 5$ GeV in 8 consecutive counters • $E_{had} > 0.15$ GeV in 2 out of 4 consecutive counters • no upstream veto
3	Range-Out/Exit Trigger	<ul style="list-style-type: none"> • 1/4 MIP in more than 16 counters • 4 GeV energy in any 8 adjacent counters • no upstream veto
4	Charged-Current Trigger II	<ul style="list-style-type: none"> • shower energy • hits in first cart upstream of toroid • muon track through one toroid quadrant
5	Test Beam Trigger	<ul style="list-style-type: none"> • slow spill • no energy requirement in the calorimeter • test beam track
6	Straight through μ Trigger	<ul style="list-style-type: none"> • hits in each cart and one toroid quadrant
8	Cosmic Ray Trigger	<ul style="list-style-type: none"> • 40 counter muon requirement
10,11,12	Pedestal Triggers	<ul style="list-style-type: none"> • No other triggers+random pulser

Table 3.3: NuTeV trigger list with descriptions

Chapter 4

Data Analysis

This chapter describes how to reconstruct physical quantities of a charged current (CC) neutrino-nucleon ($\nu - N$) scattering process from the raw data. There are only three measurable kinematic variables relevant in the CC $\nu - N$ scattering events: the energy of the outgoing muon (E_μ), the angle of the outgoing muon (θ_μ), and the total energy of the hadronic shower in the final state (E_{had}). It is important to reconstruct these quantities correctly.

The NuTeV detector measures the pulse heights in each scintillation counter and also the hits in the drift chamber when muon traverses through the target calorimeter region. We then have to convert these information into physical quantities. E_{had} is calculated from the pulse heights while θ_μ is calculated from the track of the hits. The muon path through the toroid magnetic spectrometer is fitted to find the muon momentum (P_μ) which is then converted to E_μ . The following sections discuss how to reconstruct and analyze these three kinematic variables.

4.1 Hadron Energy Reconstruction

In $\nu - N$ inelastic scattering process when a neutrino scatters off a nucleon, the nucleon is broken and its constituents emerge in the form of hadrons, primarily pions, kaons, protons and neutrons. These secondary hadrons interact with the target calorimeter and produce a hadron shower. The fraction of shower energy deposited in the counters provides a sample of the total hadron shower energy.

The energy of the hadron shower is calculated by summing the energy registered in the calorimeter scintillation counters. The deposited energy includes energy from the hadron shower and energy loss by the muon. We calculate the actual hadron energy by subtracting the muon energy loss (E_{μ}^{loss}) from the energy deposited in the counter (E^{cntr}) as follows,

$$E_{had} = C_h \sum_{place}^{shend-5} (E^{cntr} - E_{\mu}^{loss}), \quad (4.1)$$

where $C_h = 0.212$ GeV/minimium-ionizing-particle (MIP) is the hadron energy conversion which converts from MIP to GeV ¹. The E_{μ}^{loss} is the restricted muon energy loss in the target which is a logarithmic function of E_{μ} and defined as follows:

$$E_{\mu}^{loss} = (0.9315 + 0.02359 \times \log E_{\mu}^{est}) / \cos \theta_{\mu}. \quad (4.2)$$

The estimated muon energy E_{μ}^{est} is assumed to be a linear function of the length of the active target calorimeter that muon goes through. We assume that the muon

¹The number of particles is roughly determined by measuring the summed of the pulse height registered by the four phototubes on each counter. The pulse height from each phototube is corrected for the position of the hit. This sum is then converted into units of MIPs. One MIP represents the average summed of the pulse heights resulting from a single particle passing through the counter. The pulse heights registered by the phototubes at each scintillation counter are proportional to the number of MIPs that pass through the counter.

losses approximately 6.7 GeV per 42 counters.

PLACE is a variable which defines the z location of the interaction. *PLACE* is the first counter downstream of the vertex where the neutrino interaction occurs. It is defined as the first of two consecutive counters with pulse heights of 4 or more MIPs. The vertex of the event is its transverse interaction position. The vertex positions (V_x , V_y and V_z) are measured by reconstructing the muon track and following it upstream to *PLACE*. *SHEND* is the most upstream counter which is followed by three consecutive counters with less than 4 MIPs. The counters are numbered starting with one at the front face (FF) of the toroid, and increasing to end at the most upstream counter, 84 (refer back to Fig. 3.3).

4.2 Muon Momentum Reconstruction

In a CC interaction, there are three different possibilities for the outgoing muon: the muon reaches the toroid spectrometer, the muon loses all its energy before reaching the toroid and stops in the calorimeter, or the muon exits the fiducial volume² before reaching the toroid.

When muon reaches the toroid spectrometer, it is bent due to the magnetic field. The momentum is determined from the amount of the bend. In a constant magnetic field

²The fiducial volume is defined as an active interaction region where we can analyze events well. Section 4.5.1 defines the fiducial volume.

B , the bend of the muon track is given by the following equation:

$$P = \frac{0.3BL}{\sin \theta}, \quad (4.3)$$

where P is the measured momentum (GeV/c), $L = R\Delta\theta$ is the length of the track in meters (R is the radius of curvature of the track), and θ is the angular bend of the track.

If a muon does not reach the toroid but rather loses all its energy in the calorimeter and stops, we can measure the muon energy directly from the energy deposited in the calorimeter along its track. This type of event is defined as “*rangeout*” sample.

If a muon track exits from the fiducial volume before it either reaches the toroid or loses all of its energy, the energy is calculated from the multiple scattering of the track (higher energy tracks tend to have less multiple scattering than a low energy track). This type of event is called “*exit*” sample.

In our analysis, the muon is required to go through the toroid spectrometer.

4.3 Muon Angle Reconstruction

In the target calorimeter region where there is no magnetic field, a muon travels in a straight line. The muon track function is determined by fitting the hits in the drift chambers.

The vertex angle is determined by fitting the track near the vertex at position V_Z to the position of the first counter at the front face of the toriod. However, the large number of hits near the vertex from particles in the hadron shower limits the tracking ability. As a result, a few chambers nearest the vertex are not used for tracking. The number of drift chambers nearest the vertex position that are omitted from tracking is known as the tracking vertex offset. We then determine the muon angle from the slope of the track.

4.4 Muon Energy Reconstruction

The muon energy is reconstructed in two different regions: toroid spectrometer and target calorimeter. The track fitting in the toroid spectrometer determines the muon energy at the front face (E_μ^{FF}) of the toroid. The muon energy in the calorimeter is divided into inside the hadron shower ($PLACE$ to $SHEND - 5$) and outside the hadron shower ($SHEND - 6$ to $EXIT$) regions. $EXIT$ is the first counter downstream from $PLACE$ which is followed by three or more consecutive counters each with less than 0.3 MIPs. This analysis requires that the muon has to go through the toroid spectrometer. Outside the hadron shower (downstream of the hadron shower), the muon energy is just a sum of the scintillator pulse heights, calibrated from the muons with known energy. Inside the shower, the hadron energy overlays with the muon pulse heights.

The energy of the muon at the vertex is the muon energy measured at the front face of the toroid plus the estimated restricted energy loss inside the shower ($PSHWR$) plus

the measured energy loss outside the shower region ($PTARG$) as shown in Eq. 4.4.

$$E_\mu = E_\mu^{FF} + \sum_{place}^{shend-5} PSHWR + \sum_{shend-6}^1 PTARG, \quad (4.4)$$

where $PSHWR$ is the muon energy loss in the shower region and defined as:

$$PSHWR = \frac{dE}{dx} = 0.1668 + 0.00037E_\mu. \quad (4.5)$$

$PTARG$ is the muon energy loss in the non-shower region, and is a logarithmic function of muon energy.

$$PTARG = \frac{dE}{dx} = \begin{cases} A + B \log(E_\mu) & \text{for } E_\mu < 60, \\ A + B \log(60) + C(E_\mu - 60) & \text{for } E_\mu > 60, \end{cases} \quad (4.6)$$

where $A = 0.1419$, $B = 0.004357$, and $C = 0.00006822$.

4.5 Analysis Cuts

After the event reconstruction, the events are cut according to certain criteria to ensure good quality of data. These cuts are designed to select only the data in the regions that are well understood.

4.5.1 Fiducial Volume and Timing Cuts

The fiducial volume cuts are applied to ensure that events take place within the active regions. The timing cuts are applied to insure that events occur during the times expected for neutrino events. These cuts are:

- PLACE Cut: $20 < PLACE < 80$. This cut assures good longitudinal containment of the hadron shower in the calorimeter.
- TRANSVERSE VERTEX POSITION Cut: $|V_x| < 50$ in., and $|V_y| < 50$ in. This cut assures good transverse containment of the hadron shower in the calorimeter.
- RUN Cut: This cut eliminates bad runs for which the quality of the neutrino beam is poor or the detector is not functioned properly.
- IGATE Cut: This cut rejects events which have more than one neutrino interaction in the same detector event.
- NSTIME Cut: This cut eliminates all events detected during the non-neutrino pings of the accelerator cycle (see Section 3.4). It assures that the muon track coincides with the hadronic shower to within 36 ns.
- DIMUONS Cut: Dimuon events are events with a charm generated muon is toroid reconstructed. This cut eliminates events with a second muon track that either enters the toroid spectrometer, or penetrates more than 19 counters (imply that the second particle has energy greater than 3 GeV). These events are cut because the charged current neutrino events are determined from the higher energy muon. If the non-leading muon enters the toroid while the primary muon does not, the reconstructed kinematics will be wrong. Therefore the dimuon events have to be removed from the data and the Monte Carlo sample.

4.5.2 Geometric Cuts

The geometric cuts are applied to assure good momentum resolution in the toroid spectrometer. These cuts are:

- Trigger 1: This cut assures that muon (from the CC interaction in the target calorimeter) enters the toroid spectrometer.
- Target Track: Enough hits must be detected in the drift chambers for a muon track to be identified in the target calorimeter. The muon is required to enter the toroid and hit the first drift chamber. This is important for an accurate measurement of the muon angle.
- Toroid Containment: The muon track in the target calorimeter is extrapolated from the event vertex through the toroid, without assuming any deflection due to multiple scattering or the magnetic field. The extrapolated track must be within a circle of a radius less than 64 in. at the front face of the toroid, and must be inside a square area of 120 in. x 120 in. at the T2 counter (from -60 in. to 60 in. in x and in y directions). T2 is a counter in the second gap of toroid. This cut insures that the muon passes through the active area of toroid drift chambers.
- Toroid Track: This requires that muon enters the toroid and hits any of the last four drift chambers inside the toroid.
- Hole cut: $R_{FF} > 6$ in. This cut removes events in which the muon entered the field-free central hole of the toroid. The hole has a radius of about 6 in. The events which are reconstructed with a front face radius of less than 6 in. are removed.

- **80% Time in Steel:** The toroid consists of three sets of iron rings (washers). The washers have been cut in half and have a horizontal gap of about 2 in. We require that while the muon passed through the toroid, it spends most (80%) of its time in the steel, and not in the gap or the hole of the toroid.
- **Good Fit:** The muon tracks must be linked between the tracks in the calorimeter and in the toroid.
- **Fit Quality:** The χ^2 per degree of freedom (dof) must be less than 10. The dof is the number of chambers that the muon passed through the toroid.
- **Two Gaps:** This cut requires that muon passes through both the first and the second toroid carts to assure good reconstruction efficiency of the muon momentum. This requires a linked track segment in at least one of the two toroid gaps, for each of the x- and y-views.

4.5.3 The Cross Section Cuts

The total cross section sample is used to determine the normalization of the relative flux in this analysis. To be in the cross section sample events must satisfy the following:

- **Muon Angle Cut:** $\theta_\mu < 150$ mrad. This cut assures good acceptance of the muon track as it passes through the muon spectrometer.
- **Muon Energy Cut:** $15 < E_\mu < 600$ GeV and $E_\mu^{FF} > 3$ GeV. The low energy muons have poor reconstruction efficiency due to multiple Coulomb scattering. The high energy muons almost traverse straight through the spectrometer, resulting in poor momentum resolution.

4.5.4 Flux Cuts

NuTeV measures the relative flux with low- ν ($\nu = E_{had} < 20$ GeV) cut method. The relative flux is used to calculate the cross section and then to normalize it to the world cross section. This sample is also used for the quasi-elastic analysis. In addition to the cuts mentioned above these events must satisfy the following:

- Hadron Energy Cut: $E_{had} < 20$ GeV. The low hadron energy events are used to extract the flux in fixed- ν flux extraction.
- Neutrino Energy Cut: $15 < E_\nu < 360$ GeV. Below 15 GeV we have both a large acceptance correction and poor energy resolution. We have used the 15-30 GeV lower bin in order to correct for the smearing into the higher energy bins. The upper limit of 360 GeV is chosen because above that energy the error on the Monte Carlo smearing corrections becomes greater than 10%. The number of both neutrino and anti-neutrino events above 360 GeV is small and therefore does not make a significant impact on the analysis.

Chapter 5

Monte Carlo Simulation

The Monte Carlo program used for NuTeV data analysis is known as NUMONTE. NUMONTE is a fast Monte Carlo that first generates kinematic quantities for each event. It then smears these events by the detector resolution. Finally it reconstructs the events in a manner similar to the data analysis program. The term “*fast*” refers to the speed that events are generated. NUMONTE generates events more quickly than complete particle tracking packages like GEANT. Speed is important in this analysis. Since we would like to generate approximately two times more Monte Carlo events than 3.5 million charged current events.

Because of the limited geometry of the detector and the kinematic cuts, not all generated Monte Carlo events are fully reconstructed or pass all the cuts. The reconstructed data must be corrected for detector resolution and acceptance.

5.1 Event Generation

NUMONTE generates “*actual*” kinematic variables. They are either randomly generated or determined from the flux and the cross section distributions. The procedure of generating a charged current event by NUMONTE is as follows:

- Randomly generate a neutrino energy (E_ν^{gen}) and lateral interaction positions or so called vertex positions (V_x^{gen}, V_y^{gen}) from the flux distribution. The flux distribution is obtained from beam Monte Carlo called TURTLE. The flux energy distribution is measured in the neutral current analysis [34].
- Randomly generate a uniform distribution in *PLACE* and longitudinal vertex position (V_z^{gen}). *SHEND* is calculated using the length distribution.¹
- Randomly generate kinematics quantities: the Bjorken variable (x_{gen}), the inelasticity (y_{gen}), and the four-momentum transfer squared (q_{gen}^2) according to the cross section model.
- Calculate generated muon energy (E_μ^{gen}), the generated hadronic energy (E_{had}^{gen}), and the generated muon angle (θ_{gen}) from E_ν^{gen} , x_{gen} , and y_{gen} . Select azimuthal angle (ϕ_{gen}) uniformly between 0 and 2π .
- Simulate energy losses for muons when passing through the detector and calculates muon energy losses due to the restricted energy loss (*RESLOS*) and the catastrophic energy loss (*CATLOS*).
- Finally calculate the muon energy before entering the toroid (E_μ^{FF}) by subtracting ($RESLOS + CATLOS$) from E_μ^{gen} , and then get the position of muon at

¹Length distribution is obtained from the *PLACE* – *SHEND* distribution of NuTeV data. See more detail in Appendix A.

that point (V_x^{FF}, V_y^{FF}) .

The generated variables are then smeared to simulate detector resolution effects.

From E_ν^{gen} , x_{gen} , and y_{gen} , the variables E_{had}^{gen} , E_μ^{gen} and θ_{gen} are calculated as follows:

$$E_{had}^{gen} = y_{gen} E_\nu^{gen}, \quad (5.1)$$

$$E_\mu^{gen} = E_\nu^{gen}(1 - y_{gen}), \quad (5.2)$$

and

$$\theta_{gen} = \text{Cos}^{-1}\left(E_\mu^{gen} - M_P x_{gen} y_{gen} - \frac{m_l^2}{2E_\nu^{gen}}\right) \quad (5.3)$$

where M_P and m_l are proton and lepton masses, respectively.

5.2 Cross Section Models

NUMONTE calculates the cross section for each type of events, *e.g.* deep inelastic, quasi-elastic, and resonances, separately for proton and neutron (described in Chapter 2). Later on the cross section are added by the following relation:

$$\sigma_i = \frac{Z \times \sigma_i^{proton} + N \times \sigma_i^{neutron}}{A}, \quad (5.4)$$

where Z , N and $A = Z + N$ are the number of protons, neutrons, and nucleons, respectively. i is the type of events. The total cross section is the sum of all cross sections:

$$\sigma_{total} = \sum_i \sigma_i. \quad (5.5)$$

Then the total cross section is corrected for physics correction which are explained in the following sections.

5.3 Physics Model Corrections

The cross sections are expressed in terms of structure functions (SFs) which are functions of x , and q^2 and the physical environment of the quark. In certain cases we must calculate the cross section with different physical conditions. These different types of correction is called "*physics model corrections*" which we will described in this section.

5.3.1 Charm Mass Correction

The charm quark production can occur only in the charged current cross section. The neutrino scatters off an s- or d-quark in the nucleon and changes its flavor to a c-quark (Figure 5.1). There is no charm quark production in the neutral current interaction.

According to the Standard Model, the charged current interaction turns a lighter quark into a heavier quark with a coupling strength proportional to the Cabibbo-Kobayashi-Maskawa (CKM) matrix element. Charm (anti-charm) production from scattering off d (\bar{d}) quarks is Cabibbo suppressed by the factor $|V_{cd}|^2$ while the scattering off s (\bar{s}) quarks is Cabibbo favored by the factor $|V_{cs}|^2$. There is significant threshold effect and the Bjorken variable, x , is no longer represents the momentum fraction carried by the struck quark. Instead, the slow rescaling variable, ξ , is introduced:

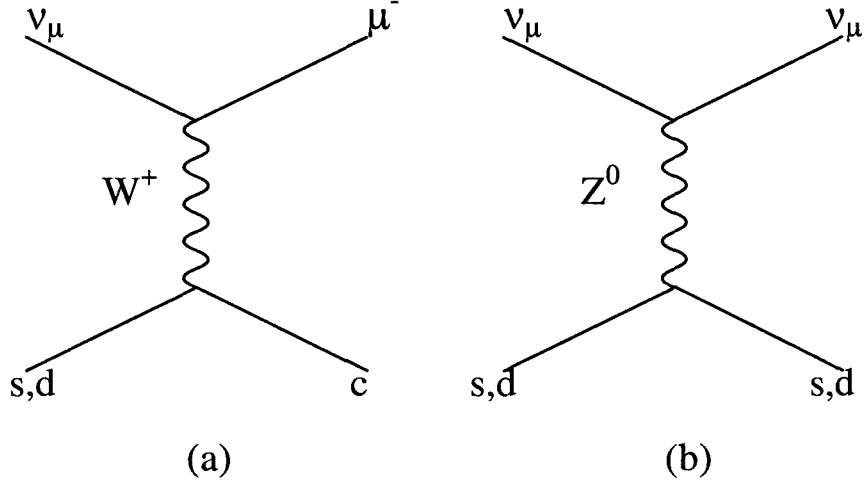


Figure 5.1: Leading order diagrams for neutrino scattering off s or d quark. (a) charged current interactions that changes the flavor of an initial quark to final state charm quark. (b) neutral current interactions that do not change the flavor of the struck quark.

$$x \rightarrow \xi = x \left(1 + \frac{m_c^2}{Q^2} \right). \quad (5.6)$$

to compensate for the charm quark threshold where m_c is the charm mass. The three structure functions are modified by the followings:

$$\begin{aligned} 2xF_1(x, Q^2) &\rightarrow \frac{x}{\xi} 2\xi F_1(\xi, Q^2) \\ F_2(x, Q^2) &\rightarrow F_2(\xi, Q^2) \\ xF_3(x, Q^2) &\rightarrow \frac{x}{\xi} \xi F_3(\xi, Q^2) \end{aligned} \quad (5.7)$$

Then the charged current differential cross section for charm production can be written in terms of the new ξ -dependent structure functions:

$$\begin{aligned} \frac{d^2\sigma^{\nu,\bar{\nu}}}{dxdy} &= \frac{G_F^2 ME}{\pi} \left[\left(1 - y - \frac{Mxy}{2E}\right) F_2^{\nu,\bar{\nu}}(\xi, Q^2) + \frac{y^2}{2} \frac{x}{\xi} 2\xi F_1^{\nu,\bar{\nu}}(\xi, Q^2) \right. \\ &\quad \left. \pm y \left(1 - \frac{y}{2}\right) \frac{x}{\xi} \xi F_3^{\nu,\bar{\nu}}(\xi, Q^2) \right] \end{aligned} \quad (5.8)$$

Writing F_2 in terms of the longitudinal structure function, R , gives a violation of the Callan-Gross relation:

$$F_2(\xi, Q^2) = \frac{1 + R(\xi, Q^2)}{1 + (2M\xi/Q)^2} 2\xi F_1(\xi, Q^2) \quad (5.9)$$

The charged current differential cross section in terms of R can be written as follows:

$$\begin{aligned} \frac{d^2\sigma^{\nu,\bar{\nu}}}{dxdy} &= \frac{G_F^2 ME}{\pi} \left[\left(\frac{y^2}{2} \frac{x}{\xi} + \frac{1 + R(\xi, Q^2)}{1 + (2M\xi/Q)^2} \left(1 - y - \frac{Mxy}{2E}\right) \right) 2\xi F_1^{\nu,\bar{\nu}}(\xi, Q^2) \right. \\ &\quad \left. \pm y \left(1 - \frac{y}{2}\right) \frac{x}{\xi} \xi F_3^{\nu,\bar{\nu}}(\xi, Q^2) \right] \end{aligned} \quad (5.10)$$

In terms of the quark distributions, the charm production charged current cross sections for neutrino and anti-neutrino are

$$\begin{aligned} \frac{d^2\sigma(\nu N \rightarrow c\mu^-)}{d\xi dy} &= \frac{G^2 ME\xi}{\pi} \left[(u(\xi, Q^2) + d(\xi, Q^2)) |V_{cd}|^2 + 2s(\xi, Q^2) |V_{cs}|^2 \right] \\ &\quad \times \left[\frac{1 + R(\xi, Q^2)}{1 + \left(\frac{2M\xi}{Q}\right)^2} \left(1 - y - \frac{Mxy}{2E}\right) + \frac{xy}{\xi} \right] \end{aligned} \quad (5.11)$$

$$\begin{aligned} \frac{d^2\sigma(\bar{\nu} N \rightarrow \bar{c}\mu^+)}{d\xi dy} &= \frac{G^2 ME\xi}{\pi} \left[(\bar{u}(\xi, Q^2) + \bar{d}(\xi, Q^2)) |V_{cd}|^2 + 2\bar{s}(\xi, Q^2) |V_{cs}|^2 \right] \\ &\quad \times \left[\frac{1 + R(\xi, Q^2)}{1 + \left(\frac{2M\xi}{Q}\right)^2} \left(1 - y - \frac{Mxy}{2E}\right) + \frac{xy}{\xi} \right] \end{aligned} \quad (5.12)$$

The charm mass term is contained in the slow rescaling term (Eq 5.6) and can be set as the charm threshold factor which is given by:

$$1 - y + \frac{xy}{\xi} = 1 - \frac{m_c^2}{2ME\xi} \quad (5.13)$$

The threshold factor must be positive, which in turns set limits on other variables:

$$x \leq 1 - \frac{m_c^2}{2MEy} \leq 1 - \frac{m_c^2}{2ME} \leq 1 \quad (5.14)$$

$$\frac{m_c^2}{2ME} \leq \frac{m_c^2}{2ME\xi} \leq y \leq 1 \quad (5.15)$$

$$\frac{m_c^2}{2ME} \leq \frac{m_c^2}{2MEy} \leq \xi \leq 1 \quad (5.16)$$

5.3.2 Isoscalar Correction

The calorimeter used in NuTeV is an iron target. Iron contains more neutrons than protons; it is not an isoscalar nucleus. The differential cross section needs to be corrected for the isoscalar target by multiplying the cross section from protons by a factor of Z/A and N/A for the cross section from neutrons. Z , N , and $A = Z + N$ are the number of protons, neutrons, and nucleons, respectively.

$$\frac{d^2\sigma^{\nu N}}{dx dy} = \frac{1}{A} \left(Z \frac{d^2\sigma^{\nu p}}{dx dy} + N \frac{d^2\sigma^{\nu n}}{dx dy} \right) \quad (5.17)$$

5.3.3 Propagator Correction

The charged current cross section includes the effect of the massive W boson propagator by multiplying the differential cross sections with the following factors:

$$\frac{d^2\sigma_{CC}^{\nu,\bar{\nu}}}{dxdy} \rightarrow \frac{d^2\sigma_{CC}^{\nu,\bar{\nu}}}{dxdy} \times \frac{1}{\left(1 + \frac{Q^2}{M_W^2}\right)^2} \quad (5.18)$$

5.3.4 Radiative Correction

The radiative corrections were calculated using the Bardin model [35]. These corrections involve the radiation of real and virtual photons from the charged lepton and quark legs in addition to $W - \gamma$ box diagrams as shown in Fig. 5.2. Instead of calculating the Bardin radiation for each event, NUMQNTTE reads in a table of Bardin radiation calculation for a range of E_ν , x , and y and applies a correction to the cross section as follows:

$$\frac{d^2\sigma}{dxdy} = \left(\frac{d^2\sigma}{dxdy} \right)_{born} \times Rad_{corr} \quad (5.19)$$

5.3.5 Nuclear Effect Correction

Nuclear effect correction is important for low q^2 region. The most important nuclear effects are the Pauli suppression and the Fermi motion. More detail on the nuclear corrections are discussed in Section 2.3.3.

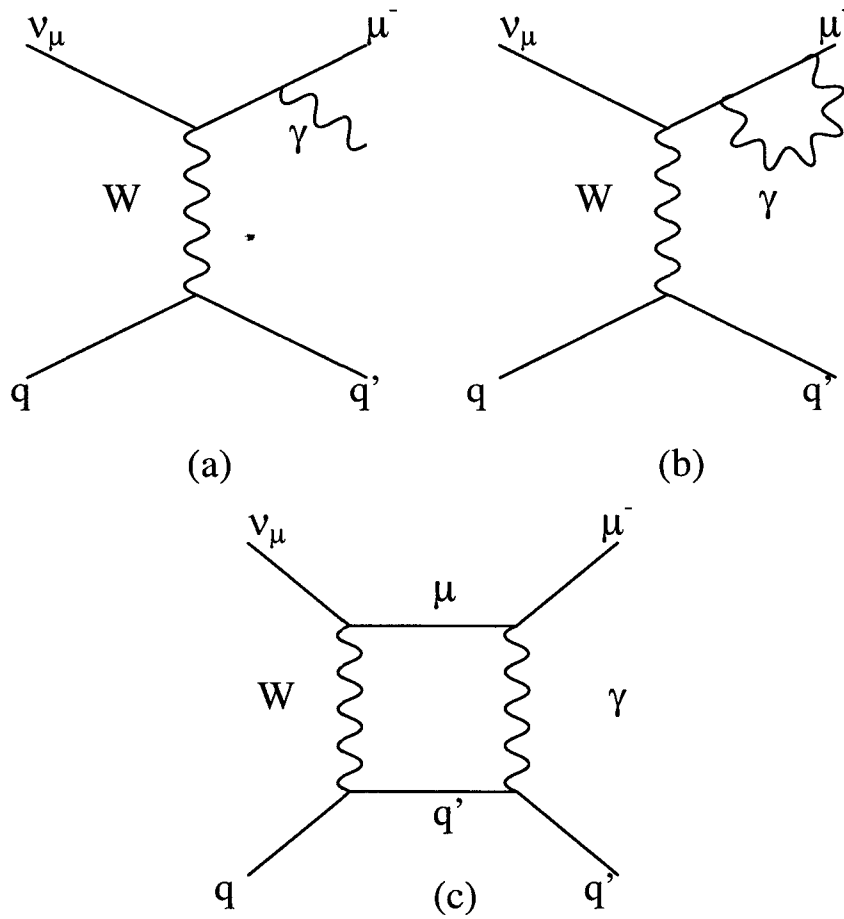


Figure 5.2: Examples of CC QED radiative correction diagrams. (a), (b) The radiative correction diagram from the muon leg. (c) The radiative correction diagram including the quark leg.

The Pauli Suppression

The Pauli suppression is applied to the cross section for deep inelastic scattering, quasi-elastic scattering, and resonances events for $W^2 < 4$.

$$\frac{d^2\sigma}{dx dy} = \left(\frac{d^2\sigma}{dx dy} \right)_{born} \times D, \quad (5.20)$$

where D is the Pauli suppression from Eq.2.61.

The Fermi Motion

The Fermi motion effect is applied to quasi-elastic and resonances events. Numonte calculates the probability of momentum distributions, $|\Phi(\vec{P})|^2$, between $0 < |\vec{P}| < 4$ (Eq.2.57) and corresponding nucleon energy after scattering as follows:

$$E_p = \begin{cases} 56 \times M_p - \sqrt{\vec{P}^2 + 55 \times M_p^2} & \text{for } 0 < |\vec{P}| < K_F \\ 2 \times M_p - \sqrt{\vec{P}^2 + M_p^2} & \text{for } K_{F^*} < |\vec{P}| < 4 \text{ GeV}/c \\ \sqrt{\vec{P}^2 + M_p^2} & \text{for } |\vec{P}| > 4 \text{ GeV}/c \end{cases} \quad (5.21)$$

5.4 E_{had} Calculation

The E_{had}^{gen} is first corrected for the nonlinearity of the NuTeV calorimeter. This nonlinearity is due to the difference in the electromagnetic shower to the hadron shower

detector responses. This gives non-unity ratio of e/h [33].

$$E_{had}^{gen} = E_{had}^{gen} \times \left[\frac{e f_{\pi^0}(E_{had}^{gen}) + h [1 - f_{\pi^0}(E_{had}^{gen})]}{e f_{\pi^0}(75) + h [1 - f_{\pi^0}(75)]} \right] \quad (5.22)$$

and $f_{\pi^0}(E_{had}^{gen})$ is normalized to 75 GeV with $e/h = 1.099$.

NUMONTE then randomly smears the E_{had}^{gen} with a continuous Poisson resolution function and obtains E_{had}^{smr} . The final hadron energy is calculated by adding the muon energy deposited in each counter (E_{μ}^{cntr}) due to *RESLOS* and *CATLOS* in the shower region to E_{had}^{smr} and subtracting the restricted muon energy loss (E_{μ}^{loss}) from that region as in Eq. 5.23. Previously we did not subtract off enough E_{μ}^{loss} . More study has been done to make this correction as described in Appendix B. Thus all of the fluctuations of the muon energy loss in the shower region appear in E_{had} .

$$E_{had} = E_{had}^{smr} + C_h \sum_{place}^{shend-5} (E_{\mu}^{cntr} - E_{\mu}^{loss}), \quad (5.23)$$

where $C_h = 0.212$ GeV/MIP is the hadron energy conversion which converts from MIP to GeV. E_{μ}^{cntr} is the muon energy deposited in the counter in MIP. E_{μ}^{loss} is defined in Eq. 4.2.

Figure 5.3 shows E_{had} distribution between data (Eq. 4.1) and MC (Eq. 5.23) for the entire analysis sample which are all events that pass the cuts described in section 4.5. The MC is normalized to data sample for E_{had} between 5 and 20 GeV. The data and MC agree well within 3% level. This normalization is then applied to all the following plots in this analysis.

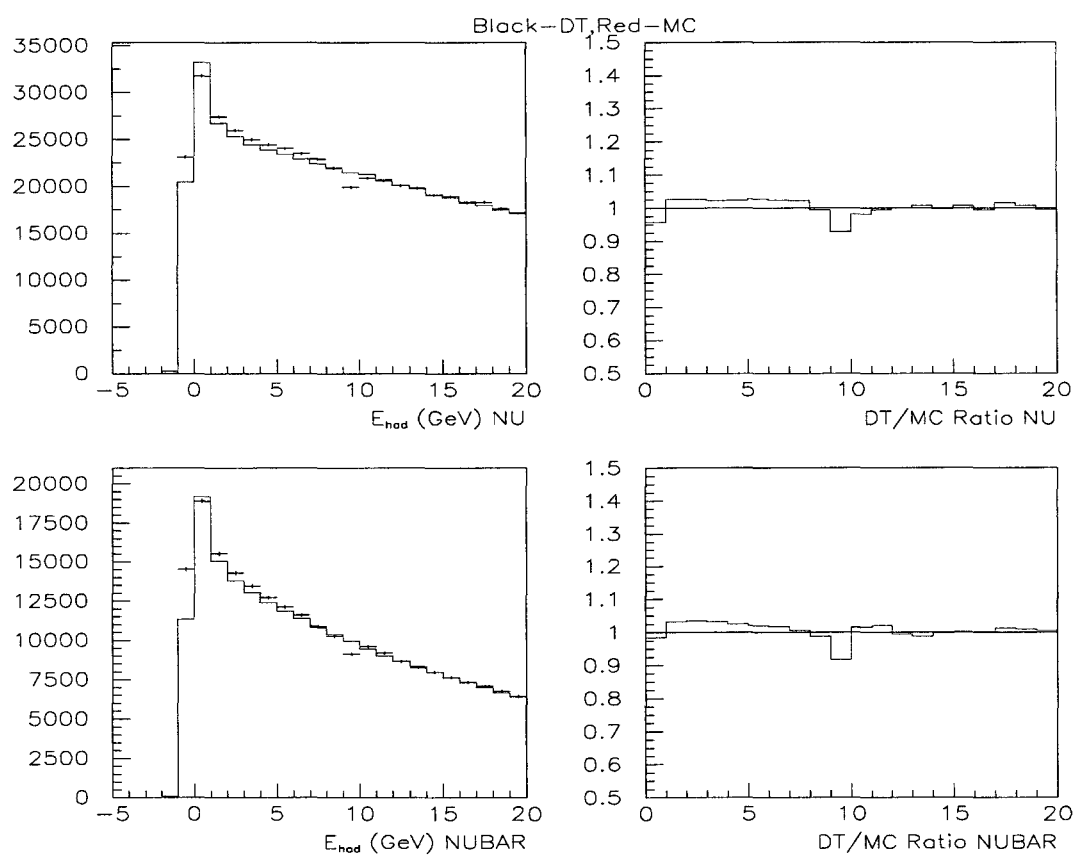


Figure 5.3: Left plots show E_{had} distribution comparison between data (black cross mark) and MC (red histogram) for both ν (top) and $\bar{\nu}$ (bottom) events. Right plots are the ratio of DT to MC for ν (top) and $\bar{\nu}$ (bottom).

5.5 E_μ Calculation

The muon energy for the charged current interaction is calculated in two different regions: toroid magnet and target calorimeter regions. The muon energy is the sum of muon energy before entering the toroid magnet (front face) and the muon energy loss in the target calorimeter. The target calorimeter regions are divided into shower and non-shower regions.

The muon energy loss is generated using measurements of the energy deposited by straight through muons (trigger 6). In this analysis we consider only the muons that reach the toroid magnet. NUMONTE first tracks the muon from PLACE to counter 1. Then it generates muon energy due to the ionization loss, bremsstrahlung, or pair production at each counter along the track, and sums over all counters to obtain the muon energy at the front face ($E_{\mu-gen}^{FF}$). The generated muon momentum at the front face ($P_{\mu-gen}^{FF}$) is calculated from

$$P_{\mu-gen}^{FF} = \sqrt{((E_{\mu-gen}^{FF})^2 - m_\mu^2)}. \quad (5.24)$$

In the toroid magnet, $P_{\mu-gen}^{FF}$ is smeared by the momentum resolution function of the toroid magnet and gets $P_{\mu-smr}^{FF}$. $E_{\mu-smr}^{FF}$ is then calculated from $P_{\mu-smr}^{FF}$.

In the shower region, the muon momentum loss (dE/dx) is assumed to be linearly dependent of muon energy ($PSHWR$). $PSHWR$ is defined the same as the one for the data in Eq. 4.5. In the non-shower region, (dE/dx) is a logarithmic function of muon energy ($PTARG$). $PTARG$ is defined as shown in Eq. 4.6.

Finally the momentum and the energy of muon can be calculated from:

$$P_\mu = P_\mu^{FF} + \sum_{place}^{shend-5} PSHWR + \sum_{shend-6}^1 PTARG, \quad (5.25)$$

and

$$E_\mu = \sqrt{(P_\mu^2 + m_\mu^2)}. \quad (5.26)$$

Figure 5.4 shows E_μ distribution between data (Eq. 4.4) and MC (Eq. 5.26) for the entire analysis sample. The plots show good agreement between data and MC for $20 < E_\mu < 250$.

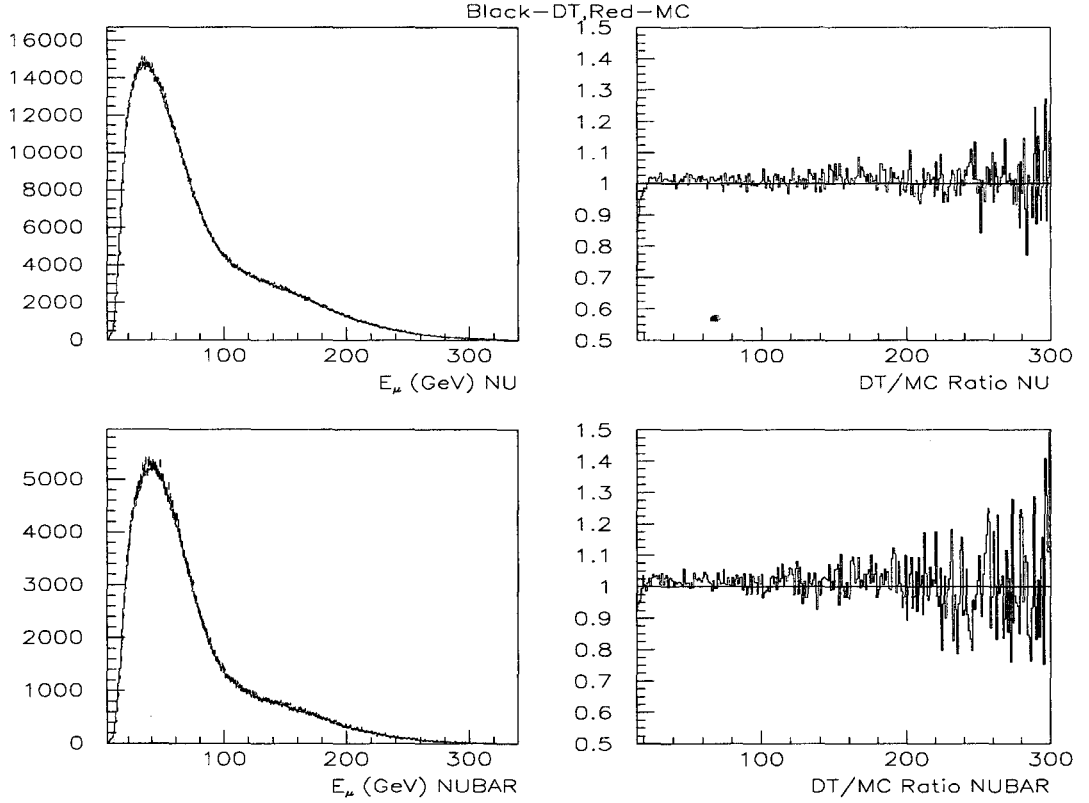


Figure 5.4: Left plots show E_μ distribution comparison between data (black cross mark) and MC (red histogram) for both ν (top) and $\bar{\nu}$ (bottom) events. Right plots are the ratio of DT to MC for ν (top) and $\bar{\nu}$ (bottom).

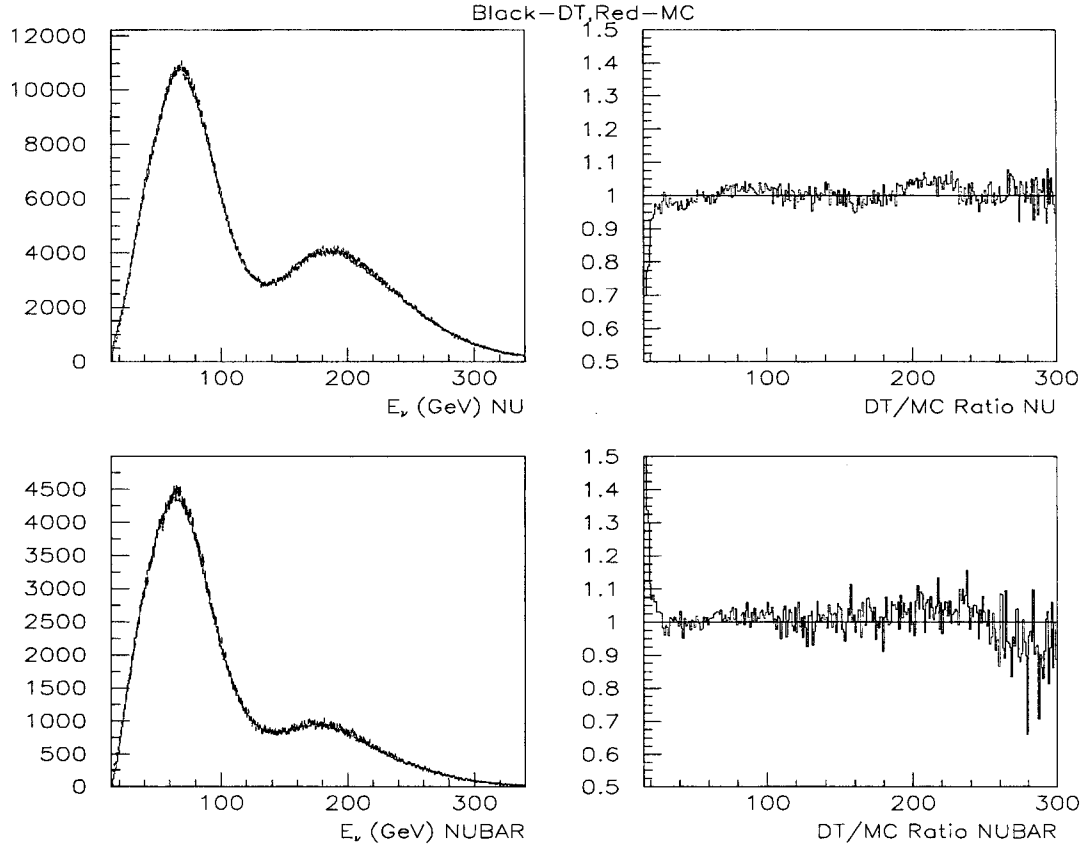


Figure 5.5: Left plots show E_ν distribution comparison between data (black cross mark) and MC (red histogram) for both ν (top) and $\bar{\nu}$ (bottom) events. Right plots are the ratio of DT to MC for ν (top) and $\bar{\nu}$ (bottom).

5.6 Calculation of Other Variables

After reconstructing E_{had} and E_μ , E_ν is calculated as a sum of those energies ($E_\nu = E_{had} + E_\mu$). Figure 5.5 shows E_ν distribution between data and MC for the entire analysis sample. The plots show good agreement between data and MC for $25 < E_\nu < 250$.

The muon angle is reconstructed using the muon trajectory throughout the target calorimeter. Figure 5.6 shows θ_μ distribution between data and MC for the entire analysis sample. The plots show good agreement between the data and MC.

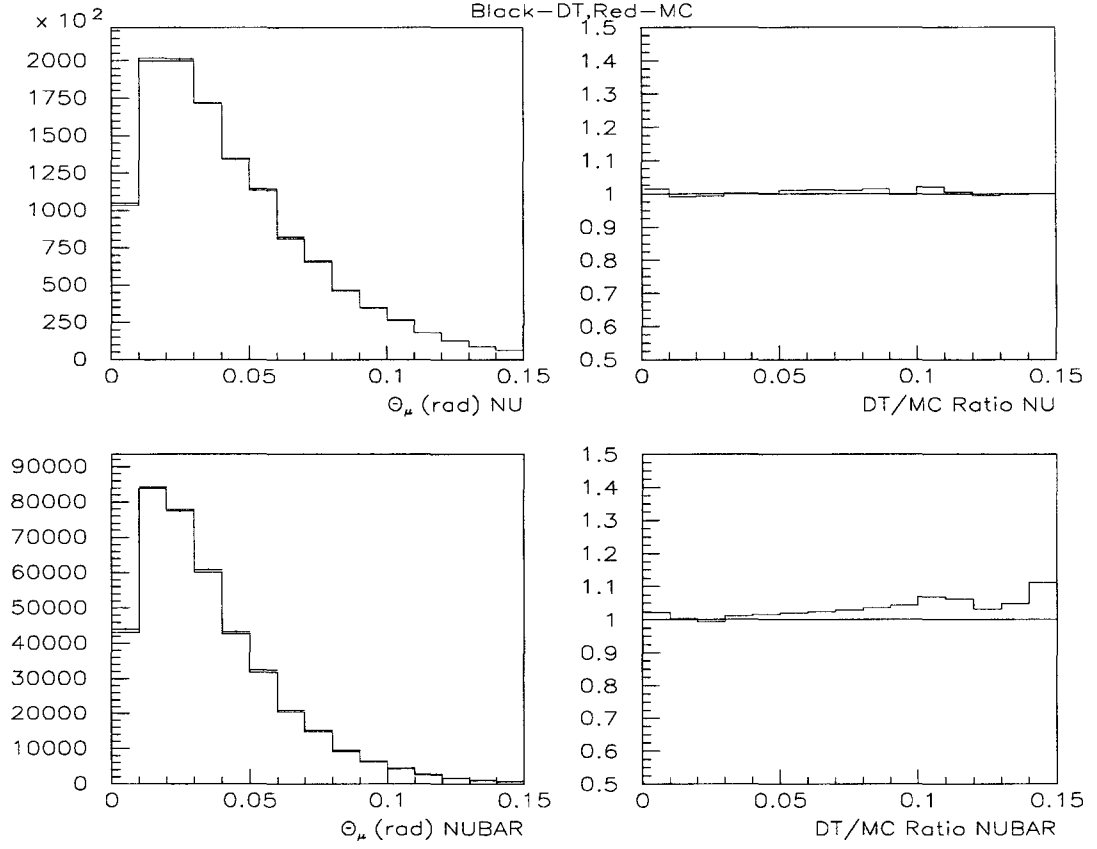


Figure 5.6: Left plots show θ_μ distribution comparison between data (black cross mark) and MC (red histogram) for both ν (top) and $\bar{\nu}$ (bottom) events. Right plots are the ratio of DT to MC for ν (top) and $\bar{\nu}$ (bottom).

The four-momentum transfer defined as $q^2 = 2E_\nu E_\mu - 2E_\mu P_\mu \cos \theta_\mu - m_\mu^2$ is then calculated and compare to data in two different E_{had} ranges, $E_{had} < 5$ and $5 < E_{had} < 20$.

The plots are shown in fig. 5.7 - 5.8.

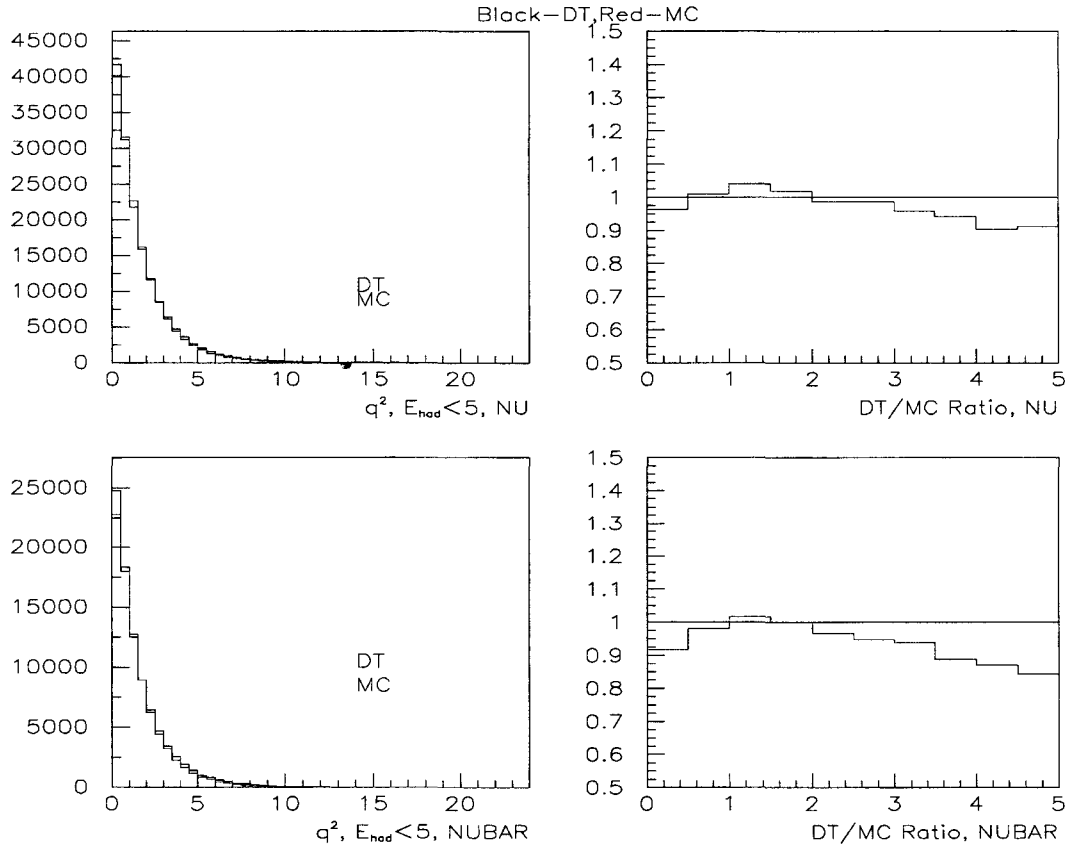


Figure 5.7: Left plots show q^2 distribution comparison between data (black cross mark) and MC (red histogram) in ν (top) and $\bar{\nu}$ (bottom) modes for $E_{had} < 5$. Right plots are the ratio of DT to MC for ν (top) and $\bar{\nu}$ (bottom).

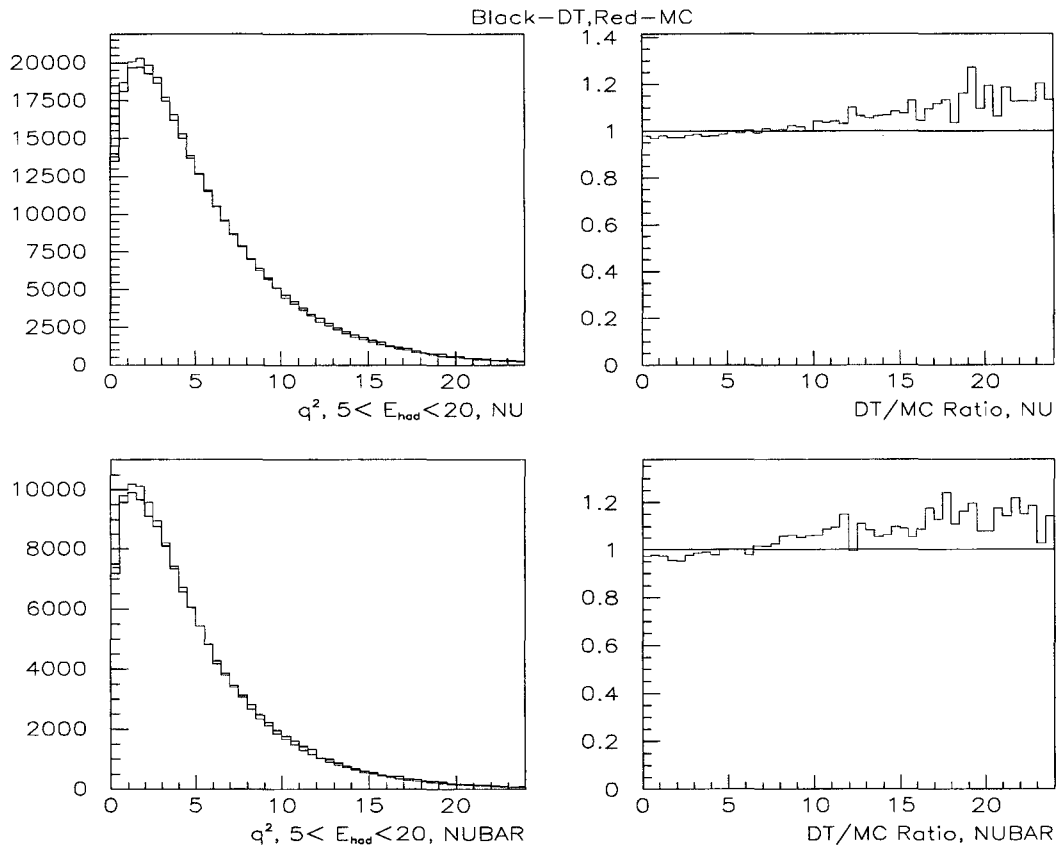


Figure 5.8: Left plots show q^2 distribution comparison between data (black cross mark) and MC (red histogram) in ν (top) and $\bar{\nu}$ (bottom) modes for $5 < E_{had} < 20$. Right plots are the ratio of DT to MC for ν (top) and $\bar{\nu}$ (bottom).

Chapter 6

The Extraction of Flux and Quasi-Elastic Cross Sections

In previous chapters, we have described how we collected the data and how we modeled it with our Monte Carlo. This chapter we will describe how the flux and the quasi-elastic (QE) cross sections are extracted.

In general the cross section (σ) is proportional to the ratio of a number of events (N) to the flux (Φ), $\sigma \propto \frac{N}{\Phi}$. In our analysis N is the number of QE events, and the flux is a number of neutrinos that passed through a unit area.

NuTeV does not provide a direct measurement of either the flux (absolute flux) or the QE events. Instead of using the absolute flux, we determine the “*relative*” flux from a sub-class of the charged current (CC) deep inelastic scattering (DIS) events. We then use this flux and CC DIS events to get the CC DIS cross section (σ_{cc}). Later we normalize the ν type of CC DIS cross section (σ_{cc}^ν) to the world CC DIS cross

section ($\sigma_{cc}^{\nu, world}$). This normalization factor will be used to determine $\bar{\nu}$ type of CC DIS cross section. We then apply the same normalization to the relative flux and get the absolute flux.

The number of QE events is extracted from the NuTeV data in a low hadronic energy region. This sample is independent of the flux sample. Once we know the flux (Φ) and the number of QE (N_{qe}) events, the cross section can be calculated. The extraction methods will be discussed in more detail in this chapter.

6.1 Flux

At high momentum transfer, the inelastic scattering process is much more probable than elastic scattering process. By plotting the four-momentum transfer squared, Q^2 , against $2M\nu$, as shown in Fig. 6.1, the phase space or area under the line $x = 1$ represents the physical region. The region $x < 1$ corresponds to the inelastic scattering, while the line $x = 1$ defines the kinematics for elastic scattering.

Consider the inelastic region, the phase space or area under $x = 1$ line is proportional to the value of ν . The maximum value of ν is E ($\nu_{max} = E$) when the outgoing lepton carries zero momentum. The phase space of ν_{max} is now a function of E and increases with E . Because the cross section is proportional to the phase space, this implies that the cross section is also proportional to E .

In CC total cross section, we integrate ν from 0 to ν_{max} , and get $\sigma^{total} \propto E$. So

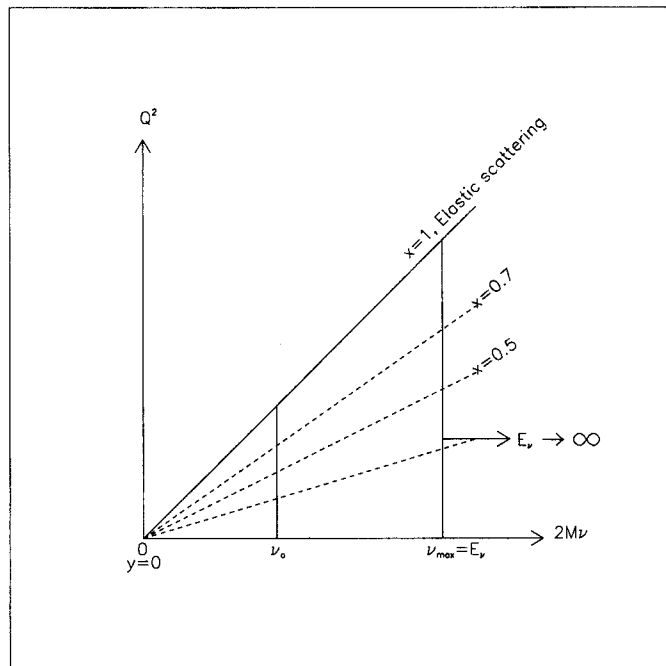


Figure 6.1: The kinematic region for ν -N scattering processes.

the CC total cross section rises linearly with E . While in the fixed- ν flux extraction method, we do the integration of ν from 0 to ν_o where ν_o is a constant and set to be 20 GeV. This makes the fixed- ν flux cross section constant, $\sigma^{fixed-\nu} \propto \nu_o = constant$. Because the cross section is constant, the flux is proportional to the total number of scattering events below a fixed ν_o .

6.1.1 Fixed ν Flux Extraction Method

In NuTeV experiment it is difficult to measure the absolute flux. The fixed- ν flux extraction method is introduced to measure the relative flux. This method relies on CC events with low ν . The scaling variable term $x = \frac{Q^2}{2M\nu}$ limits the Q^2 and $2M\nu$ relation and also set the limit of the cross section as described previously.

The differential cross section for DIS process in Eq. 2.23 can be rewritten in terms of x , ν and E as follows:

$$\frac{d^2\sigma^{\nu(\bar{\nu})}}{dx d\nu} = \frac{G_F^2 M}{\pi} \left[\left(1 - \frac{\nu}{E} - \frac{Mx\nu}{2E^2} + \frac{\nu^2}{2E^2} \frac{1 + \frac{2Mx}{\nu}}{1 + R} \right) F_2^{\nu(\bar{\nu})} \pm \frac{\nu}{E} \left(1 - \frac{\nu}{2E} \right) x F_3^{\nu(\bar{\nu})} \right]. \quad (6.1)$$

Rewriting Eq. 6.1 in terms of powers of $\frac{\nu}{E}$ term gives:

$$\frac{d^2\sigma^{\nu(\bar{\nu})}}{dx d\nu} = \frac{G_F^2 M}{\pi} \left[F_2 - \frac{\nu}{E} (F_2 \mp x F_3) + \frac{\nu^2}{2E^2} \left(\left(\frac{1 + 2Mx/\nu}{1 + R} - \frac{Mx}{\nu} \right) F_2 \mp x F_3 \right) \right]. \quad (6.2)$$

If we define $\tilde{R}(x, Q^2)$ such that

$$1 + \tilde{R} = \frac{1 + 2Mx/\nu}{1 + R} - \frac{Mx}{\nu} \quad (6.3)$$

then Eq. 6.2 takes a simple form:

$$\frac{d^2\sigma^{\nu(\bar{\nu})}}{dx d\nu} = \frac{G_F^2 M}{\pi} \left[F_2 - \frac{\nu}{E} (F_2 \mp x F_3) + \frac{\nu^2}{2E^2} (F_2 \mp x F_3 + \tilde{R} F_2) \right]. \quad (6.4)$$

Like R , \tilde{R} can be determined from DIS electron scattering.

Integrating Eq. 6.4 over all x with ν and E fixed yields:

$$\frac{d\sigma^{\nu(\bar{\nu})}}{d\nu} = \frac{G_F^2 M}{\pi} \left[\int F_2 - \frac{\nu}{E} \left(\int F_2 \mp \int x F_3 \right) + \frac{\nu^2}{2E^2} \left(\int F_2 \mp \int x F_3 + \int \tilde{R} F_2 \right) \right], \quad (6.5)$$

where $\int F = \int_0^1 F(x) dx$ for F_2 and $x F_3$. According to the quark parton model, F_2 and $x F_3$ are now functions of x only and therefore their integrals are constant.

Rewriting in term of constants A , B , and C

$$\begin{aligned}\frac{d\sigma^{\nu(\bar{\nu})}}{d\nu} &= A + \frac{\nu}{E}B - \frac{\nu^2}{2E^2}(B - A\tilde{R}), \\ &= A + \frac{\nu}{E}B - \frac{\nu^2}{2E^2}C,\end{aligned}\tag{6.6}$$

where

$$\begin{aligned}A &= \frac{G_F^2 M}{\pi} \int F_2, \\ B &= -\frac{G_F^2 M}{\pi} \int (F_2 \mp x F_3), \\ C &= B - \frac{G_F^2 M}{\pi} \int \tilde{R} F_2, \\ \frac{B}{A} &= -\left(1 \mp \frac{\int x F_3}{\int F_2}\right).\end{aligned}\tag{6.7}$$

We then integrate over a region of ν to get the total cross section.

$$\sigma^{\nu,\bar{\nu}} = \nu \left[A + \frac{\nu}{2E}B - \frac{\nu^2}{6E^2}C \right].\tag{6.8}$$

In the limit that $\frac{\nu}{E}$ is small, Eq. 6.8 shows that the total cross section depends only on the value of ν . If ν is constant then the total cross section is also a constant and the number of events we observe is proportional to the flux. If ν is set to be $\nu_{max} = E$ then the total cross section will depend on E as well. This agrees with the result from the previous section.

We multiply both side of Eq. 6.6 with a flux and get the number of events:

$$\frac{dN(E, \nu)}{d\nu} \propto \Phi(E) \left[A + \frac{\nu}{E} B - \frac{\nu^2}{2E^2} (B - A\tilde{R}) \right]. \quad (6.9)$$

$\frac{dN(E, \nu)}{d\nu}$ is the number of observed CC events which can be determined by binning events in (E, ν) . $\Phi(E)$ is the incident neutrino flux and defined as the number of neutrino per unit area. We can also write the flux from Eq. 6.9 as:

$$\Phi(E) \propto \int_0^{\nu_o} \frac{\frac{dN(E, \nu)}{d\nu}}{\left[1 + \frac{\nu}{E} \frac{B}{A} - \frac{\nu^2}{2E^2} \left(\frac{B}{A} - \frac{\int \tilde{R} F_2}{\int F_2} \right) \right]} d\nu \equiv \int_0^{\nu_o} \frac{dN(E, \nu)^{corr}}{d\nu} d\nu. \quad (6.10)$$

The denominator term is called $\frac{B}{A}$ -correction and the term $\frac{B}{A}$ is energy independent. $\frac{dN(E, \nu)^{corr}}{d\nu}$ has been corrected for the $\frac{B}{A}$ -correction in each energy bin. We fit Eq. 6.9 as a quadratic function of $\frac{\nu}{E}$ for $\nu < \nu_o$ to extract $\frac{B}{A}$ for each E bin. Then we average the $\frac{B}{A}$ over E bin and use it to get $\frac{dN(E, \nu)^{corr}}{d\nu}$ and $\Phi(E) \propto N(E)^{corr} = \int_0^{\nu_o} \frac{dN(E, \nu)^{corr}}{d\nu} d\nu$.

6.1.2 Flux Extraction

In the flux extraction, all events have to pass the fiducial volume, geometric and flux cuts. The events are futher divided into $E_{had}(\equiv \nu)$ bins which is 1 GeV wide for a total of 25 bins from -5 to $\nu_o = 20$ GeV. The negative E_{had} is possible and comes from both pedestal fluctuations and fluctuation in the subtraction of the energy deposited by the muon. We first correct the number of data events (DT) for the acceptance

and the physics model corrections which is described in Section 5.3 as follows:

$$\begin{aligned}
 DT^{corrected} = & DT^{reconstructed} \times \frac{MC^{smr}}{\underbrace{MC^{gen}}_{AcceptanceCorrection}} \\
 & \times \underbrace{\frac{\sigma(m_c = 0, IsoscalarTarget, noProp.Corr., noRad.Corr.)}{\sigma(m_c = 1.32, FeTarget, Prop.Corr., Rad.Corr.)}}_{PhysicsModelCorrection}
 \end{aligned} \tag{6.11}$$

The first term on the right hand side is the reconstructed data events. The second term is the acceptance correction where MC^{smr} and MC^{gen} are smeared and generated Monte Carlo (MC) events, respectively. The last term is the physics model correction discussed in Section 5.3 and meant to bring the cross section to the parton model assumptions. The σ term in the numerator is the CC DIS cross section without a charm threshold in the final state on an isoscalar target, with no q^2 dependence in the boson propagator and without the radiative corrections. The σ term in the denominator is the physical CC DIS cross section with a charm threshold in the final state on an iron target, with the real boson propagator and with the radiative corrections. We apply the physics model corrections to the data because the $\frac{B}{A}$ term should be extracted in the bare level without any corrections.

Instead of writing as $\frac{dN(E,\nu)}{d\nu}$ as done in the previous section we use $\Delta N(E, \nu)$ because the number of events are binned in E and ν bins. The value of $\frac{B}{A}$ in each E bin is determined from a fit to the corrected number of events ($\Delta N(E, \nu) \equiv DT^{corrected}$) distribution in ν bins from Eq. 6.9. $\Delta N(E, \nu)$ is fitted to the following relation:

$$\Delta N(E, \nu) = \left[A' \left(1 + \frac{\nu^2}{2E^2} \tilde{R} \right) + B' \left(\frac{\nu}{E} - \frac{\nu^2}{2E^2} \right) \right]. \tag{6.12}$$

Equation 6.12 has only two unknown, A' and B' . The ratio of $\frac{B'}{A'}$ is the same as $\frac{B}{A}$. We will use $\frac{B}{A}$ instead of $\frac{B'}{A'}$. The $\tilde{R} \equiv \frac{\int \tilde{R} F_2}{\int F_2}$ is calculated using the Buras-Gaemers differential cross section model. F_2 is just a sum of quark and anti-quark distribution. Hence, we can extract the value of A' and B' and get the ratio of $\frac{B}{A}$ in each individual energy bin. The ratio $\frac{B}{A}$ is constant within each energy bin. We do not include the low $E_{had}(\nu)$ in the flux samples. Therefore $\Delta N(E, \nu)$ is only fit from $\nu_{min} = 5 < \nu < \nu_o = 20$ GeV. This low E_{had} cut removes the QE and resonances (RES) processes. The extracted values of $\frac{B}{A}$ do not show any strong energy dependence, as shown in Fig. 6.2. So we fit $\frac{B}{A}$ in each individual energy bin and compute the average $\langle \frac{B}{A} \rangle$ over the different energy bins for $30 < E < 360$ GeV. The average can be taken if the $\int F$ term is a constant between different energy bins. The average $\langle \frac{B}{A} \rangle$ for ν and $\bar{\nu}$ are -0.6168 ± 0.0329 and -1.8090 ± 0.0257 , respectively.

Instead of using \tilde{R} from electron scattering data, we have tried to extract it from our neutrino data. This is an alternative way to extract \tilde{R} . We rewrite Eq. 6.12 as follows:

$$\Delta N(E, \nu) = A' + \left(\frac{\nu}{E} - \frac{\nu^2}{2E^2} \right) B' + \frac{\nu^2}{2E^2} A' \tilde{R}, \quad (6.13)$$

and

$$\Delta N(E, \nu) = A' + \left(\frac{\nu}{E} - \frac{\nu^2}{2E^2} \right) B' + \frac{\nu^2}{2E^2} C'. \quad (6.14)$$

We now fit three parameters, A' , B' and C' . The parameter C' is related to \tilde{R} as:

$$\tilde{R}' = \frac{C'}{A'} \quad (6.15)$$

The fit values of \tilde{R}' are listed in table 6.1. The errors of \tilde{R}' are very large. Most

of the values of \tilde{R}' are within one sigma from \tilde{R} . Thus, we are consistent with the electro-production data and we decided to use the \tilde{R} from it.

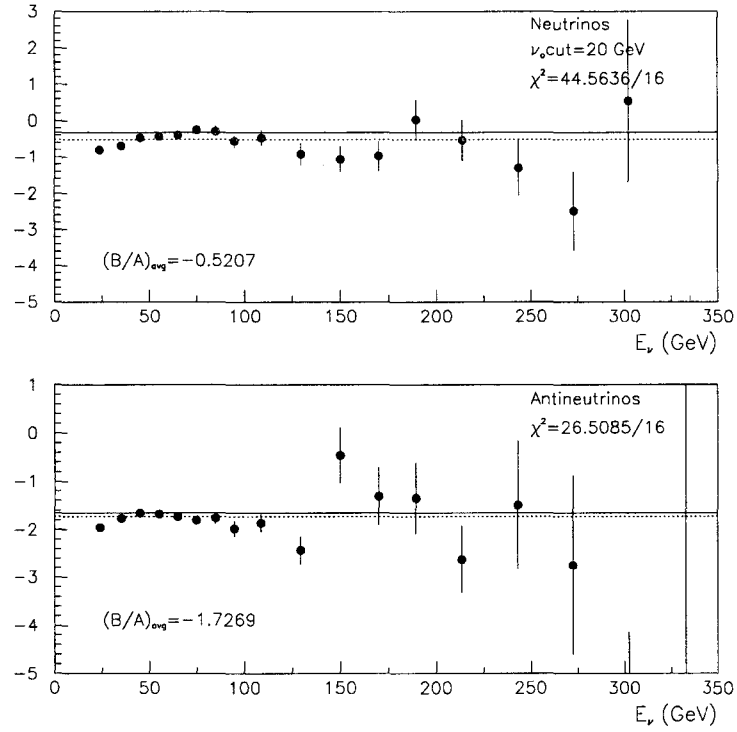


Figure 6.2: $\frac{B}{A}$ as a function of E_ν for ν (top) and $\bar{\nu}$ (bottom) modes. The solid line is CCFR [36] $\frac{B}{A}$ average. The dash line is NuTeV $\frac{B}{A}$ average. The points are individual NuTeV $\frac{B}{A}$.

6.1.3 Flux Normalization

After we get the $\frac{B}{A}$ term, the flux which is proportional to $N(E)^{\text{corr}}$ can be calculated from Eq. 6.10. Because the flux does not depend on the type of events, we include all events between 5 and 20 ($5 < \nu < 20$) GeV.

Neutrino energy	\tilde{R}	$\tilde{R}' \pm error \nu mode$	$\tilde{R}' \pm error \bar{\nu} mode$
$15 < E_\nu < 30$	-0.7326	-2 ± 2	0.5 ± 0.8
$30 < E_\nu < 40$	-0.2093	-0.5 ± 0.6	-0.1 ± 0.5
$40 < E_\nu < 50$	-0.1617	-0.8 ± 1.0	-0.2 ± 0.8
$50 < E_\nu < 60$	-0.1582	-1 ± 1	0 ± 1
$60 < E_\nu < 70$	-0.1550	2 ± 2	0 ± 2
$70 < E_\nu < 80$	-0.1513	-1 ± 3	-8 ± 4
$80 < E_\nu < 90$	-0.1478	0 ± 5	-2 ± 5
$90 < E_\nu < 100$	-0.1442	-13 ± 9	-2 ± 8
$100 < E_\nu < 120$	-0.1410	-10 ± 10	10 ± 9
$120 < E_\nu < 140$	-0.1379	9 ± 16	-22 ± 24
$140 < E_\nu < 160$	-0.1352	-17 ± 30	30 ± 29
$160 < E_\nu < 180$	-0.1325	-3 ± 31	26 ± 42
$180 < E_\nu < 200$	-0.1302	-16 ± 51	95 ± 41
$200 < E_\nu < 230$	-0.1280	31 ± 49	34 ± 69
$230 < E_\nu < 260$	-0.1259	7 ± 85	80 ± 130
$260 < E_\nu < 290$	-0.1240	-130 ± 190	-250 ± 380
$290 < E_\nu < 320$	-0.1222	490 ± 130	140 ± 340
$320 < E_\nu < 360$	-0.1205	320 ± 240	880 ± 210

Table 6.1: Comparison of \tilde{R} and \tilde{R}' in ν and $\bar{\nu}$ modes.

We have calculated the relative flux in the previous section. The relative flux is proportional to the corrected number of events for $5 < \nu < \nu_o = 20$ GeV as shown in Eq. 6.10. We need an absolute flux to calculate the cross section. The absolute normalization factor of the flux is obtained by normalizing our CC DIS neutrino-nucleon ($\nu - N$) cross section to the average of the world CC DIS $\nu - N$ cross section for an isoscalar target. Our average cross section, using the relative flux in the $15 < E < 300$ GeV range, is normalized to the world average isoscalar CC DIS $\nu - N$ cross section of $\frac{\sigma^\nu}{E} = 0.677 \times 10^{-38} \text{cm}^2/\text{GeV}$ per nucleon [36].

The absolute flux is calculated from

$$\begin{aligned} \Phi(E) = & \sum_{5 < \nu \leq 20} \Delta N^{corr}(E, \nu) \times \left\langle \frac{1}{\sigma_{cc}^{\nu, world, iso}(E)/E} \right\rangle \\ & \times \left\langle \frac{\sum_{all \nu} \Delta N^{Acc.Corr.}(E, \nu)}{\sum_{5 < \nu \leq 20} \Delta N^{corr}(E, \nu) \times \langle E \rangle} \times \frac{\sigma^{model, iso}}{\sigma^{model, Fe}} \right\rangle. \end{aligned} \quad (6.16)$$

The first term on the right hand side is the corrected number of events which have been corrected for acceptance, physics model and $\frac{B}{A}$ -corrections. The second term is the inverse of the average of the world isoscalar CC DIS $\nu - N$ cross section per unit energy. The last term is the average of the corrected cross section per unit energy. $\Delta N^{Acc.Corr.}(E, \nu)$ is the number of events corrected only for acceptance correction. $\langle E \rangle$ is the average energy for each bin. $\sigma^{model, iso}$ is the CC DIS cross section that is corrected for isoscalar target and has had applied the charm mass, W-propagator, and radiative corrections. $\sigma^{model, Fe}$ is the CC DIS cross section that is corrected for all physics correction but not for an isoscalar target correction. We apply these physics corrections back to the data because we use the world CC DIS isoscalar cross section as a normalization factor.

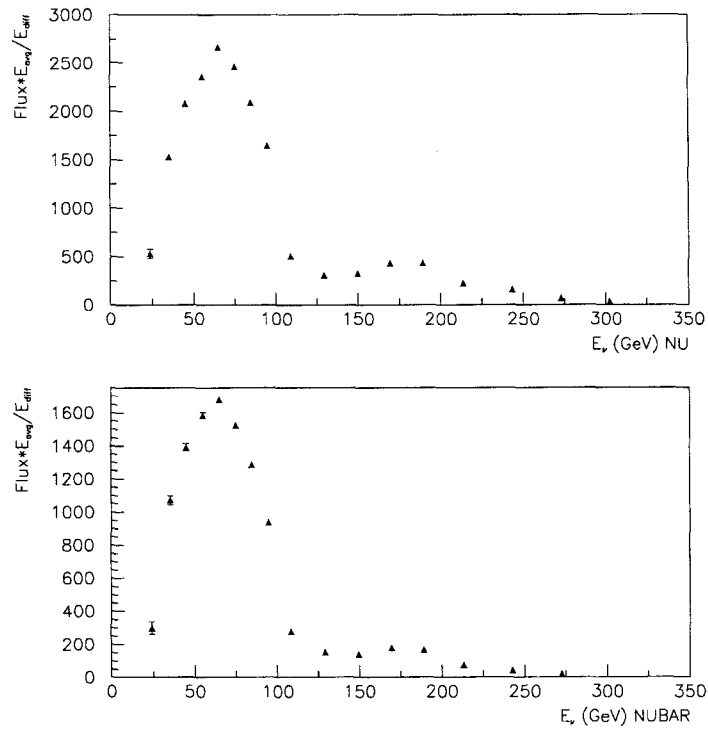


Figure 6.3: The absolute flux distribution in ν (top) and $\bar{\nu}$ (bottom) modes. The error bar shows only statistical error.

Figure 6.3 shows the absolute flux using the described extraction method. Because the size of each energy bin is different we plot $\frac{\Phi(E) \times E_{avg}}{E_{diff}}$. E_{avg} is the average energy for each energy bin. E_{diff} is the bin size for each energy bin.

6.2 QE Events Extraction

The QE scattering process occurs in the low q^2 , low E_{had} and high x region. There is a peak at small E_{had} which indicates the QE events as shown in Fig. 6.4. It is difficult to measure only QE events from our data because NuTeV experiment was not designed to measure the DIS, QE and RES events separately. Instead NuTeV data contain all possible processes. We have to use Monte Carlo to model each type of event and eliminate those unwanted events until we get only QE events. Looking at the E_{had} distribution, we can see that there is a peak in the data at low E_{had} which is the QE events.

6.2.1 Non DIS Events Extraction

Figure 6.5 compares the E_{had} distribution for the data ¹ and Monte Carlo. The NuTeV data (DT) shows a peak at low E_{had} which is consistent with the peak in Fig. 6.4. The Monte Carlo which in this version models only DIS (MC_{DIS}) process. DT and MC_{DIS} agree very well in $5 < E_{had} < 20$ GeV ($E_{had} > 5$) region. This is the region used to extract the flux. The MC_{DIS} events are normalized to DT events with the following normalization (N_1):

$$N_1 = \frac{DT}{MC_{DIS}} \Big|_{5 < E_{had} < 20} \quad (6.17)$$

Since DT and MC_{DIS} agree above 5 GeV we assume that the normalized MC_{DIS} accurately predicts the DIS type of events below 5 GeV. We then extract events

¹There is a dip in the data at $E_{had} \approx 10$ GeV in both modes. This may come from the bad measurement during certain period of time and we ignore it in this study.

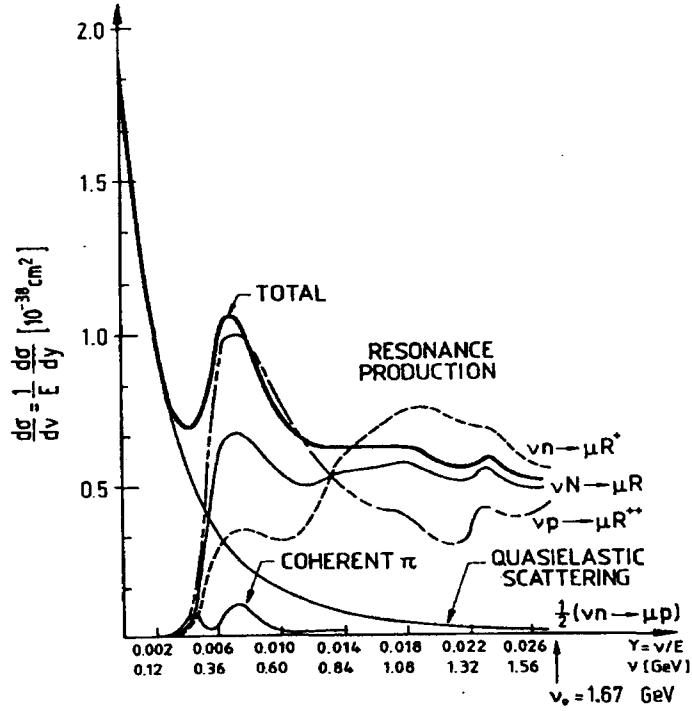


Figure 6.4: The differential cross section in low E_{had}^* for $E_\nu = 60$ GeV. This plot is Fig.5 in Ref. [37]. It shows that the quasi-elastic cross section dominates in low E_{had} region.

which are not DIS (NON-DIS events) by subtracting normalized MC_{DIS} events from DT events ($DT - N_1 \times MC_{DIS}$). These NON-DIS events include QE and RES events.

The number of NON-DIS events are summed from $-5 < E_{had} < 5$ GeV. This region ($E_{had} < 5$) is independent of the flux sample. These events as a function of E_ν are shown in Fig. 6.6. The number of events in each energy bin is listed in Table 6.2.

We estimate the number of RES events in the NON-DIS samples by using higher

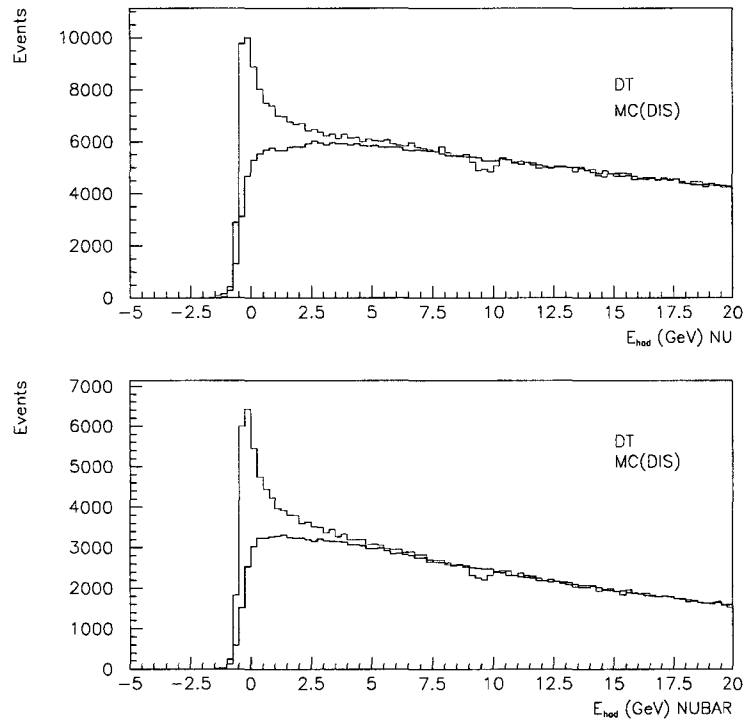


Figure 6.5: The E_{had} distribution between DT (red histogram with a peak) and MC_{DIS} (blue histogram drop to zero) in ν (top) and $\bar{\nu}$ (bottom) modes.

Neutrino energy	event $\pm\delta$ ν mode	event $\pm\delta$ $\bar{\nu}$ mode
$15 < E_\nu < 30$	3552 ± 218	3211 ± 217
$30 < E_\nu < 40$	4074 ± 226	2800 ± 239
$40 < E_\nu < 50$	3721 ± 234	2623 ± 247
$50 < E_\nu < 60$	3689 ± 229	2501 ± 242
$60 < E_\nu < 70$	3289 ± 219	2337 ± 227
$70 < E_\nu < 80$	2863 ± 196	1746 ± 203
$80 < E_\nu < 90$	2115 ± 168	1391 ± 171
$90 < E_\nu < 100$	1367 ± 139	908 ± 139
$100 < E_\nu < 120$	1736 ± 149	1064 ± 146
$120 < E_\nu < 140$	1226 ± 113	526 ± 105
$140 < E_\nu < 160$	770 ± 105	442 ± 93
$160 < E_\nu < 180$	1026 ± 106	343 ± 89
$180 < E_\nu < 200$	849 ± 99	414 ± 81
$200 < E_\nu < 230$	1028 ± 103	365 ± 80
$230 < E_\nu < 260$	500 ± 79	206 ± 58
$260 < E_\nu < 290$	249 ± 56	79 ± 40
$290 < E_\nu < 320$	161 ± 38	41 ± 26
$320 < E_\nu < 360$	77 ± 27	22 ± 17

Table 6.2: The number of NON-DIS events in ν and $\bar{\nu}$ modes.

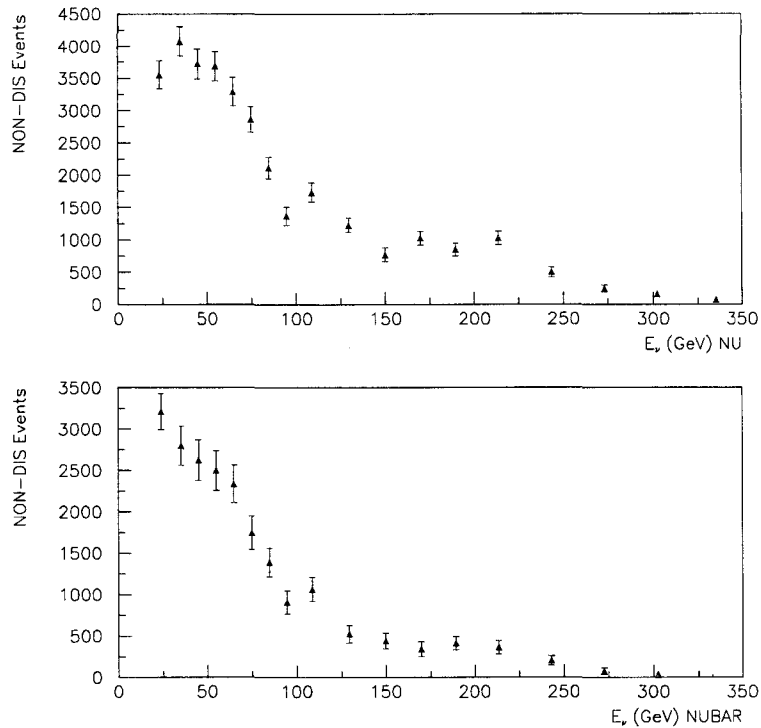


Figure 6.6: The NON-DIS sample as a function of E_ν in ν (top) and $\bar{\nu}$ (bottom) modes. The error bars show only statistical errors.

twist (HT) model. The HT model (described in Section. 2.5) should account for the average of the low energy resonance production. Our hadron energy resolution is insufficient to distinguish individual resonances peaks. HT model which averages the resonances production would be appropriate for us. To implement this model we reweight each DIS event with the HT factor described in Eq. 2.72 in Section 2.5.3. HT events are the differences between MC which models both DIS and HT (MC_{DIS+HT}) and MC with only DIS (MC_{DIS}). These two MC events are normalized to DT events for $E_{had} > 5$ GeV region. Figure 6.7 and Table 6.3 show the HT events as a function of E_ν .

The events left over from the subtraction of HT from NON-DIS samples are QE events. Figure 6.8 and Table 6.4 show QE events distribution as a function of energy.

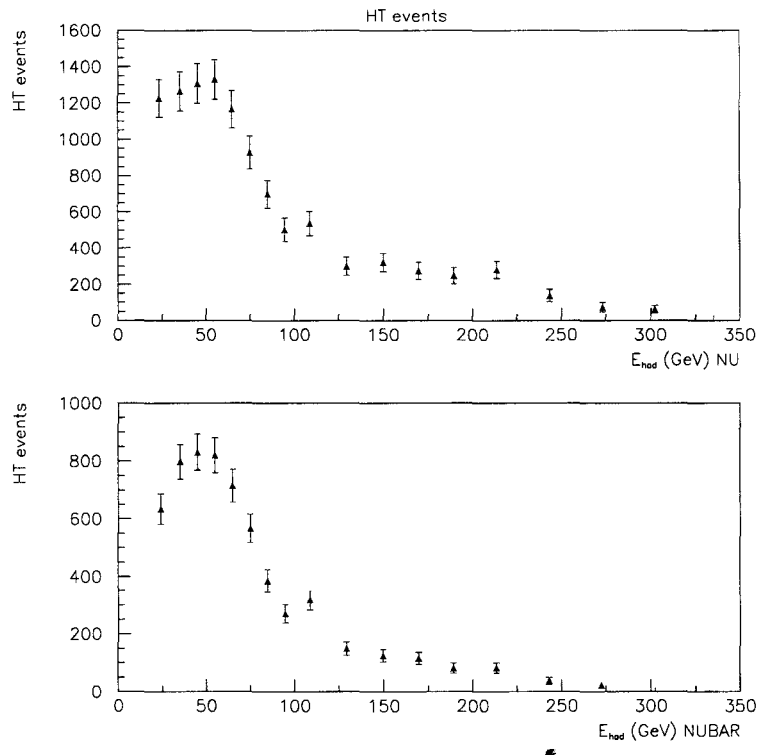


Figure 6.7: The (MC_{HT}) sample as a function of E_{ν} in ν (top) and $\bar{\nu}$ (bottom) modes. The error bars show only statistical errors.

QE events occur predominately in low Q^2 and low E_{had} region. Figure 6.9 compares the Q^2 distribution for the QE events extracted from our data, DT_{QE} , and that expected from C. H. Llewellyn Smith's QE model which is implemented in the MC, MC_{QE} . In $E_{had} < 5$ region in both $\nu/\bar{\nu}$ modes, DT_{QE} is higher than MC_{QE} . The DT_{QE} distributions show tails at $Q^2 > 2.5 \text{ GeV}^2$. However, in the $E_{had} > 5$ region, DT_{QE} is much less than MC_{QE} at low Q^2 . The DT_{QE} points are not consistent with zero. There is also a tail at high Q^2 distribution in this region as well. The magnitude

Neutrino energy	event $\pm\delta$ ν mode	event $\pm\delta$ $\bar{\nu}$ mode
$15 < E_\nu < 30$	1227 ± 103	634 ± 52
$30 < E_\nu < 40$	1265 ± 107	798 ± 60
$40 < E_\nu < 50$	1308 ± 110	831 ± 62
$50 < E_\nu < 60$	1330 ± 110	820 ± 60
$60 < E_\nu < 70$	1166 ± 103	715 ± 56
$70 < E_\nu < 80$	928 ± 91	567 ± 49
$80 < E_\nu < 90$	698 ± 77	386 ± 39
$90 < E_\nu < 100$	502 ± 65	270 ± 32
$100 < E_\nu < 120$	537 ± 68	317 ± 34
$120 < E_\nu < 140$	300 ± 50	149 ± 23
$140 < E_\nu < 160$	322 ± 51	125 ± 21
$160 < E_\nu < 180$	275 ± 48	116 ± 20
$180 < E_\nu < 200$	248 ± 45	82 ± 18
$200 < E_\nu < 230$	282 ± 47	83 ± 17
$230 < E_\nu < 260$	139 ± 34	38 ± 12
$260 < E_\nu < 290$	75 ± 25	23 ± 9
$290 < E_\nu < 320$	62 ± 21	9 ± 6
$320 < E_\nu < 360$	14 ± 14	2 ± 4

Table 6.3: The number of HT events in ν and $\bar{\nu}$ modes.

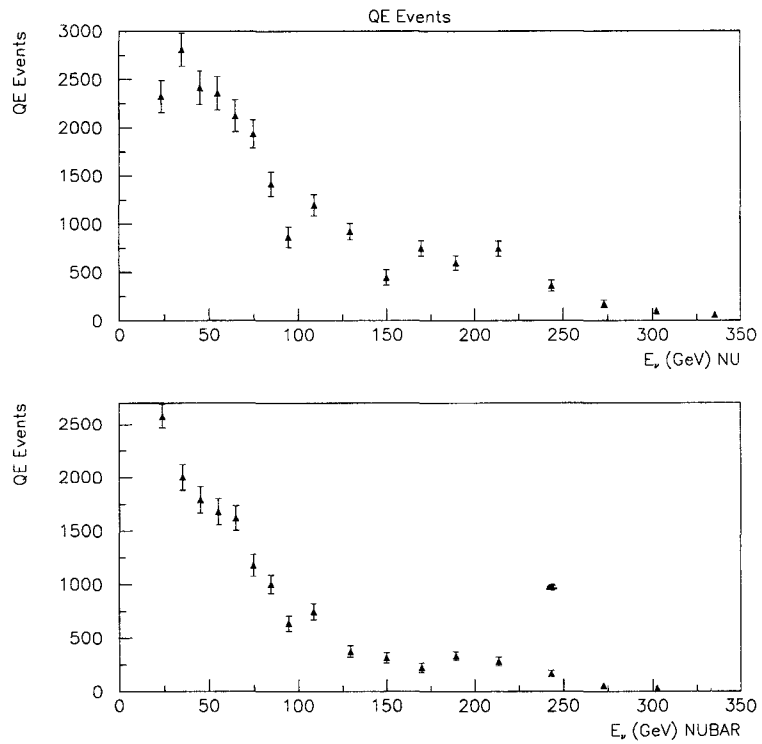


Figure 6.8: The QE sample as a function of E_ν in ν (top) and $\bar{\nu}$ (bottom) modes. The error bars show only statistical errors.

Neutrino energy	event $\pm\delta$ ν mode	event $\pm\delta$ $\bar{\nu}$ mode
$15 < E_\nu < 30$	2325 ± 165	2577 ± 113
$30 < E_\nu < 40$	2809 ± 171	2002 ± 121
$40 < E_\nu < 50$	2413 ± 175	1792 ± 123
$50 < E_\nu < 60$	2359 ± 173	1681 ± 121
$60 < E_\nu < 70$	2123 ± 164	1623 ± 114
$70 < E_\nu < 80$	1935 ± 147	1179 ± 102
$80 < E_\nu < 90$	1417 ± 126	1005 ± 86
$90 < E_\nu < 100$	865 ± 105	638 ± 70
$100 < E_\nu < 120$	1199 ± 112	747 ± 74
$120 < E_\nu < 140$	926 ± 86	377 ± 53
$140 < E_\nu < 160$	448 ± 81	316 ± 47
$160 < E_\nu < 180$	751 ± 80	227 ± 45
$180 < E_\nu < 200$	601 ± 75	332 ± 42
$200 < E_\nu < 230$	746 ± 79	282 ± 41
$230 < E_\nu < 260$	361 ± 58	168 ± 30
$260 < E_\nu < 290$	174 ± 42	56 ± 20
$290 < E_\nu < 320$	99 ± 31	32 ± 13
$320 < E_\nu < 360$	63 ± 21	20 ± 9

Table 6.4: The number of QE events in ν and $\bar{\nu}$ modes.

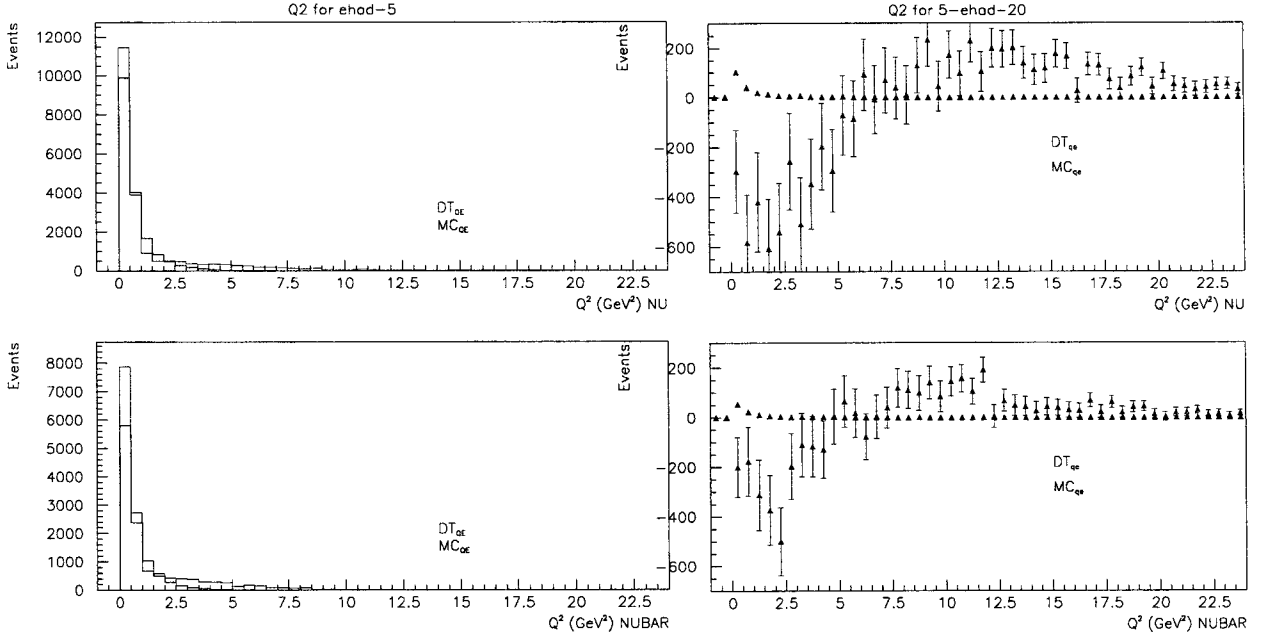


Figure 6.9: The QE sample as a function of Q^2 for $E_{had} < 5$ in ν (top) and $\bar{\nu}$ (bottom) modes. The left plots are in $E_{had} < 5$ region. The right plots are in $E_{had} > 5$ region. The extracted QE from NuTeV data are shown in red (DT_{QE}). Data is then compared to the MC which simulated only QE cross section and shown in blue (MC_{QE}).

of the tail is small compared to the one in the $E_{had} < 5$ region. We decide to ignore the tail in $Q^2 > 2.5$ GeV² region. Consider the tail in the $E_{had} < 5$ region, if it comes from the DIS, this tail should go to zero when $Q^2 = 0$. We extrapolate this tail as a constant between $2.5 < Q^2 < 5$ and subtract half of the integral from this region off the DT_{QE} events. The number of events summed from $2.5 < Q^2 < 5$ are listed in Table 6.5.

We also put a cut on $30 < E_\nu < 350$ GeV and $15 < E_\mu < 600$ GeV to remove the low energy events which are not well understood. The final events distribution that will be used to extract the QE cross section is shown in Fig. 6.10 and Table 6.6.

Neutrino energy	event $\pm\delta$ ν mode	event $\pm\delta$ $\bar{\nu}$ mode
$30 < E_\nu < 40$	148 ± 63	228 ± 44
$40 < E_\nu < 50$	127 ± 67	123 ± 46
$50 < E_\nu < 60$	294 ± 67	214 ± 47
$60 < E_\nu < 70$	116 ± 64	188 ± 45
$70 < E_\nu < 80$	236 ± 58	93 ± 40
$80 < E_\nu < 90$	187 ± 51	142 ± 35
$90 < E_\nu < 100$	104 ± 42	102 ± 29
$100 < E_\nu < 120$	117 ± 45	103 ± 30
$120 < E_\nu < 140$	95 ± 34	57 ± 22
$140 < E_\nu < 160$	69 ± 31	55 ± 19
$160 < E_\nu < 180$	42 ± 31	22 ± 18
$180 < E_\nu < 200$	11 ± 29	47 ± 17
$200 < E_\nu < 230$	114 ± 32	45 ± 17
$230 < E_\nu < 260$	67 ± 25	46 ± 13
$260 < E_\nu < 290$	-8 ± 17	11 ± 9
$290 < E_\nu < 320$	8 ± 12	10 ± 6
$320 < E_\nu < 360$	17 ± 9	5 ± 4

Table 6.5: The number of QE events in ν and $\bar{\nu}$ modes sum from $2.5 < Q^2 < 5 \text{ GeV}^2$ for each E_ν .

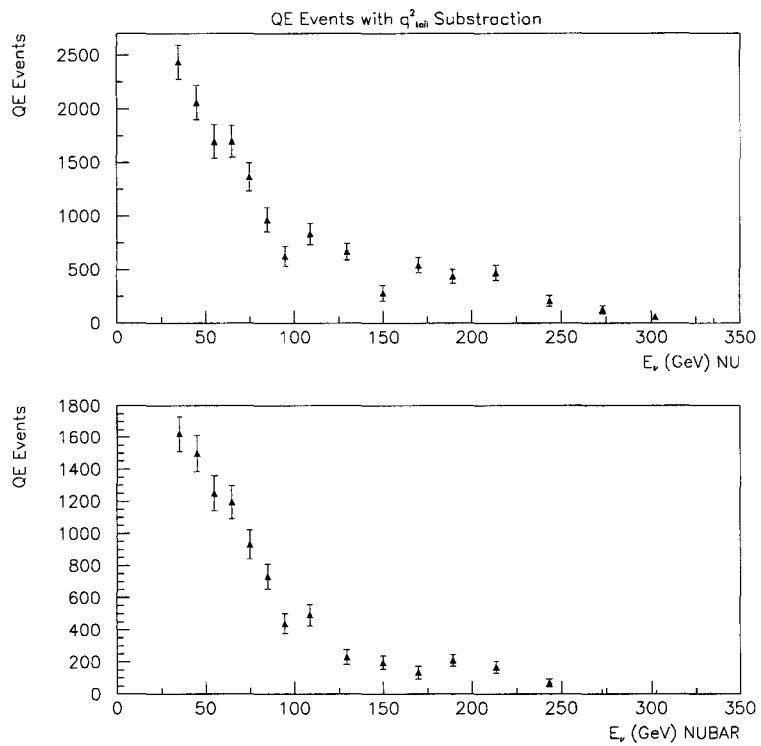


Figure 6.10: The QE sample as a function of E_ν in ν (top) and $\bar{\nu}$ (bottom) modes after applying $Q^2 < 2.5 \text{ GeV}^2$, $30 < E_\nu < 350 \text{ GeV}$ and $15 < E_\mu < 600 \text{ GeV}$ cuts.

Neutrino energy	event $\pm\delta$ ν mode	event $\pm\delta$ $\bar{\nu}$ mode
$30 < E_\nu < 40$	2378 ± 157	1588 ± 112
$40 < E_\nu < 50$	2002 ± 159	1495 ± 113
$50 < E_\nu < 60$	1674 ± 156	1226 ± 110
$60 < E_\nu < 70$	1689 ± 148	1199 ± 103
$70 < E_\nu < 80$	1371 ± 132	946 ± 92
$80 < E_\nu < 90$	971 ± 112	723 ± 77
$90 < E_\nu < 100$	606 ± 94	433 ± 63
$100 < E_\nu < 120$	806 ± 100	492 ± 66
$120 < E_\nu < 140$	663 ± 76	228 ± 47
$140 < E_\nu < 160$	290 ± 73	191 ± 42
$160 < E_\nu < 180$	561 ± 72	142 ± 40
$180 < E_\nu < 200$	446 ± 67	208 ± 37
$200 < E_\nu < 230$	469 ± 70	172 ± 36
$230 < E_\nu < 260$	196 ± 51	68 ± 25
$260 < E_\nu < 290$	125 ± 36	18 ± 17
$290 < E_\nu < 320$	56 ± 27	12 ± 11
$320 < E_\nu < 360$	20 ± 17	9 ± 7

Table 6.6: The number of QE events in ν and $\bar{\nu}$ modes with $Q^2 < 2.5 \text{ GeV}^2$, $30 < E_\nu < 350 \text{ GeV}$ and $15 < E_\mu < 600 \text{ GeV}$ cuts.

6.3 Quasi-Elastic Cross Section Extraction

The QE cross section is calculated from the absolute flux and the number of QE events is as follows:

$$\sigma_{qe}(E) = \frac{N_{qe}(E)}{\Phi(E)} \times Acc_{corr}^{qe}(E), \quad (6.18)$$

where

$$\begin{aligned} N_{qe}(E) &= \sum_{Q^2 < 2.5} \sum_{\nu=-5}^5 N_{qe}(E, \nu) \\ Acc_{corr}^{qe}(E) &= \frac{\sum_{all \nu} MC_{QE}^{gen}(E, \nu)}{\sum_{\nu=-5}^5 MC_{QE}^{smr}(E, \nu)} \end{aligned} \quad (6.19)$$

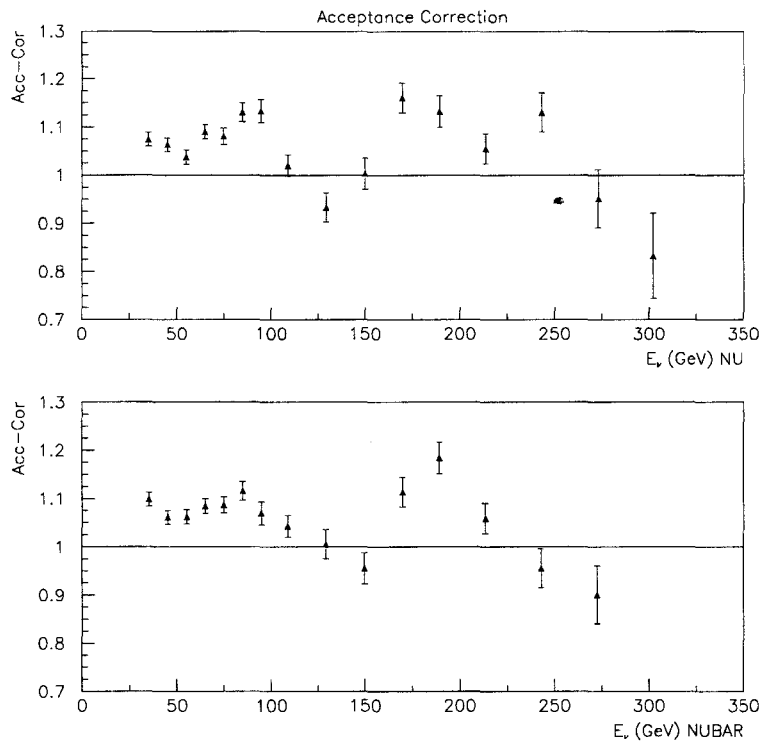


Figure 6.11: The acceptance correction in ν (top) and $\bar{\nu}$ (bottom) modes.

$Acc_{corr}^{qe}(E)$ is the acceptance correction for QE events. MC_{QE}^{gen} and MC_{QE}^{smr} are generated and smeared MC events which have only C. H. Llewellyn Smith's QE cross section model. The $Acc_{corr}^{qe}(E)$ distribution is shown in Fig. 6.11.

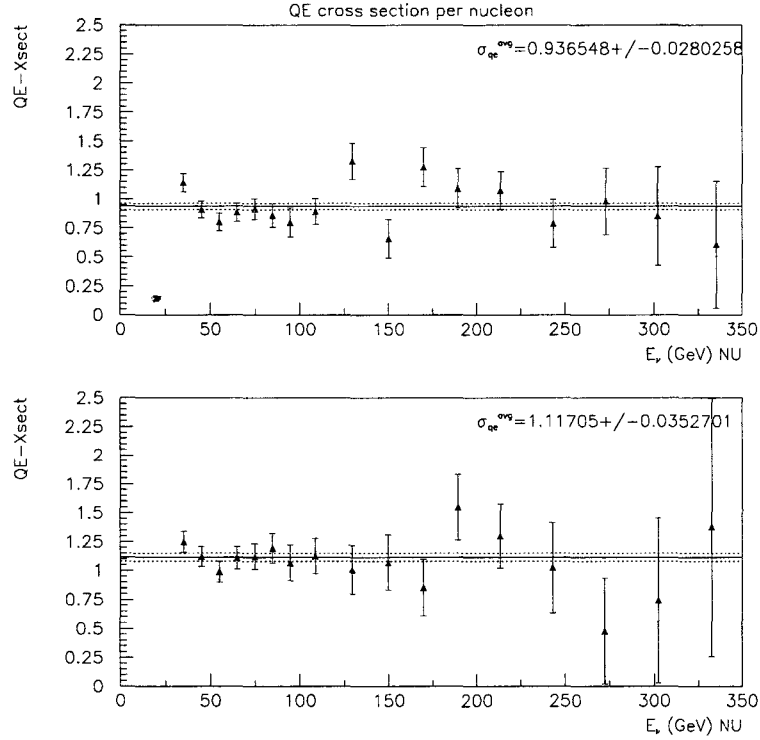


Figure 6.12: The σ_{qe} per nucleon as a function of E_ν in ν (top) and $\bar{\nu}$ (bottom) modes. The solid line is the the average of σ_{qe} . The dash lines represent \pm error.

The QE cross section extracted from Eq. 6.18 are for an iron target. The average of $\sigma_{qe}(E)$ for $30 < E_\nu < 300$ in ν and $\bar{\nu}$ modes are 0.49 ± 0.01 with $\chi^2/dof = 1.9$ and 0.53 ± 0.02 with $\chi^2/dof = 0.74$, respectively.

To obtain the QE-cross section per neutron for neutrino scattering and per proton for anti-neutrino scattering one needs to multiply $\sigma_{qe}^{\nu, \bar{\nu}}$ with factors of $A/N = 1.8927$ and

Neutrino energy	$\sigma_{qe} \pm \delta\sigma_{qe}$ ν mode	$\sigma_{qe} \pm \delta\sigma_{qe}$ $\bar{\nu}$ mode
$30 < E_\nu < 40$	1.14 ± 0.08	1.25 ± 0.09
$40 < E_\nu < 50$	0.91 ± 0.07	1.12 ± 0.09
$50 < E_\nu < 60$	0.80 ± 0.08	0.99 ± 0.09
$60 < E_\nu < 70$	0.89 ± 0.08	1.11 ± 0.10
$70 < E_\nu < 80$	0.92 ± 0.09	1.12 ± 0.11
$80 < E_\nu < 90$	0.86 ± 0.10	1.19 ± 0.13
$90 < E_\nu < 100$	0.80 ± 0.13	1.07 ± 0.16
$100 < E_\nu < 120$	0.89 ± 0.12	1.13 ± 0.15
$120 < E_\nu < 140$	1.33 ± 0.16	1.01 ± 0.21
$140 < E_\nu < 160$	0.66 ± 0.17	1.07 ± 0.24
$160 < E_\nu < 180$	1.28 ± 0.17	0.86 ± 0.24
$180 < E_\nu < 200$	1.09 ± 0.17	1.55 ± 0.28
$200 < E_\nu < 230$	1.08 ± 0.16	1.30 ± 0.28
$230 < E_\nu < 260$	0.79 ± 0.21	1.03 ± 0.39
$260 < E_\nu < 290$	0.98 ± 0.29	0.48 ± 0.46
$290 < E_\nu < 320$	0.85 ± 0.42	0.74 ± 0.71
$320 < E_\nu < 360$	0.61 ± 0.53	1.38 ± 1.12

Table 6.7: The total QE cross section per nucleon for an iron target in ν and $\bar{\nu}$ modes.

$A/Z = 2.1202$ for $\nu - n$ and $\bar{\nu} - p$ processes, respectively. $Z = 23.403$, $N = 26.215$, and $A = Z + N$ are the number of protons, neutrons, and nucleons for calorimeter target calculated in [38], respectively. The $\sigma_{qe}^{BoundNucleon(\nu,\bar{\nu})}$ is 0.94 ± 0.03 and 1.12 ± 0.04 . The extracted values of QE cross section are listed in Table 6.7 and 6.8 and shown in Fig. 6.12. The solid line in the plots show the average of $\sigma_{qe}^{\nu-n(\bar{\nu}-p)}$. The dash lines represent only the statistical error interval around the average.

The QE cross section in a bound nucleon is different from the one for a free nucleon due to the binding energy effect. We need to take into account the Pauli suppression in those processes. Ref. [39] shows that the total QE neutrino cross section for iron per neutron is reduced by a factor of 0.923 from that of free neutrons and the anti-

neutrino cross section per proton is reduced by 0.917.

	$\sigma_{qe}^{BoundNucleon}$	χ^2 per DOF
ν	0.94 ± 0.03	1.86
$\bar{\nu}$	1.12 ± 0.04	0.74

Table 6.8: The NuTeV total QE cross section per bound nucleon in ν and $\bar{\nu}$ modes. The magnitude is 10^{-38} .

Chapter 7

Systematic Errors

This chapter discusses about the systematic errors in this analysis. The estimation of the systematic uncertainty is obtained by varying parameters and cuts by reasonable amounts. The sources of the systematic errors are divided into three categories:

- The experimental systematics;
- The cross section extraction systematics; and
- The model systematics.

7.1 The Experimental Systematics

These errors are associated with the energy calibration. The energy measured by NuTeV detector is known to better than 0.43% level for E_{had} and 0.70% level for E_μ [40]. We test the sensitivity of energy measurement by shifting the E_{had} and E_μ in the data events up and down by 0.50% and 0.70%, respectively. Shifting E_{had} up increases the quasi-elastic (QE) cross section by 0.76% in ν mode but decreases 0.09% in $\bar{\nu}$ mode. Shifting E_{had} down decreases the QE cross section by 0.52% in ν mode

but increases 0.06% in $\bar{\nu}$ mode. Shifting E_μ up decreases the QE cross section by 3.00% and 1.85% in ν and $\bar{\nu}$ modes, respectively. Shifting E_μ down increases the QE cross section by 3.00% and 2.10% in ν and $\bar{\nu}$ modes, respectively.

The errors due to shifting energy up and down are correlated. We need to take into account the correlation relation. Our combined systematic errors due to shifting the E_{had} and E_μ up and down are 0.64% and 3.00% for ν mode and 0.07% and 1.98% for $\bar{\nu}$ respectively.

7.2 The Cross Section Extraction Systematics

7.2.1 Flux Extraction Methods

We have extracted the flux by using another flux extraction method to study its systematic error. An alternative method [41] is to fit the number of corrected events and extract the $\frac{B}{A}$ as follows:

$$\Delta N(E, \nu) = \left[A'' \left(1 - \frac{\nu}{E} + \frac{\nu^2}{2E^2} (1 + \tilde{R}) \right) + B'' \left(\frac{\nu}{E} - \frac{\nu^2}{2E^2} \right) \right], \quad (7.1)$$

where A'' and B'' are rescaled with $\int F_2(\nu) / \int F_2(\nu = 12)$ and $\int xF_3(\nu) / \int xF_3(\nu = 12)$, respectively (the model allows scaling violations in the quark model). The choice of $\nu = 12$ is selected because it is the middle value between $4 < \nu < 20$ GeV. There is no significant difference in the value of theoretically calculated $\frac{B}{A}$ for $12 < \nu < 20$ GeV.

This method applies the higher twist (HT) effects to the deep inelastic scattering

(DIS) cross section when corrected for the physics model correction. This is different from the one we use in our analysis. Previously we do not include the HT effect in the DIS cross section when corrected for the physics model correction. Using this alternative flux extraction, the QE cross section decreases by 0.26% and 0.19% in neutrino and anti-neutrino modes, respectively. Thus we assign those values as systematic error to our flux extraction.

7.2.2 Q^2 Tail in $E_{had} < 5$ Region

Figure 6.9 shows the Q^2 distribution of QE events for $E_{had} < 5$. The plots show the tail at $Q^2 > 2.5$. We extrapolate this tail down to zero as Q^2 goes to zero by subtracting half of the integral from $2.5 < Q^2 < 5$. The systematic error of the Q^2 tail is from the difference between the one with the tail subtraction and without it. They are 6.04% and 8.13% in neutrino and anti-neutrino modes, respectively.

7.3 The Model Systematics

7.3.1 M_A and F_A in C. H. Llewellyn Smith Quasi-elastic Model

From Eq. 2.50:

$$\frac{d\sigma}{d|q^2|} \begin{pmatrix} \nu n \rightarrow l^- p \\ \bar{\nu} p \rightarrow l^+ n \end{pmatrix} = \frac{M^2 G_F^2 \cos^2 \theta_c}{8\pi E_{\nu, \bar{\nu}}^2} \left[A(q^2) \mp B(q^2) \frac{(s-u)}{M^2} + \frac{C(q^2)(s-u)^2}{M^4} \right], \quad (7.2)$$

the QE differential cross section is dominated by the A term where A depends on F_A :

$$A = \frac{-q^2}{4M^2} \left[\left(4 - \frac{q^2}{M^2}\right) |F_A|^2 - \left(4 + \frac{q^2}{M^2}\right) |F_V^1|^2 - \frac{q^2}{M^2} \left(1 + \frac{q^2}{4M^2}\right) |\xi F_V^2|^2 - \frac{4q^2}{M^2} (F_V^1 \xi F_V^2) \right], \quad (7.3)$$

and F_A related to M_A by:

$$F_A(q^2) = \frac{F_A(0)}{\left(1 - \frac{q^2}{M_A^2}\right)^2}, \quad (7.4)$$

Theoretically increasing or decreasing M_A by 10% also increases or decreases the QE cross section by 10% in both ν and $\bar{\nu}$ modes. We apply this effect to the acceptance correction in Eq. 6.19. The extracted QE cross section changes 0.68% and 0.60% in ν and $\bar{\nu}$ modes, respectively. These value will be used as our systematic errors.

7.3.2 Limit on Higher Twist at High x

The HT model used in this analysis is from fitting SLAC data. The fit gives Eq. 2.72:

$$ht(x) = \begin{cases} 0 & \text{for } x < 0.4 \text{ and } ht < 0 \\ 0.672\left(\frac{x^{1.893}}{1-1.138x} - 0.236\right) & \text{for } x \leq 0.8 \\ 10 & \text{for } x > 0.8 \end{cases} \quad (7.5)$$

The HT effect is applied to the low energy events. We set HT to be bounded between 0 and 10. The cut-off at 10 is based on a comparison of the model to SLAC data [42]. We estimate the systematic error on the HT effect by changing this cut-off to be 7.5. The QE cross sections increase by 3.68% and 4.10% for ν and $\bar{\nu}$, respectively. They are used as a HT systematic errors for this study.

These systematic errors are assumed to be independent and thus can be added in

quadrature. The total systematic errors for the QE cross section for bound nucleon in Fe target from different sources are shown in Table 7.1. Our final extracted QE cross section for bound nucleon in Fe target becomes:

$$\sigma_{qe}(\nu_{\mu} + n \rightarrow \mu^{-} + p) = 0.94 \pm 0.03(stat.) + 0.07(syst.), \quad (7.6)$$

and

$$\sigma_{qe}(\bar{\nu}_{\mu} + p \rightarrow \mu^{+} + n) = 1.12 \pm 0.04(stat.) + 0.10(syst.). \quad (7.7)$$

Source of Sytematic Uncertainty	$\delta\sigma_{qe}^{\nu}$	$\delta\sigma_{qe}^{\bar{\nu}}$
Shift E_{had} up/down 0.5%	0.0060	0.0008
Shift E_{μ} up/down 0.7%	0.0281	0.0221
Flux Extraction Method	0.0024	0.0021
q^2 Tail Subtraction	0.0565	0.0908
Acceptance Correction due to shift M_A by 10%	0.0064	0.0067
Shift Higher Twist Limit to 7.5	0.0345	0.0458
Total of Systematic Uncertainty	0.0725	0.1043

Table 7.1: The systematic uncertainty in this analysis treated as bound nucleon.

Chapter 8

Conclusion

This thesis has presented a measurement of the quasi-elastic (QE) cross section from a neutrino (anti-neutrino)-nucleon scattering processes at the Tevatron. This is the first measurement for the high neutrino energy ($30 < E_\nu < 300$ GeV) QE cross section.

We extracted the events using a Monte Carlo (MC) program called NUMONTE which is well described the deep inelastic scattering (DIS) data. We subtract the MC DIS events from the data and get NON-DIS events. We use higher twist (HT) model to account for the low energy resonances (RES) events. The HT model is a model that well described the DIS events at high energy and the RES events at low energy. The QE events are then calculated from the subtraction of HT events from the NON-DIS events. We extracted the flux by using the charged current (CC) DIS events and normalized it to the world CC DIS isoscalar cross section.

The average values of QE cross section for bound nucleon in Fe target in ν and $\bar{\nu}$

from $30 < E_\nu < 300$ are:

$$\sigma_{qe}^{Nucleon}(\nu) = 0.94 \pm 0.03(stat.) \pm 0.07(syst.), \quad (8.1)$$

and

$$\sigma_{qe}^{Nucleon}(\bar{\nu}) = 1.12 \pm 0.04(stat.) \pm 0.10(syst.). \quad (8.2)$$

We include our high energy data to the low energy ones from other experiments (Ref [43, 44, 45, 46, 47, 48, 49]). Figure 8.1 and 8.2 show the QE scattering cross section for the following process:

$$\nu_\mu n \rightarrow \mu^- p, \quad (8.3)$$

and

$$\bar{\nu}_\mu p \rightarrow \mu^+ n. \quad (8.4)$$

The points shown in the figures are for bound nucleon. The extracted QE cross section in ν mode agrees within statistical and systematic uncertainties with a prediction from NUANCE. (NUANCE is an MC package and predicts QE cross section using C. H. Llewellyn Smith's QE model with $M_A = 1.0$ GeV, $M_V = 0.84$ GeV, and $F_A(0) = -1.25$.) The extracted QE cross sections in $\bar{\nu}$ mode are higher than the prediction and within two standard deviation of the statistical and systematic uncertainties. Table 8.1 shows the QE cross section per free nucleon which have been corrected for Pauli suppression and compare with the one calculated from NUANCE at $E_\nu = 200$ GeV.

CC ν_μ Quasi-Elastic Cross Section

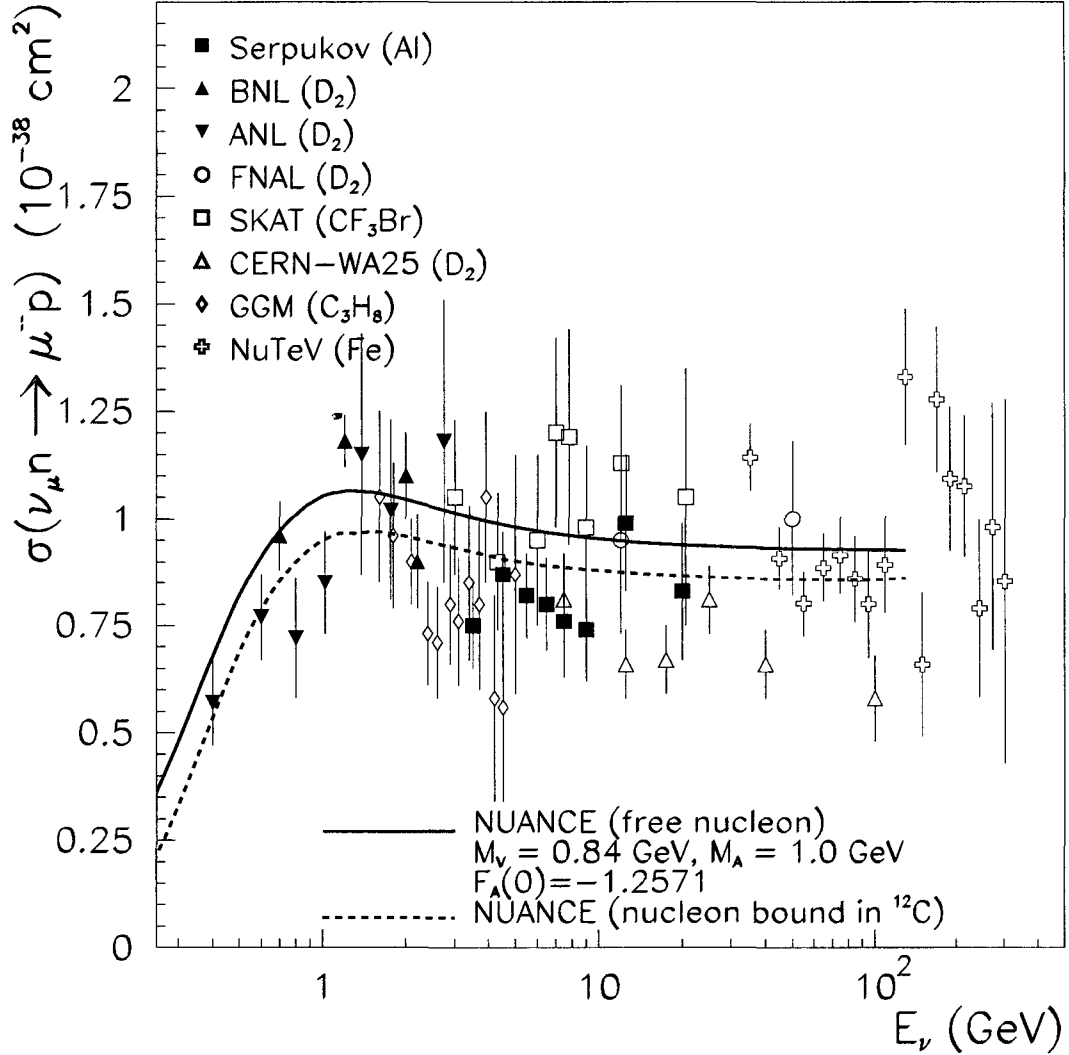


Figure 8.1: The QE cross section $\sigma(\nu_\mu n \rightarrow \mu^- p)$ as a function of E_ν for a bound nucleon. The data points are from this experiment and some other experiments. The solid line is the prediction for free nucleon. The dash line is for bound nucleon in carbon. We include only the statistical errors in our data.

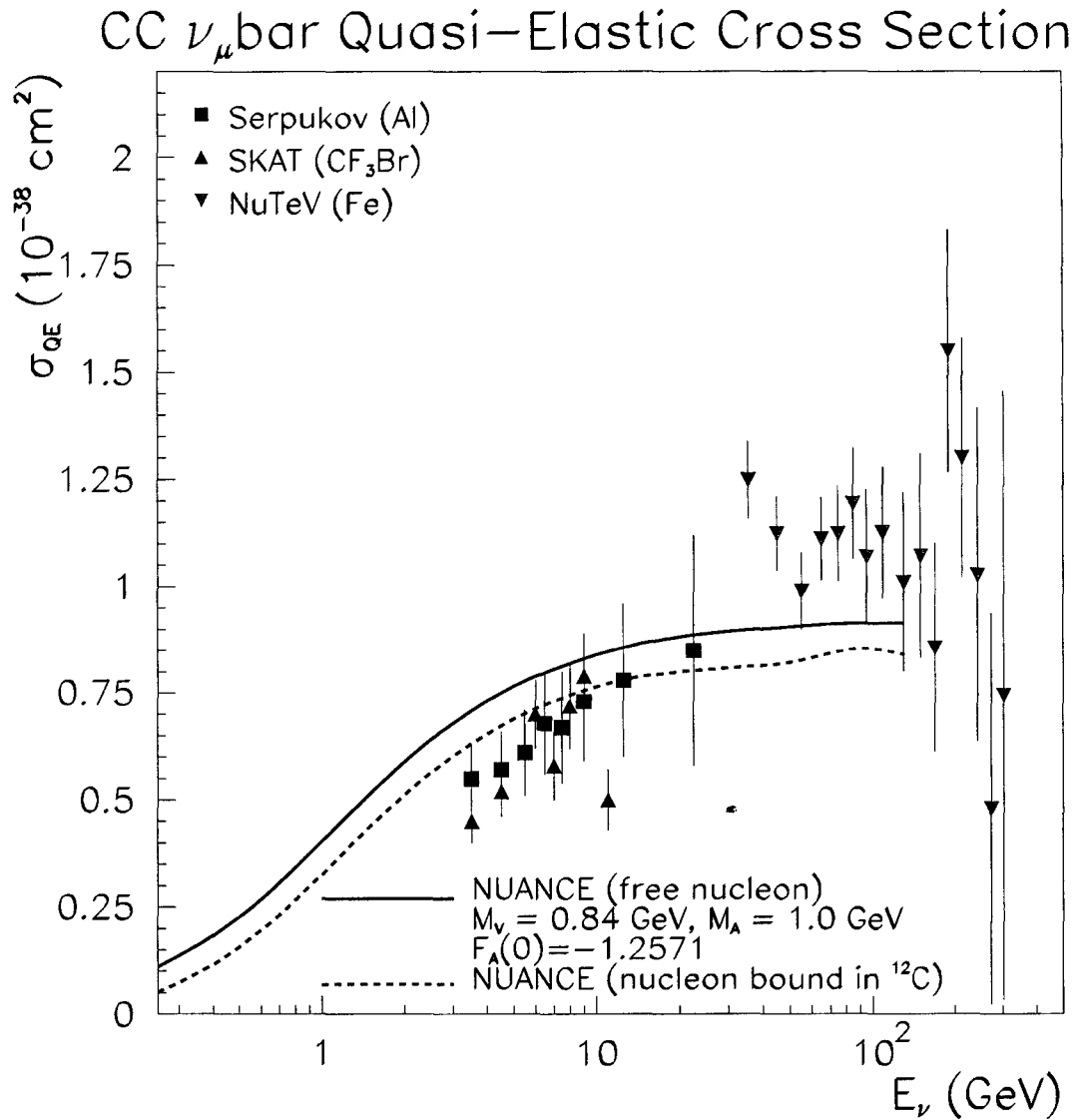


Figure 8.2: The QE cross section $\sigma(\bar{\nu}_\mu p \rightarrow \mu^+ n)$ as a function of E_ν for a bound nucleon. The data points are from this experiment and some other experiments. The solid line is the prediction for free nucleon. The dash line is for bound nucleon in carbon. We include only the statistical errors in our data.

Our QE events are extracted by the subtraction of DIS and HT from the data. We assume that our MC describes DIS events well. The HT events is extracted as an average of the RES production. The Q^2 plot in Fig. 6.9 show that our extracted QE data is higher than the one predicted from MC. This may indicate that there are other types of events besides QE and RES at low q^2 or the HT model used in our analysis does not include all the RES productions. In addition, as noted before changing the value of M_A will also change the QE cross section by the same percentage. These may cause the QE cross section higher than predicted one.

	$\sigma_{qe}^{FreeNucleon}$	$\sigma_{qe}^{FreeNucleon}(E_\nu = 200)$ from NUANCE
ν	$1.01 \pm 0.03 \pm 0.08$	0.93
$\bar{\nu}$	$1.22 \pm 0.04 \pm 0.11$	0.92

Table 8.1: The NuTeV total QE cross section per free nucleon in ν and $\bar{\nu}$ modes. The magnitude is 10^{-38} . They have been corrected for nucleon target and Pauli suppression in order to compare with the theoretical vaules. The last column shows the total QE cross section per free nucleon from NUANCE at $E = 200$ GeV. NUANCE is a Monte Carlo which simulates the QE cross section using Llewellyn Smith QE model with $M_V = 0.84$, $M_A = 1.0$ and $F_A(0) = -1.2571$.

Appendix A

Place Study

The hadron and muon energy depend on $SHEND$ as shown previously in Eq 4.1 and Eq. 4.4. In the Monte Carlo $SHEND$ is thrown against the length distribution. One needs to ensure that the correct length distribution is used as an input length distributions for NUMONTE. Previously we used the length distributions from CCFR data and assumed that the distributions are the same for NuTeV data. Besides we assume that the distributions are the same in both neutrino and anti-neutrino modes. The distributions are also a function of E_{had} and calculated as follows:

$$LENGTH = PLACE - (SHEND - 5) \quad (A.1)$$

The length distributions for different E_{had} bin from CCFR and NuTeV in neutrino and anti-neutrino modes are shown in Fig. A.1 and Fig. A.2, respectively. These plots show strongly disagreement in the length distributions between CCFR and NuTeV data at low E_{had} . They also show that the output CCFR length distributions from NUMONTE are shifted from the input CCFR ones by approximately 0.5 counter.

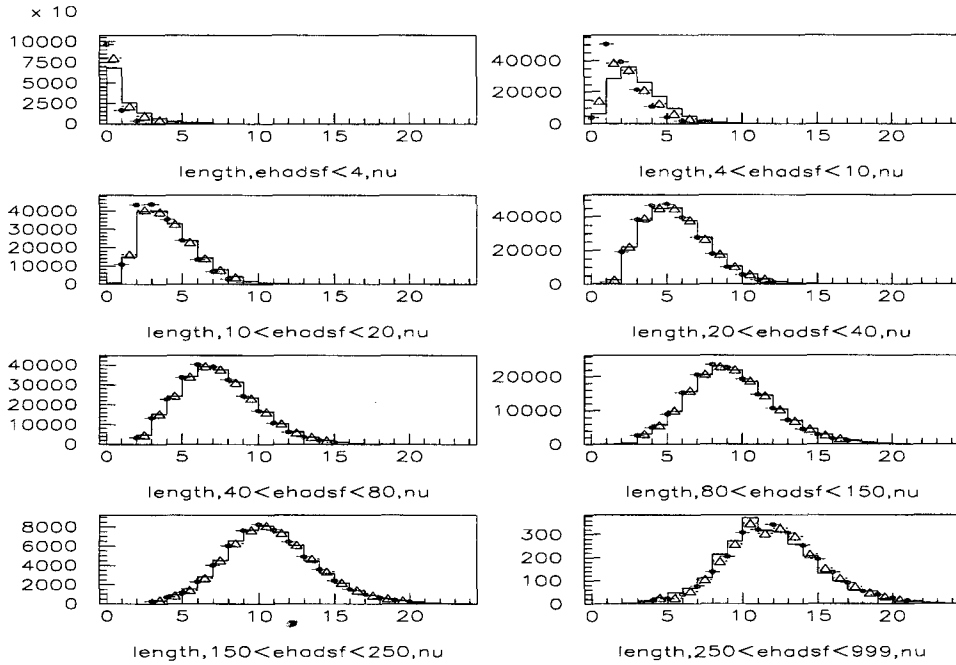


Figure A.1: The length distribution comparison of CCFR data (red dot) to NuTeV data (black histogram) and output from NUMONTE with CCFR input (blue triangle) in neutrino mode.

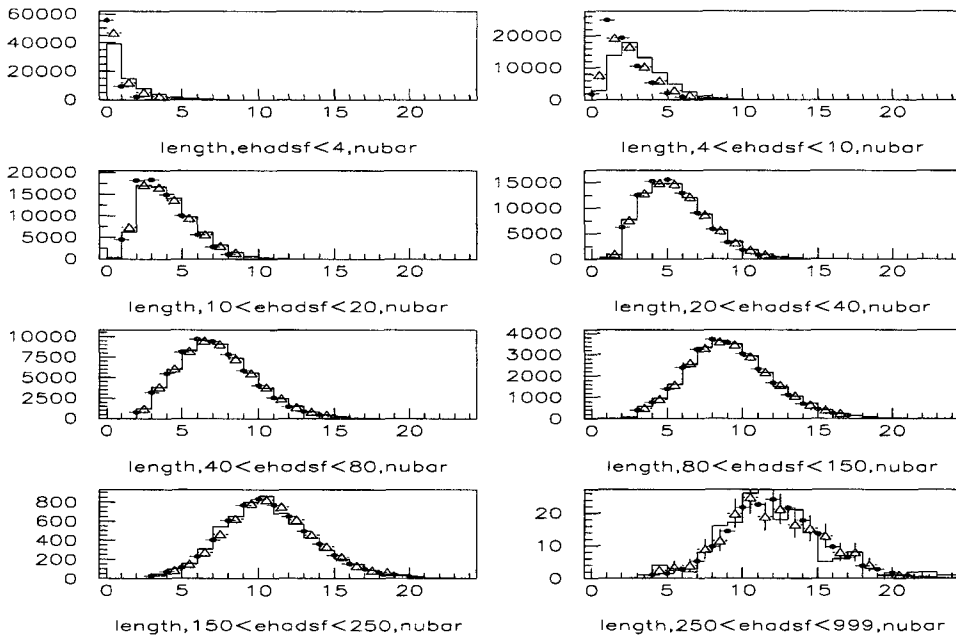


Figure A.2: The same comparison in anti-neutrino mode.

We then use NuTeV data as an input for NUMONTE and plot the output length distribution in two different ways, $PLACE-(SHEND-5)$ and $PLACE-(SHENDSF-5)$. $SHEND$ is the counter where the shower ends without any smearing and $SHENDSF$ includes smearing effect. We also remove the shift by 0.5 in the input length distributions. Figure A.3 - A.4 shows NuTeV data as an input distribution compares to the output length distribution using $SHEND$ and $SHENDSF$ in ν and $\bar{\nu}$ modes, respectively. The plot shows a good agreement in length distributions between NuTeV data and the output using $SHENDSF$ which is what expected. The agreement holds in all energy bins. We decide to use the length distributions from NuTeV data as an input for NUMONTE and remove the shift by 0.5. The E_{had} distribution comparison between NuTeV data and the output from NUMONTE with and without a 0.5 shift using NuTeV length distribution as input are shown in Fig. A.5.

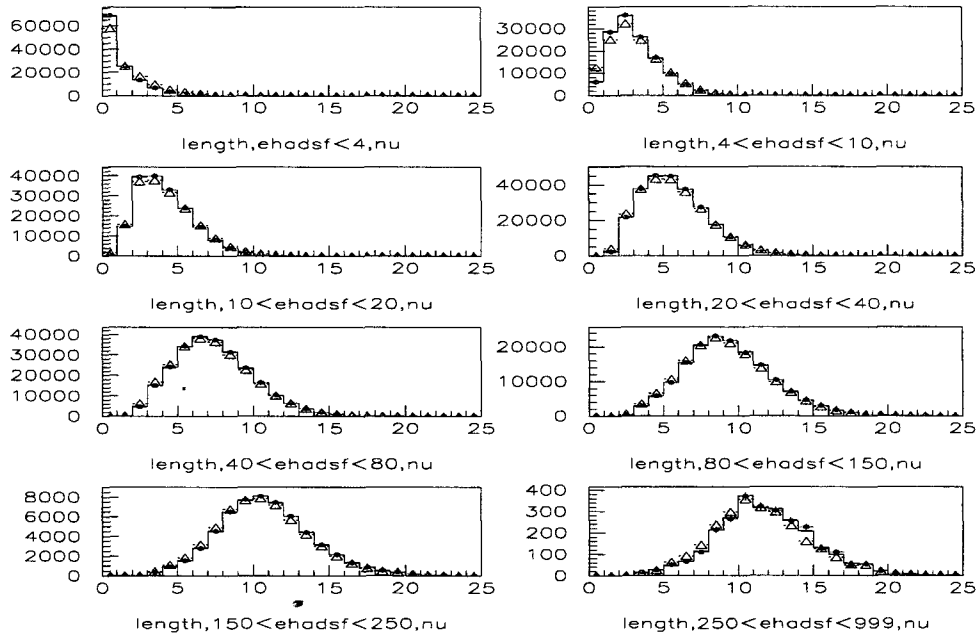


Figure A.3: The length distribution comparison between NuTeV data after removing the shift by 0.5 (black histogram) and output from NUMONTE with the new NuTeV data as an input using *SHEND* (blue triangle), and *SHENDSF* (red dot) in neutrino mode.

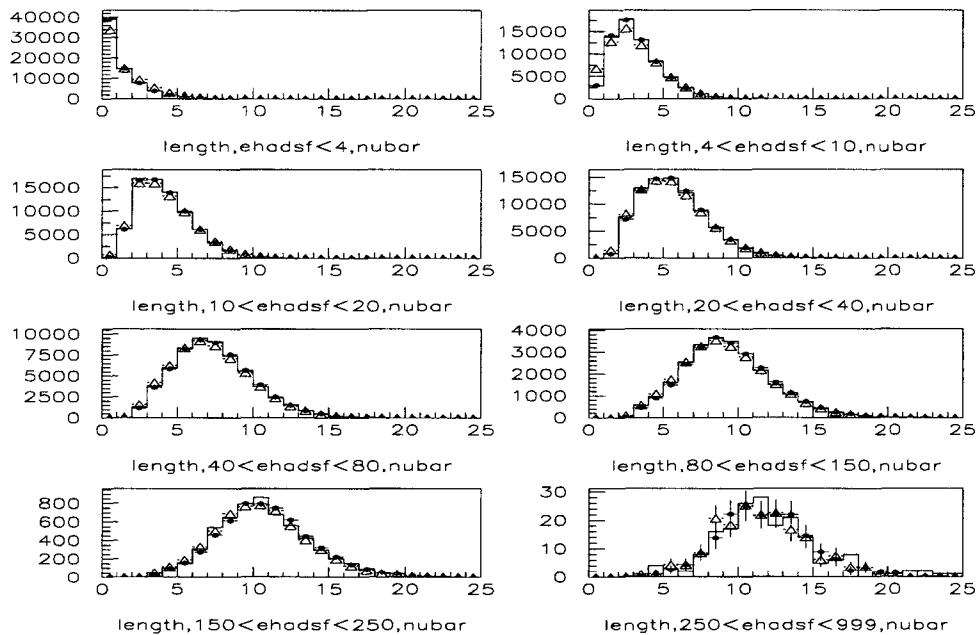


Figure A.4: The same comparison in anti-neutrino mode.

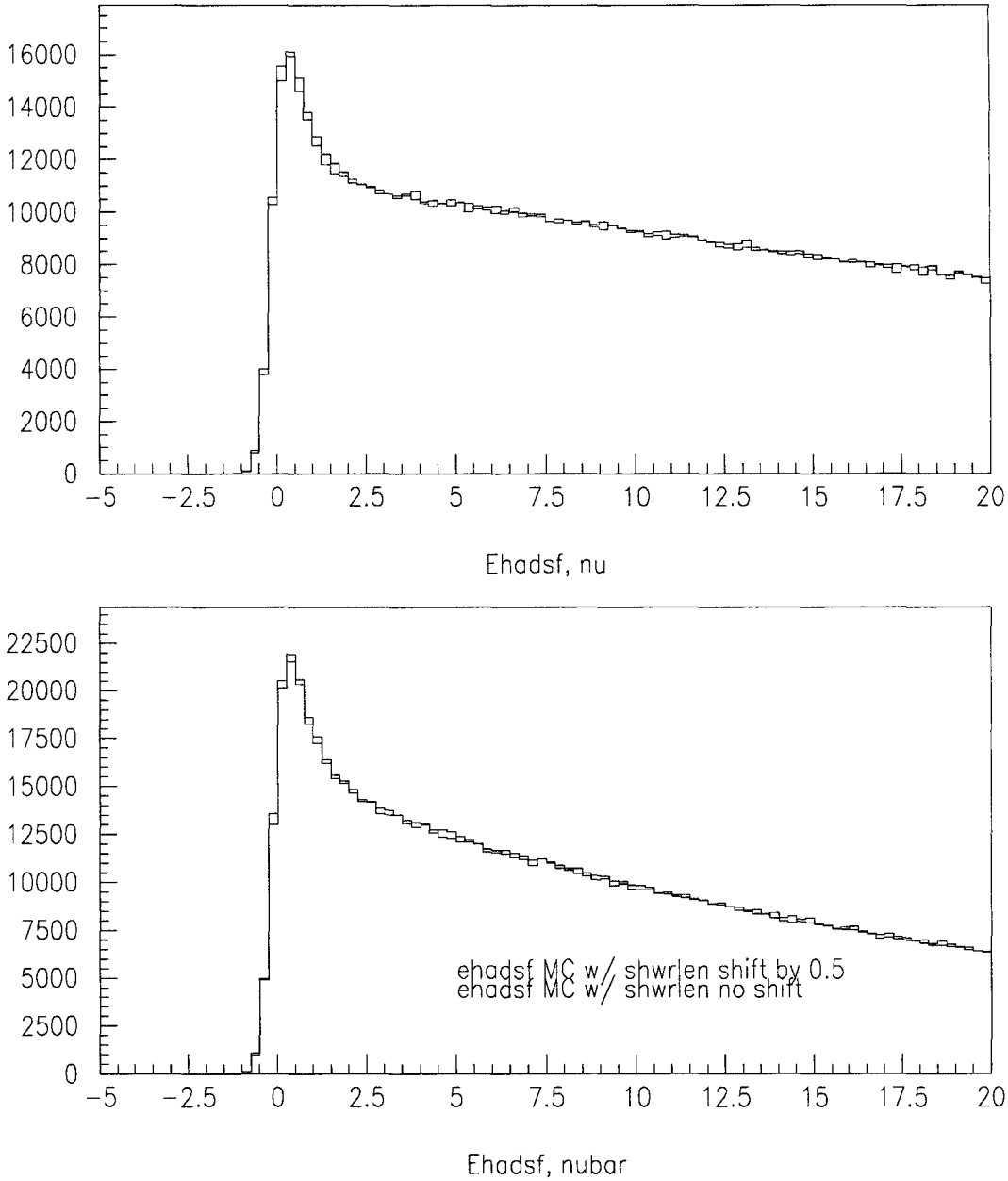


Figure A.5: The E_{had} distribution comparison between output from NUMONTE with (red) and without (blue) 0.5 shift in ν (top) and $\bar{\nu}$ (bottom) modes.

Figure A.6 - A.7 show the two-dimensional plots of E_{had} distribution versus the length distribution for NuTeV data (DT) and Monte Carlo (MC) output using *SHENDSF* in neutrino mode, respectively. As we can see from the top left plots in those two figures, the curvature of the two-dimensional plot along E_{had} are different. DT has a smooth curvature while MC has a cut off at $E_{had} \approx 4$ GeV. The other three plots show the projection of *LENGTH* distribution for different E_{had} . They show similar distribution between DT and MC. The cut off at 4 GeV may come from the fact that we use the length distribution from NuTeV data with the limit of 4, 10, 20, 40, 80, 150, 250, and 9999 GeV. Similar results in anti-neutrino mode are shown in Fig. A.8 - A.9.

Due to the cut off at $E_{had} \approx 4$ GeV where the quasi-elastic events dominate, we further study on length distribution by subdividing the E_{had} region into smaller region, as follows: 0, 1, 2, 3, ..., 10, 15, 20, 40, 80, 150, 250, and 9999 GeV.

Figure A.10 - A.11 show the length distributions of NuTeV data with smaller E_{had} bins in neutrino and anti-neutrino modes, respectively. We then re-apply these new distributions into NUMONTE. The two-dimensional histograms of E_{had} versus length distributions using *SHENDSF* as done previously are shown in Fig. A.12 - A.13. The plots show better agreement in all regions with the smaller E_{had} bins.

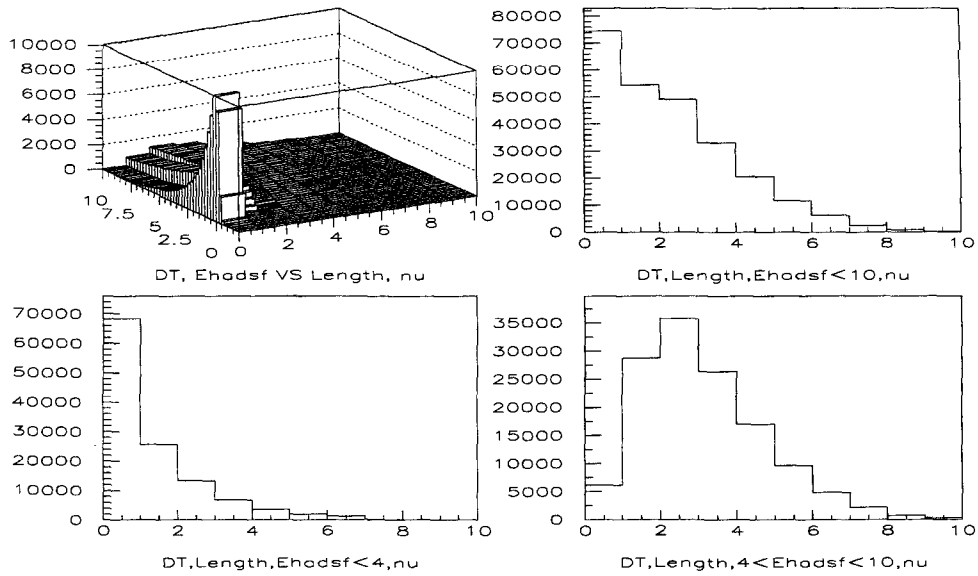


Figure A.6: The distribution from NuTeV data in ν mode. The top left plot shows the 2D lego plot of the length distribution (x-axis) versus the E_{had} distribution (y-axis). The top right plot shows the length distribution for $E_{had} < 10$. The bottom left plot shows the length distribution for $E_{had} < 4$. The bottom right plot shows the length distribution for $4 < E_{had} < 10$.

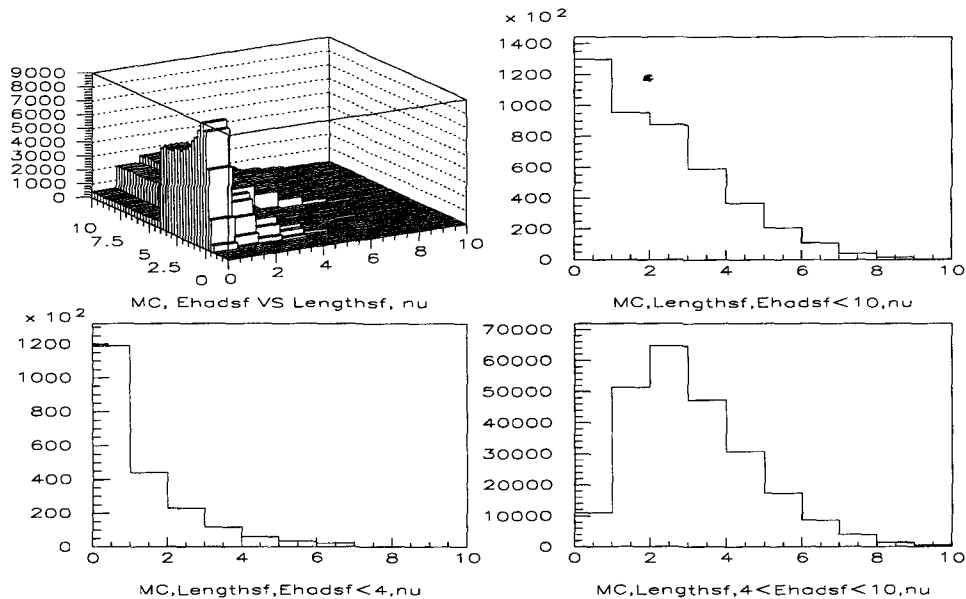


Figure A.7: The same distribution for output NUMONTE using NuTeV length distribution with big E_{had} step in ν mode.

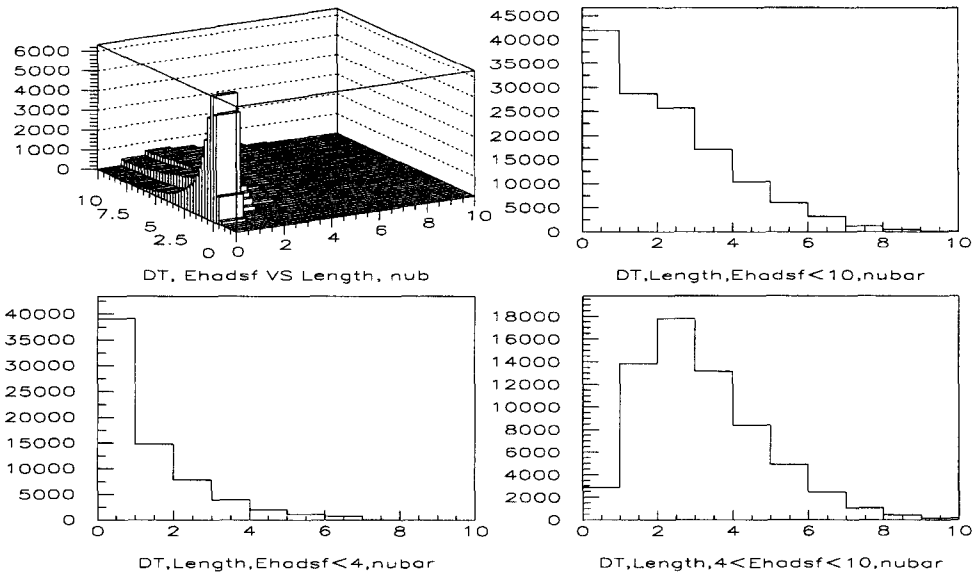


Figure A.8: The distribution from NuTeV data in $\bar{\nu}$ mode. The top left plot shows the 2D lego plot of the length distribution (x-axis) versus the E_{had} distribution (y-axis). The top right plot shows the length distribution for $E_{had} < 10$. The bottom left plot shows the length distribution for $E_{had} < 4$. The bottom right plot shows the length distribution for $4 < E_{had} < 10$.

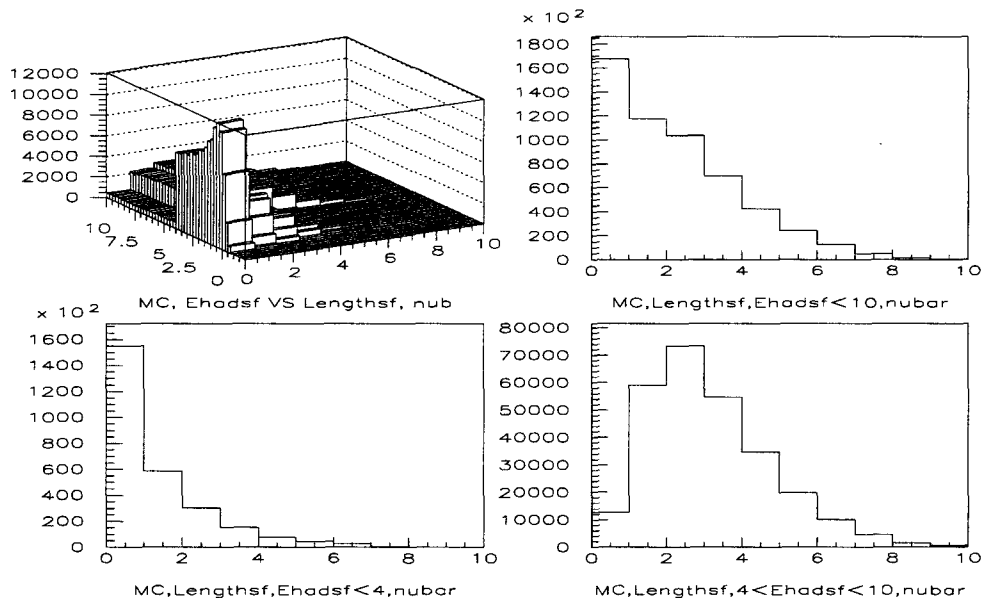


Figure A.9: The same distribution for output NUMONTE using NuTeV length distribution with big E_{had} step in $\bar{\nu}$ mode.

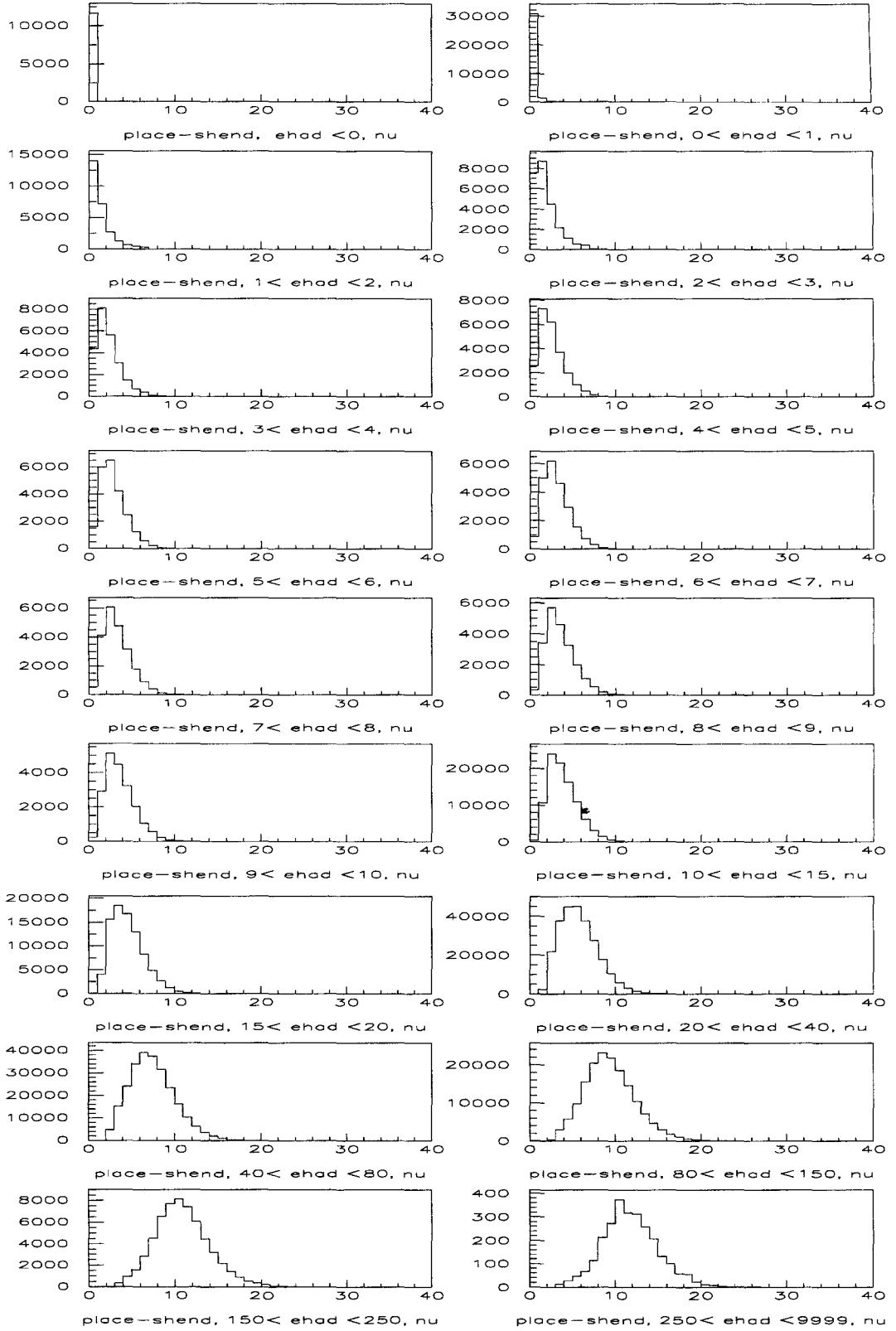


Figure A.10: The NuTeV length distribution with finer E_{had} bins in ν mode.

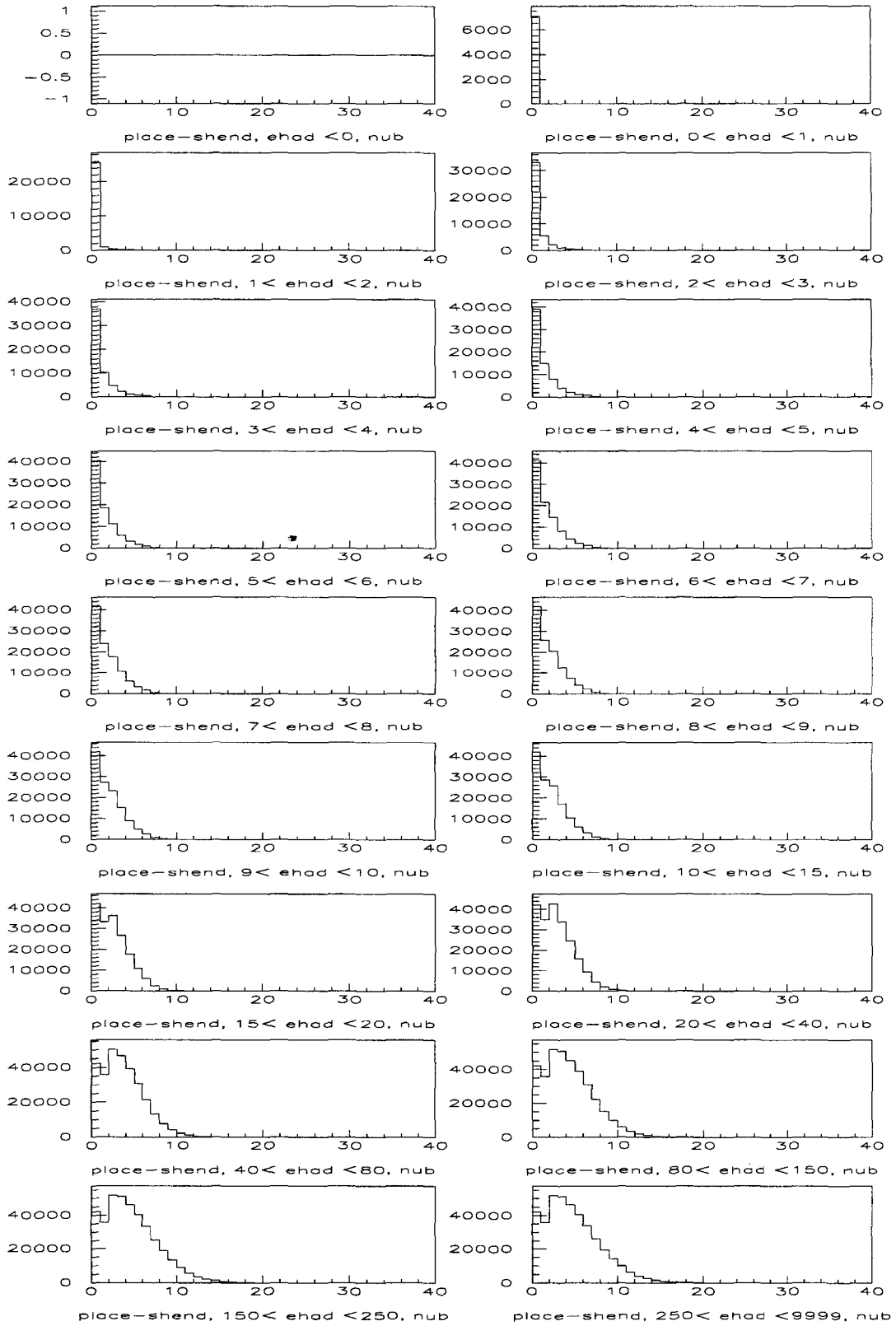


Figure A.11: The NuTeV length distribution with finer E_{had} bins in $\bar{\nu}$ mode.

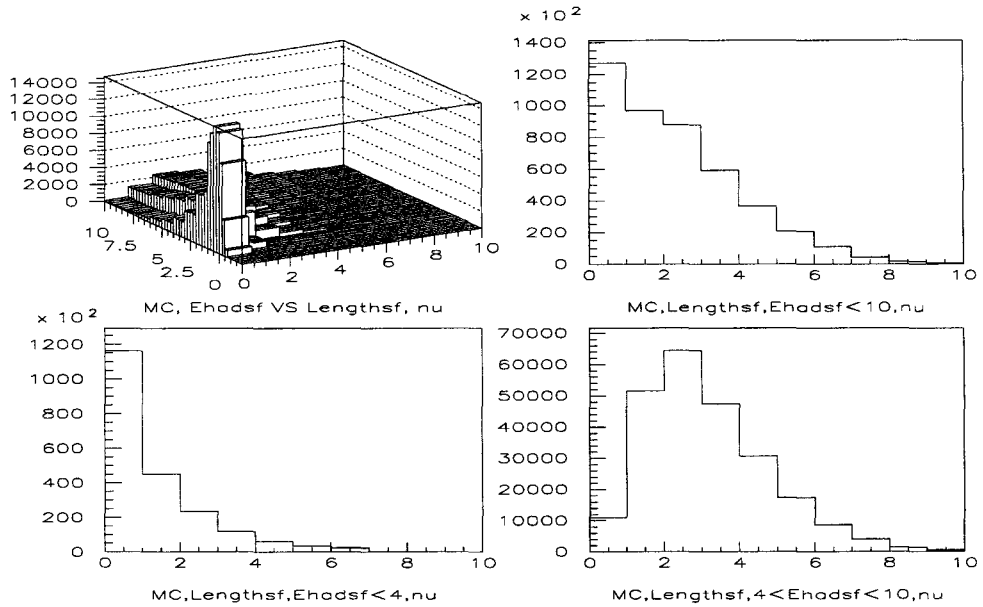


Figure A.12: The distribution from output NUMONTE with E_{had} finer bins for NuTeV length distribution in ν mode. The top left plot shows the 2D lego plot of the length distribution (x-axis) versus the E_{had} distribution (y-axis). The top right plot shows the length distribution for $E_{had} < 10$. The bottom left plot shows the length distribution for $E_{had} < 4$. The bottom right plot shows the length distribution for $4 < E_{had} < 10$.

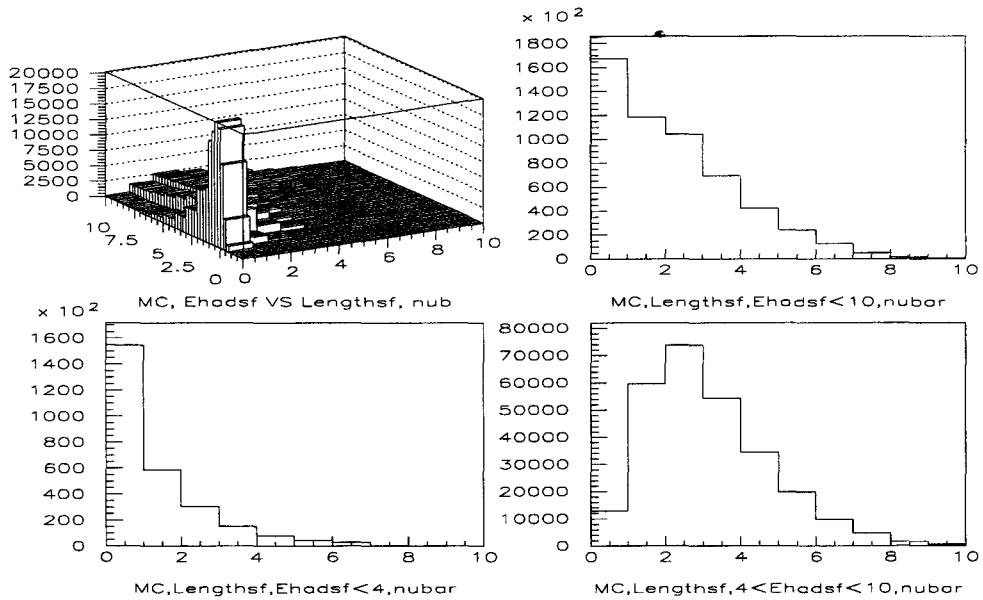


Figure A.13: The same distribution in $\bar{\nu}$ mode.

Appendix B

E_μ Subtraction Calculation

Muon deposits energy in the target calorimeter along the track as it traverses. In the shower region this muon energy is subtracted off the total energy deposit in the target and the result is the hadron energy (refer back to Eq. 5.23). Outside the shower region the energy deposited in the counter is from muon energy only. The subtraction should be zero outside the shower region to ensure that E_μ^{loss} describes the muon energy loss from data well. The subtraction of muon energy is defined as:

$$E_\mu^{diff} = E^{cntr} - E_\mu^{loss}. \quad (\text{B.1})$$

The sample for this study is the charged current events which the shower ends at least 45 counters before entering the toroid magnet. Then sum the energy difference 5, 10, 15, and 20 counters down stream from 20 counters from the counter where the shower ends ($SHEND - 20$).

Figure B.1 and B.2 show the data (DT) and Monte Carlo (MC) comparison of E_μ^{diff} with different number of counters sum. The means of the plots are not zero. These

imply that neither data nor Monte Carlo subtracts off enough muon energy. The values of the means from data and Monte Carlo are shown in Table B.1. The more counters sum used, the higher the means are. The mean is linearly increasing as the number of counters increase. By averaging the muon energy shift from these plots, the muon energy shift per counter in the data are 0.047632 and 0.044892 for neutrino and anti-neutrino, respectively, and 0.047402 and 0.045970 for neutrino and anti-neutrino from Monte Carlo events, respectively.

Number of counters sum from $shend - 20$	ν Mode		$\bar{\nu}$ Mode	
	DT	MC	DT	MC
5	0.2503	0.2384	0.2366	0.2323
10	0.4822	0.4748	0.4556	0.4623
15	0.7105	0.7102	0.6698	0.6900
20	0.9386	0.9467	0.8826	0.9139
Average/counter	0.047632	0.047402	0.044892	0.045970

Table B.1: The mean values of E_{μ}^{diff} from data and Monte Carlo in ν and $\bar{\nu}$ modes.

After applying the new muon energy shift subtraction to the previous plot, the new plots show the means are approximately equal to zero as shown in Table B.2.

Number of counters sum from $shend - 20$	ν Mode		$\bar{\nu}$ Mode	
	DT	MC	DT	MC
5	0.0128	0.0017	0.0127	0.0027
10	0.0074	0.0023	0.0087	0.0039
15	-0.0002	0.0030	-0.0002	0.0040
20	-0.0074	0.0055	-0.0104	0.0001

Table B.2: The mean values of E_{μ}^{diff} from data and Monte Carlo in ν and $\bar{\nu}$ modes after applying E_{μ}^{diff} .

Later on, we apply these muon subtractions to the hadron energy. Previously the plots show that the peaks shift to the right as the number of counters sum increases. After applying the shift the plots show the peaks are now center at zero as shown in Fig. B.6 - Fig. B.8 for data and Monte Carlo, respectively.

2002/10/03 18.28

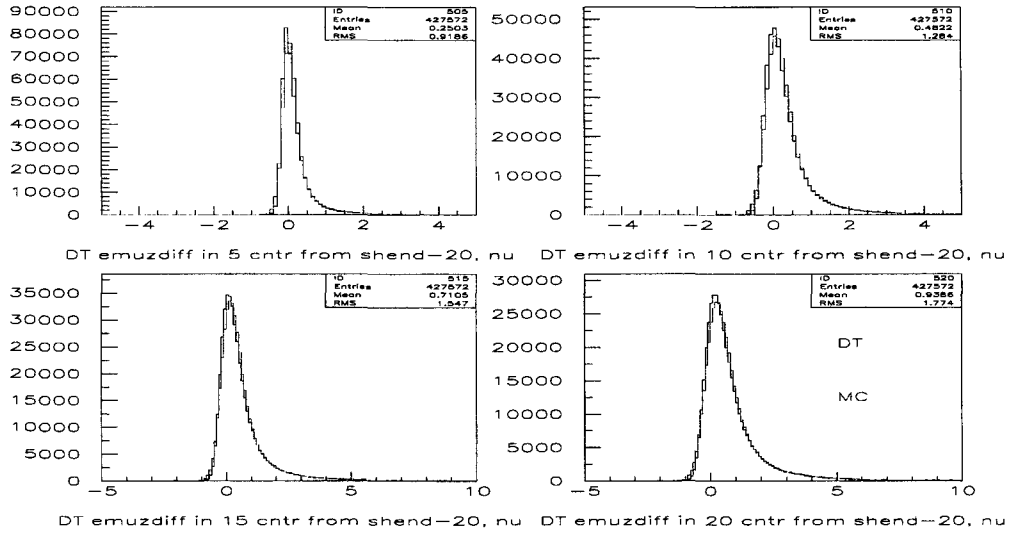


Figure B.1: E_{μ}^{diff} distributions from DT in black and MC in red in ν -mode. The top left is the sum of E_{μ}^{diff} from counter shend-20 to shend-25. The top right is the sum from shend-20 to shend-30. The bottom left is the sum from shend-20 to shend-35. And the bottom right is the sum from shend-20 to shend-40.

2002/10/03 18.28

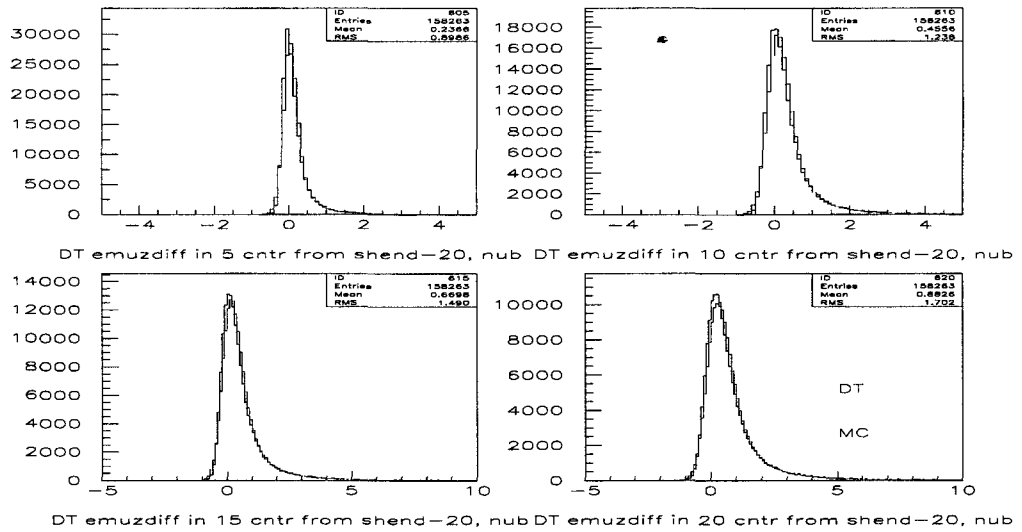


Figure B.2: The same distribution in $\bar{\nu}$ mode.

2002/10/03 18.29

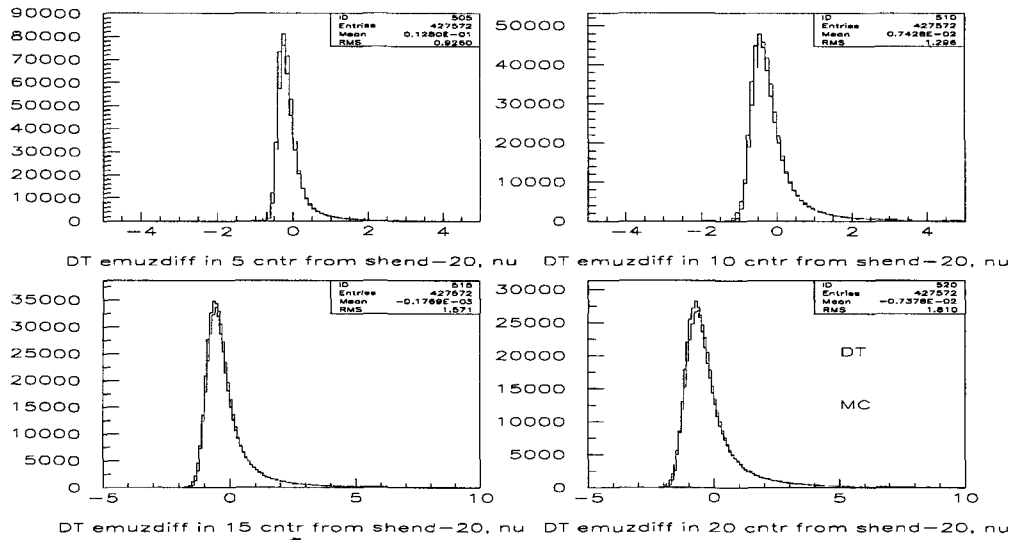


Figure B.3: E_{μ}^{diff} distributions from the data after applying the muon energy shift, DT in black and MC in red in ν -mode. The top left is the sum of E_{μ}^{diff} from counter shend-20 to shend-25. The top right is the sum from shend-20 to shend-30. The bottom left is the sum from shend-20 to shend-35. And the bottom right is the sum from shend-20 to shend-40.

2002/10/03 18.29

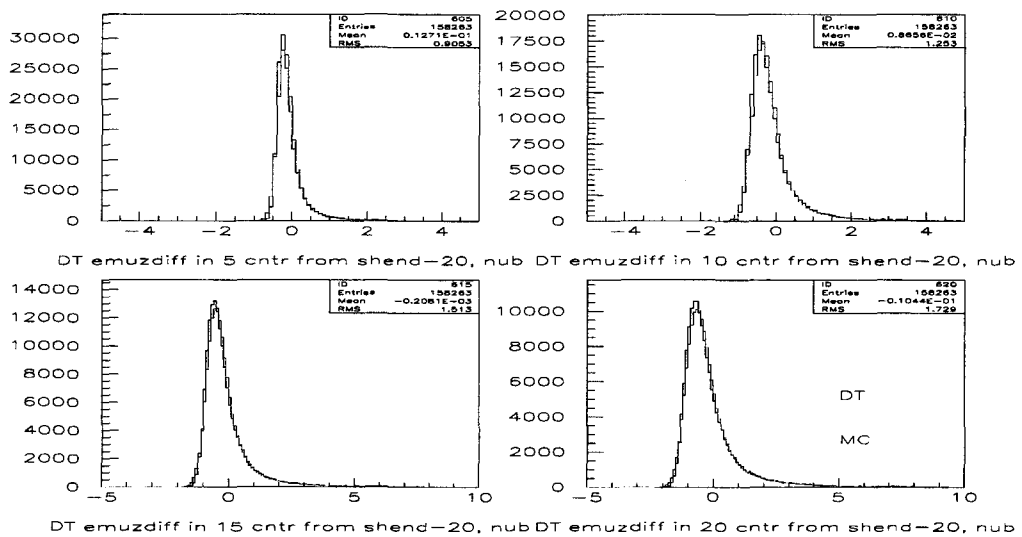


Figure B.4: The same distribution after applying the shift in $\bar{\nu}$ mode.

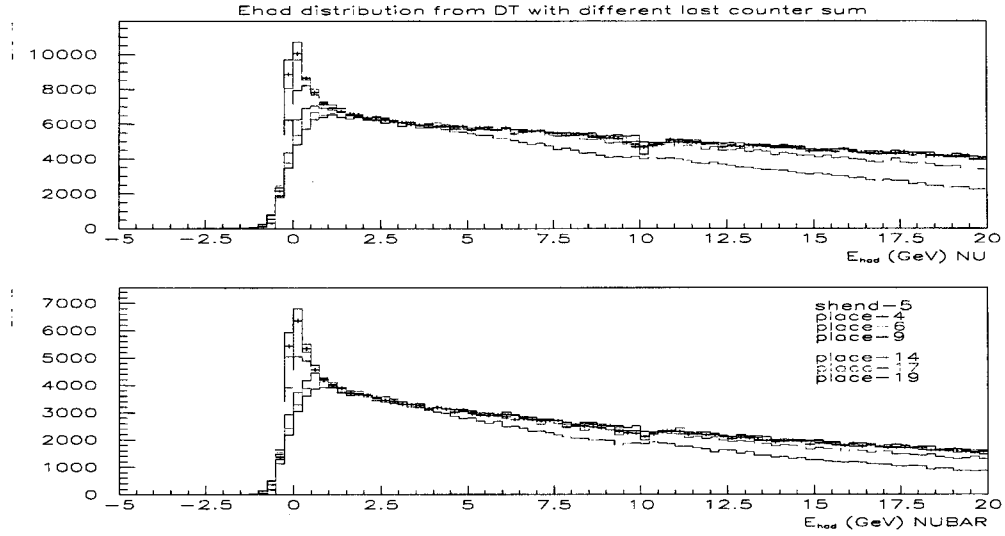


Figure B.5: Comparison of E_{had} distributions from DT for both ν (top) and $\bar{\nu}$ (bottom) events using different numbers of counter sum before applying E_{μ}^{diff} .

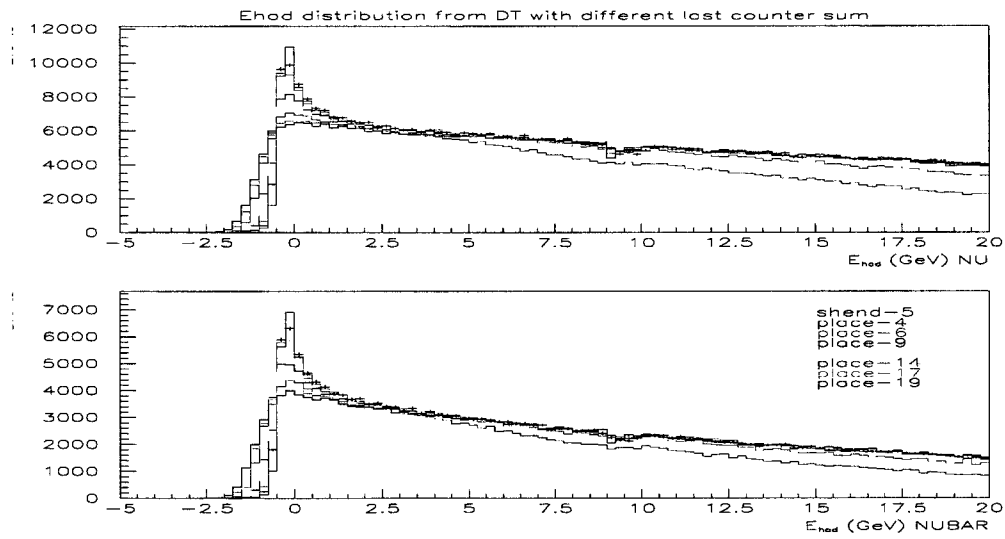


Figure B.6: Comparison of E_{had} distributions from DT, for both ν (top) and $\bar{\nu}$ (bottom) events using different numbers of counter sum after applying E_{μ}^{diff} .

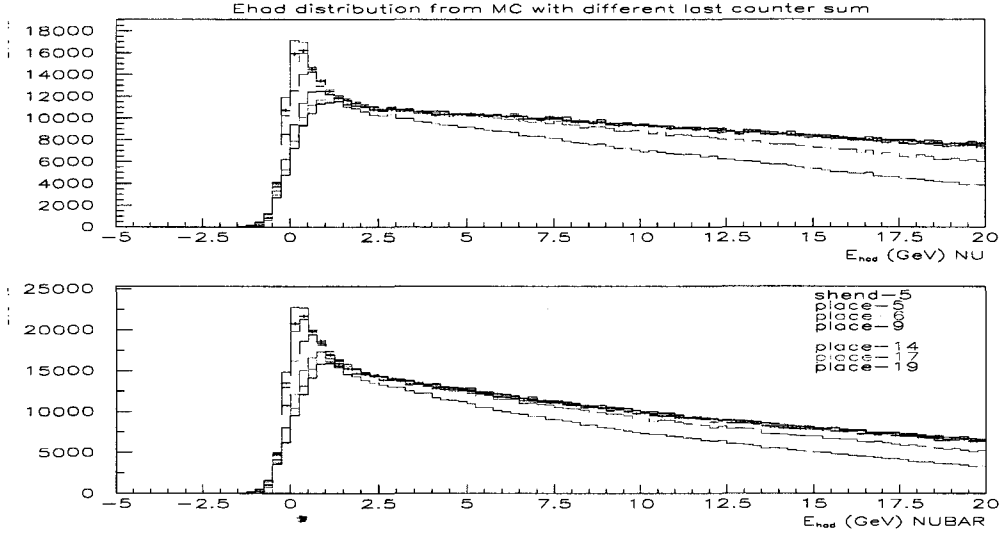


Figure B.7: Comparison of E_{had} distributions from MC, for both ν (top) and $\bar{\nu}$ (bottom) events using different numbers of counter sum before applying E_{μ}^{diff} .

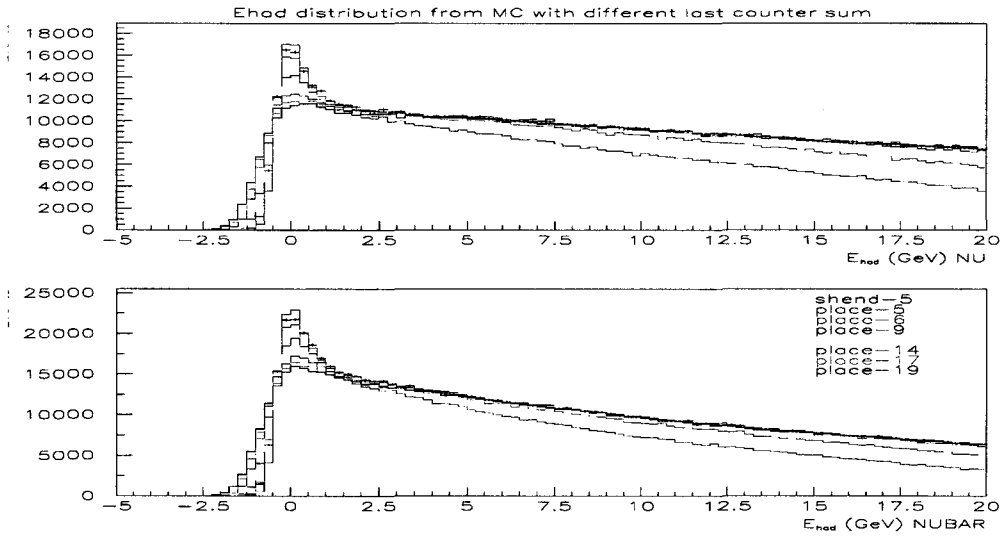


Figure B.8: Comparison of E_{had} distributions from MC, for both ν (top) and $\bar{\nu}$ (bottom) events using different numbers of counter sum after applying E_{μ}^{diff} .

Bibliography

- [1] J. Yu *et al.*, “*Technical Memorandum: NuTeV SSQT Performance*”, Report No. FERMILAB-TM-2040 (1998).
- [2] Particle Data Group (PDG), Particle Physics Booklet, July (2002).
- [3] J. Bailey *et al.*, Nucl. Phys. **B151**, 367-388 (1979).
- [4] E. J. Moniz *et al.*, Phys. Rev. Lett. **26**, 445-448 (1971).
- [5] A. Bodek and J. L. Ritchie, Phys. Rev. **D23**, 1070-1091 (1981).
- [6] D. Griffiths, *Introduction to Elementary Particles*, John Wiley & Sons (1987).
- [7] D. H. Perkins, *Introduction to High Energy Physics 3rd edition*, Addison Wesley (1987).
- [8] S. Dasu *et al.*, Phys. Rev. Lett. **60**, 2591-2594 (1988).
- [9] S. Dasu *et al.*, Phys. Rev. Lett. **61**, 10611-1064 (1988).
- [10] L. W. Whitlow *et al.*, Phys. Lett. **B250**, 193-198 (1990).
- [11] F. Halzen and A. D. Martin, *Quarks and Leptons: An Introductory Course in Modern Particle Physics*, John Wiley & Sons (1984).

- [12] G. P. Zeller *et al.*, Phys. Rev. Lett. **88**, 091802 (2002).
- [13] G. P. Zeller *et al.*, Phys. Rev. **D65**, 111103 (2002).
- [14] S. Kretzer *et al.*, BNL-NT-03/16, RBRC-328.
- [15] F. G. Cao and A. I. Signal, hep-ph/0302206.
- [16] C. H. Llewellyn Smith *et al.*, Physics Report **3C**, 261-379 (1972).
- [17] D. Rein and L. M. Sehgal, Ann. Phys. **133**, 79-153 (1981).
- [18] D. Rein, Z. Phys. **C35**, 43-64 (1987).
- [19] C. H. Albright and L. S. Liu, Phys. Rev. **B140**, 748-761 (1961).
- [20] R. P. Feynman, M. Kislinger, and F. Ravndal, Phys. Rev. **D3**, 2706-2732 (1971).
- [21] H. Georgi and H. D. Politzer, Phys. Rev. **D14**, 1829-1848 (1976).
- [22] R. Barbieri *et al.* Phys. Lett. **B64**, 171-176 (1976).
- [23] R. Barbieri *et al.* Nucl. Phys. **B117**, 50-76 (1976).
- [24] A. Bodek and U. K. Yang, hep-ex/0210024.
- [25] A. Bodek and U. K. Yang, hep-ex/0203009.
- [26] U. K. Yang, Ph.D.Thesis, University of Rochester (2001).
- [27] W. K. Sakumoto *et al.*, Nucl. Inst. Meth. **A294**, 179-192 (1990).
- [28] U. K. Yang and A. Bodek, Phys. Rev. Lett. **82**, 2467-2470 (1990).
- [29] U. K. Yang and A. Bodek, Eur. Phys. J. **C13**, 241-245 (2000).

- [30] J. A. Formaggio, Ph.D.Thesis, Columbia University (2001).
- [31] A. Alton *et al.*, Phys. Rev. **D63**, 012001 (2001).
- [32] S. E. Avvakumov, Ph.D.Thesis, University of Rochester (2001).
- [33] D. A. Harris *et al.*, Nucl. Inst. Meth. **A447**, 377-415 (2000).
- [34] G. P. Zeller, Ph.D.Thesis, Northwestern University (2002).
- [35] D. Yu. Bardin and V. A. Dokuchaeva, Nucl. Phys. **B246**, 221-230 (1984).(Preprint JINR-E2-86-260 (1986).)
- [36] W. G. Seligman, Ph.D.Thesis, Columbia University, Nevis Report 292 (1997).
- [37] R. Belusevic and D. Rein, Phys. Rev. **D38**, 2753-2757 (1988).
- [38] B. J. King, Ph.D.Thesis, Columbia University, Nevis Report 284 (1994).
- [39] Internal BooNE experiment note presented by Randy Johnson.
- [40] Private communication with Donna Naples.
- [41] Private communication with Martin Tzanov.
- [42] Private communication with Unki Yang.
- [43] S. V. Belikov *et al.*, Z. Phys. **A320**, 625-633 (1985).
- [44] N. J. Baker *et al.*, Phys. Rev. **D23**, 2499-2505 (1981).
- [45] S. J. Barish *et al.*, Phys. Rev. **D16**, 3103-3121 (1977).
- [46] T. Kitagaki *et al.*, Phys. Rev. **D28**, 436-442 (1983).

- [47] J. Brunner *et al.*, Z. Phys. **C45**, 551-555 (1985).
- [48] D. Allasia *et al.*, Nucl. Phys. **B343**, 285-309 (1990).
- [49] S. Bonetti *et al.*, Il Nuovo Cimento, **A38**, 260-270 (1977).